



UPPSALA
UNIVERSITET

*Digital Comprehensive Summaries of Uppsala Dissertations
from the Faculty of Science and Technology 1186*

Synthesis and Characterisation of Ultra Thin Film Oxides for Energy Applications

MATTIS FONDELL



ACTA
UNIVERSITATIS
UPSALIENSIS
UPPSALA
2014

ISSN 1651-6214
ISBN 978-91-554-9048-5
urn:nbn:se:uu:diva-232948

Dissertation presented at Uppsala University to be publicly examined in Polhemsalen, 10134, Ångström, Lägerhyddsvägen 1, Uppsala, Friday, 21 November 2014 at 10:15 for the degree of Doctor of Philosophy. The examination will be conducted in English. Faculty examiner: Professor Christophe Detavernier (Ghent University).

Abstract

Fondell, M. 2014. Synthesis and Characterisation of Ultra Thin Film Oxides for Energy Applications. *Digital Comprehensive Summaries of Uppsala Dissertations from the Faculty of Science and Technology* 1186. 113 pp. Uppsala: Acta Universitatis Upsaliensis. ISBN 978-91-554-9048-5.

This thesis describes studies of materials which can be exploited for hydrogen production from water and sunlight. The materials investigated are maghemite ($\gamma\text{-Fe}_2\text{O}_3$), magnetite (Fe_3O_4) and especially hematite ($\alpha\text{-Fe}_2\text{O}_3$), which is an iron oxide with most promising properties in this field. Hematite has been deposited using Atomic Layer Deposition (ALD) - a thin-film technique facilitating layer-by-layer growth with excellent thickness control and step coverage. The iron oxides were deposited using *bis-cyclopentadienyl* iron ($\text{Fe}(\text{Cp})_2$) or *iron pentacarbonyl* ($\text{Fe}(\text{CO})_5$) in combination with an O_2 precursor. Since it is crucial to have good control of the deposition process, the influence of substrate, process temperature, precursor and carrier gas have been investigated systematically. By careful control of these deposition parameters, three polymorphs of iron oxide could be deposited: hematite ($\alpha\text{-Fe}_2\text{O}_3$), maghemite ($\gamma\text{-Fe}_2\text{O}_3$) and magnetite (Fe_3O_4).

The deposited materials were characterized using X-ray Diffraction, Raman and UV-VIS Spectroscopy, and Scanning Electron Microscopy. Hard X-ray Photoelectron Spectroscopy (HAXPES) was also used, since it is a non-destructive, chemically specific, surface sensitive technique – the surface sensitivity resulting from the short mean escape depth of the photoelectrons. The depth probed can be controlled by varying the excitation energy; higher photoelectron energies increasing the inelastic mean-free-path in the material.

HAXPES studies of atomic diffusion from F-doped SnO_2 substrates showed increased doping levels of Sn, Si and F in the deposited films. Diffusion from the substrate was detected at annealing temperatures between 550 °C and 800 °C. Films annealed in air exhibited improved photocatalytic behavior; a photocurrent of 0.23 mA/cm² was observed for those films, while the as-deposited hematite films showed no photo-activity whatsoever.

The optical properties of low-dimensional hematite were studied in a series of ultra-thin films (thicknesses in the 2-70 nm range). The absorption maxima were shifted to higher energies for films thinner than 20 nm, revealing a different electronic structure in thin films.

Keywords: Atomic Layer Deposition, Iron oxides, Hematite, Solar Water Splitting, Hard X-Ray Photoelectron Spectroscopy

Mattis Fondell, Department of Chemistry - Ångström, Inorganic Chemistry, Box 538, Uppsala University, SE-751 21 Uppsala, Sweden.

© Mattis Fondell 2014

ISSN 1651-6214

ISBN 978-91-554-9048-5

urn:nbn:se:uu:diva-232948 (<http://urn.kb.se/resolve?urn=urn:nbn:se:uu:diva-232948>)

"I have not failed. I've just found 10,000 ways that won't work."
- *Thomas A. Edison*

Till Min Familj

List of papers

This thesis is based on the following papers, which are referred to in the text by their Roman numerals.

- I. Optical Quantum Confinement in Low Dimensional Hematite**
Mattis Fondell, T. Jesper Jacobsson, Mats Boman and Tomas Edvinsson
Journal of Materials Chemistry A, **2**, 3352–3363 (2014)
- II. Phase Control of Iron Oxide Grown in Nano-Scale Cauliflower Structures: Hematite, Maghemite and Magnetite**
Mattis Fondell, Mihaela Gorgoi, Linus von Fieandt, Mats Boman and Andreas Lindblad
Submitted to Vacuum
- III. Temperature Induced Diffusion of Sn and Si in Hematite and Implications for Photocatalytic Water Splitting Applications**
Mattis Fondell, T. Jesper Jacobsson, Mihaela Gorgoi, Linus von Fieandt, Mats Boman, Tomas Edvinsson and Andreas Lindblad
Submitted to Energy & Environmental Science
- IV. On the Structural and Optical Properties of Ultrathin Iron Oxide**
Indrek Jogi, T. Jesper Jacobsson, **Mattis Fondell**, Timo Vätjen, Jan-Otto Carlsson, Mats Boman and Tomas Edvinsson
Submitted to Journal of Solid State Chemistry
- V. Self-supported Three-Dimensional Nanoelectrodes for Microbattery Applications**
S. Cheah, E. Perre, Mårten Rooth, **Mattis Fondell**, Anders Hårsta, Leif Nyholm, Mats Boman, Jun Lu, Paul Simon and Kristina Edström
Nano Letters, **9**, 3230–3233 (2009)
- VI. An HAXPES study of Sn, SnS, SnO and SnO₂**
Mattis Fondell, Mihaela Gorgoi, Mats Boman and Andreas Lindblad
Journal of Electron Spectroscopy and Related Phenomena, **195**, 195–199 (2014)
- VII. HAXPES Study of Sn Core Levels and Their Plasmon Loss Features**
Mattis Fondell, Mihaela Gorgoi, Mats Boman and Andreas Lindblad
Results in Physics, in press, (2014) DOI: 10.1016/j.rinp.2014.08.006

**VIII. Surface modification of iron oxides by ion bombardment –
comparing depth profiling by HAXPES and Ar ion sputtering**
Mattis Fondell, Mihaela Gorgoi, Mats Boman and Andreas Lindblad
Submitted to Results in Physics

Reprints were made with permission from the publishers.

My contributions to the papers in this thesis

Paper I: I was responsible for planning the paper and did the work regarding depositions, XRF, SEM, XRD and Raman measurements. I wrote the sections regarding the deposition and the analysing techniques which I was responsible for and were involved all discussions regarding the paper.

Paper II: I was responsible for planning the paper and did the depositions, XRF, XRD, and Raman measurements. The HAXPES measurements were done together with one of the co-authors. I wrote the main part of the paper and were involved in all discussions.

Paper III: I was responsible for planning the paper and did the depositions, XRD and Raman measurements. The HAXPES measurements were done together with one of the co authors. I wrote the main part of the paper and were involved in all discussions.

Paper IV: Took part in the depositions and the characterisation of the samples. Wrote parts of the paper and were involved in all the discussions.

Paper V: Performed all the depositions of TiO_2 and took part in the planning of the experiments performed.

Paper VI: I was responsible for all the samples and performed the XRD. Took part in all the HAXPES measurements. Took part in the whole writing process, discussions and planning of the paper.

Paper VII: Took part in all the HAXPES measurements. Took part in the whole writing process, discussions and planning of the paper together with one of the co authors.

Paper VIII: Took part in all the HAXPES measurements and performed the XPS and Raman measurements. Took part in the whole writing process, discussions and planning of the paper.

Extended bibliography

The following conferences which I have contributed and been to.

1. Atomic Layer Deposition of Ultrathin Iron Oxide Films for Photovoltaic Applications

Mattis Fondell, Indrek Jogi, Mats Boman and Tomas Edvinsson
Orally presented in Kyoto, Japan, at the 15th International Conference on Thin Films, 8–11 Nov, 2011

2. Phase Selective Deposition of α -Al₂O₃ by Thin Layers of TiO₂

Mattis Fondell, Mats Boman, Sara Munktell, Oscar Alm, Tommy Larsson
Orally presented in San Diego, USA, at the 40th International Conference on Metallurgic Coatings and Thin Films, 28 Apr - 3 May, 2013

3. Atomic Layer Deposition for Energy Related Applications

Mattis Fondell, Indrek Jogi, Mats Boman and Tomas Edvinsson
Presented with Poster in Stenugnsund, Sweden, June, 2011

4. An HAXPES Study of Sn and Si Diffusion in Iron Oxide

Mattis Fondell, Mihaela Gorgoi, Mats Boman and Andreas Lindblad
Presented with Poster in Berlin, Germany, at User Meeting at Bessy II Helmholtz Zentrum, 4-6 Dec, 2013

Contents

1	Introduction	11
2	Theory and Background	17
2.1	Energy Bands	17
2.2	The Iron Oxides	18
2.2.1	Hematite (α -Fe ₂ O ₃), Maghemite (γ -Fe ₂ O ₃) and Magnetite (Fe ₃ O ₄)	19
3	Methods for Thin Film Material Synthesis	23
3.1	Atomic Layer deposition	23
3.1.1	The importance of the precursor	25
3.1.2	ALD Window	26
3.1.3	Dependence of deposition temperature	28
3.1.4	Effect of different substrates	28
3.1.5	Design of ALD reactors used in this thesis	30
3.1.6	Deposition parameters for the deposited films	32
4	Characterization Techniques and Experimental Details	37
4.1	X-ray Diffraction (XRD)	37
4.2	X-ray Fluorescence (XRFS)	40
4.3	Raman Spectroscopy	41
4.4	Scanning Electron Microscopy (SEM)	42
4.5	X-ray Photoelectron Spectroscopy (XPS) and Hard X-ray Photoelectron Spectroscopy (HAXPES)	43
4.6	Synchrotron radiation	49
4.6.1	Measurements with hard X-rays	53
4.6.2	Experimental details for reference measurements of Sn, SnS, SnO, SnO ₂ , Fe ₂ O ₃ and FeO.	53
4.7	UV-Visible spectroscopy / Optical absorption spectroscopy	55
5	Results and Discussion	57
5.1	Haxpes measurements on Sn, SnS, SnO and SnO ₂	57
5.2	Haxpes measurements on FeO and Fe ₂ O ₃	60
5.3	Thin film deposition	61

5.3.1	Titanium dioxide (TiO_2)	61
5.3.2	Iron oxides ($\alpha\text{-Fe}_2\text{O}_3$, $\gamma\text{-Fe}_2\text{O}_3$, Fe_3O_4)	63
5.3.3	The importance of the substrate during the deposition (Ferrocene as Iron precursor)	63
5.4	Choise of carrier gas during thin film deposition	70
5.5	Diffusion of Sn, Si and F in iron oxide upon annealing	75
5.6	Optical quantum confinement in low dimensional hematite	84
6	Summary and Conclusion	91
7	Svensk sammanfattning	95
	References	101

1. Introduction

A sustainable society can not depend on energy from fossil fuelled sources – for at least two reasons: the finite amount of such fuels (oil, natural gas, coal) available at reasonable prices [1–3], and the release of green house gas emissions, mainly in the form of carbon dioxide from the utilisation of those fuels. The latter contributes to global warming [1, 4, 5]. This thesis concerns materials that can be used for hydrogen production from water and sunlight. This is one possible component in a sustainable energy system which can harvest and store the energy from the sun for later use (for instance during night-time). Specifically I have studied methods to deposit thin films of various compounds and the films' chemical and physical properties. For a cost efficient device the materials need to be tailor made, and can be in the form of a thin film. One material which possess good properties for solar water splitting is hematite ($\alpha\text{-Fe}_2\text{O}_3$), an iron oxide, which is the main material I have studied.

Thin films and deposition techniques

Thin films can be present where we least expect them. For instance: a photograph is a thin film of colours on a white paper, a fluorescent lamp has an internal thin film which produces light at a low temperature, a coating on a razor blade to prolong its lifetime, or the thin film present on my glasses which prevents them from being scratched. These examples are not dependent on a perfect thin film, regarding a uniform thickness or the step coverage (in the nm range).

Different types of thin films are today widely produced at research facilities and in industries. The definition of a thin film is that the film is within or below the μm range [6] and the applications for such films are numerous [7].

Other applications need magnetic layers for data storage, photocatalytic interfaces for solar cells, dielectrics for the semi conductor industry, the surface of a drill, or the outer layers on a cutting tool – all with specific and diverse demands on the thin film. The quality of these films are often very high since they are produced for a specific and often "extreme" application, their thickness is often below 100 nm (in the case of cutting tools typically $10\mu\text{m}$).

Thin films are also one of the reasons why computers and mobile phones has decreased in size, and that their performance has increased rapidly since the 1960's [8]. Electronic parts and circuits can now be controlled, in the nanometer range. With technology progressing the constitutions need not to be large to assure function, for instance new oxide materials has made it possible to make transistors with sub 25 nm in size [7].

The main reason for the interest in thin films is that they can change the physical and chemical properties of the surface of the underlying material and desired properties may be promoted and functionality can be added. A thin film could enhance the hardness, roughness, give less friction, or it could be used as a protective layer for a sensitive layer beneath, *i.e.* solar cells or flexible OLED displays [9]. Many of the applications have high demands on the thin film, which often has to be of a specific thickness, having a well defined phase content and be uniformly deposited (without pinholes).

A thin film also have the added bonus of potential cost benefits: instead of manufacturing a certain component with 100% of the desired material, it is enough to have a cheaper material as a backbone with a thin film with the desired properties on top, having typically less than 1% of the total volume. One example is the platinum metal in a car catalyst: if it were solid there would be about 1 kg of platinum in the device, in reality there is only about 3 g on a ceramic backbone – lowering the cost from 33 000 € to 100 €.

There are a couple of well investigated thin film deposition techniques, which can produce thin films with good quality. Three common techniques are physical vapour deposition (PVD) [10], chemical vapour deposition (CVD) [11–13] and atomic layer deposition (ALD) [14–17].

Among these, PVD generally has a poorer step coverage than CVD and ALD and are less useful on high aspect ratio substrates or vicinal surfaces. The reason is that this is a line of sight technique, but the fast surface reactions and limited rearrangement time also influences. The line of sight phenomenon is illustrated in Figure 1.1. There are, ways to improve the step coverage, *e.g.* rotating the sample during deposition. PVD or sputtering, uses elemental or compound targets as raw material for the growth.

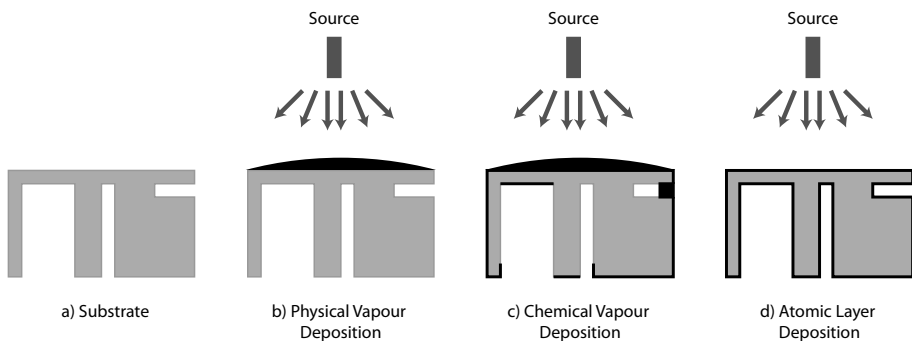


Figure 1.1. Illustration of step coverages of three different thin film deposition techniques. a) Schematic picture of a sample with cavities. b) Physical vapour deposition/Sputtering, c) Chemical vapour deposition, d) Atomic layer deposition.

CVD has been used in the microelectronic industry for a long time, since it provides a good thickness control, and that fairly high aspect ratios can be coated conformally. Briefly, the coating is deposited from a mix of precur-

sors in the gas phase, continuously present over the substrate. The precursors has to diffuse through the boundary layer which is present over the substrate, and a velocity gradient perpendicular to the flow direction is generated (in an horizontal reaction chamber). The concentration of the precursors are also dependant of flow distance. This makes large area substrates difficult to deposit, with a uniform thickness. This can be controlled by using a shower type of gas nozzle to distribute the gas phase evenly over the substrate, by tilting the sample or like in PVD, rotate the sample. To obtain conformal films in CVD, the reaction rate should be low, and the rate limiting step should be surface kinetics, not gas phase mass transport.

There are many similarities between CVD and ALD, since ALD is a sequential CVD process. The same experimental setup could often be used for either ALD or CVD (especially in research). The advantage with ALD is the self limiting precursor steps which give rise to conformal films with an excellent thickness control (illustrated in Figure 1.1), since the growth is atomic layer by atomic layer. The thickness can easily be controlled by the number of precursor pulses. In comparison with CVD, no reactions occur in the gas phase, instead the reaction take place on the surface of the substrate. ALD then avoid homogeneous nucleation in the gas phase. ALD also results in pinhole free, homogeneous and dense films at lower temperatures [18, 19]. It should be mentioned that ALD not always gives a layer by layer growth. In some cases island formation on the substrate could occur, and the initial growth procedure is strongly depending on the surface energies of the substrate [20, 21]. This behaviour causes a nonlinear growth and could give rise to structured surfaces, instead of the smooth films normally provided by ALD [22, 22]. Figure 1.1 illustrates the step coverage of PVD [23–26], CVD [27–30] and ALD [31–37]. The behaviour of the PVD and CVD could be a little flamboyant, but ALD is superior when step coverage is discussed.

The drawback using ALD is the slow deposition rate, compared with PVD or CVD. Layer by layer growth takes more time since only one precursor at the time is introduced into the reactor. There is, however, a "roll by roll" deposition chamber developed to increase the speed of an individual deposition [38, 39]. This is especially important for industries which uses ALD.

The technique used in this thesis were ALD, and pulsed CVD (pCVD). With pCVD the pulses are separated, as in ALD, but due to decomposition of the precursor, a higher growth rate can be achieved. ALD were chosen as the step coverage were of great importance on some of the substrates used. The thickness of the thin films discussed in this thesis are in the nanometer range.

Iron oxide as material for solar water splitting

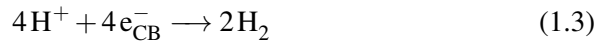
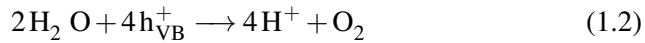
Since fossil fuels currently is the main source of energy, much research is focused to produce energy from a more environmentally friendly (carbon free) source. When fossil fuels (oil, coal or natural gas) are used the green house gas

CO₂ is produced ¹. The gas gets trapped in the atmosphere and contributes to the global warming [4]; greenhouse gases have always been present in earth's atmosphere – keeping heat in the form of infrared radiation stored in the atmosphere (the moon lacking a proper atmosphere, for instance, do not enjoy this storage of heat) by capturing IR-radiation emitted from the earth's surface, instead of letting it radiate into space. A deviation toward increasing concentrations from the natural levels of greenhouse gases have been occurring ever since humans started burning fossil fuels – a larger than natural fraction of the infrared radiation is thus kept and reradiated in the atmosphere. It is estimated that an 0.5 °C temperature increase have happened since the 1970's. Because of this, there is a large interest to find new sustainable (renewable) energy sources. Examples of renewable energy sources are: solar, hydroelectric, wind, wave and tidal energy [40]. Solar energy could potentially provide a large amount of energy. It is estimated that the energy emitted from the sun impinging on earth is approximately $3 \cdot 10^{24}$ J during a year. This is around 10000 times the current worldwide energy consumption, per annum [41]. This means that it would be enough with one hour to get enough energy to provide the world for one year – if it can be harvested and stored. It has been estimated that if solar cells were placed on a small area of the globe – *e.g.* a fraction of the Sahara desert – with a modest 10% efficiency of the solar cells it would be enough for the energy needed world wide [42]. Solar energy could in the end be able to provide both direct electrical power, and store energy in for example the form of hydrogen. Therefore water splitting, into molecular oxygen and hydrogen (Reaction 1.1), has attracted a lot of interest.



Solar hydrogen generation offers one route to harvest the energy from the sun into a chemically active form without carbon, which can be stored. The measurements performed in this thesis mainly investigates one component of the photoelectrochemical hydrogen production (the photoanode).

In a phototelectrochemical device, both the excited electrons in the conduction band (e^-_{CB}) and the produced holes in the valence band (h^+_{VB}) take part in the water splitting process at the cathode and anode under acidic conditions, shown in Reaction 1.2 and 1.3.



Fujishima and Honda were the first to demonstrate the concept using a photoelectrochemical device for solar energy conversion and storage [43]. However, in their experiment it was a high band gap material (TiO₂) and the pH

¹Carbon dioxide and methane (from agricultural sources) are the most abundantly emitted from human endeavours.

difference on the sides of the membrane which made it possible to perform water splitting. They proposed that water could be split, without applying any potential bias, using only the solar energy whereas the pH difference in practice gave a potential difference between the cells.

In this thesis hematite ($\alpha\text{-Fe}_2\text{O}_3$) has been evaluated for use in a water splitting device. Hematite has properties that are highly beneficial for this application, which have motivated this research [44–48]. The absorption coefficient of visible light is high, the band gap of around 2 eV fits with the energies involved in the water splitting process [49] as well as absorbs a large part of the visible solar spectrum, and the energetic position of the valence band edge is suitable for water oxidation. Hematite is, as evident by the widespread appearance of rust, highly stable in ambient environment and composed of abundant, cheap, and nontoxic elements.

The materials properties of hematite are, however not ideal. The conduction band edge of around + 0.2 V vs. normal hydrogen electrode (NHE) [49] is slightly too low for the unassisted hydrogen production. This could to some extent be overcome by making the hematite quantum confined, which could raise the conduction band edge. The more common approach, and the approach used in this thesis, is to target the hematite as a photoanode for the oxygen evolution reaction.

This situation is identical to several other semiconductors investigated for one of the half reactions, for example: TiO_2 [50, 51], WO_3 [52, 53], BiVO_4 [54, 55], ZnO [56, 57], CIGS [58], and Cu_2O [59, 60], which alone are not capable of unbiased water splitting in a single cell device architecture. In a working device, these semiconductors must be combined with an additional photoabsorber that adds the additional driving force for the full reaction. The standard approach to this problem is to construct tandem devices based on two semiconductors with different band gaps. Specific tandem combinations are sometimes also suggested, like the possibility to combine Fe_2O_3 photocathodes with a dye-sensitized solar cell [45, 61]. An alternative to tandem devices for obtaining the proper photopotential is to construct modules of several cells interconnected in series [62].

In the following chapters I describe the material systems in more detail, also the theoretical and experimental necessities are covered. The last chapters summarise the results of Paper I-VIII, and provides an outlook towards how this research may be continued.

2. Theory and Background

In this section some necessary theory is discussed as well as a brief introduction to different iron oxides. The importance of annealing iron oxide for the solar water splitting application is also discussed.

2.1 Energy Bands

A material, semiconductor or insulator, may be photo-excited; a photon ($\hbar\omega$) may excite an electron from the valence band to the conduction band, *i.e.* the difference between the valence and the conduction band is the band gap (E_g) of the material, illustrated in Figure 2.1. To create such an electron-hole pair the energy of the photon needs to be larger than the band gap, *i.e.* $\hbar\omega > E_g$. Depending on the size of the band gap, the absorption onset states are located at different photon energies, for semi conductors this is often in the visible-light range and insulators in the UV-range. There is also indirect band gaps, as in the case of hematite (iron oxide). This situation is described in more detail in the results section and Paper I.

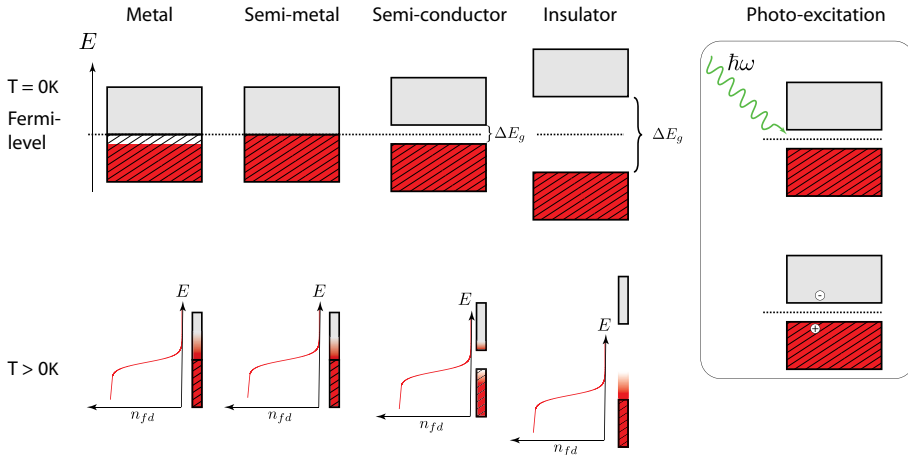


Figure 2.1. Illustration of electron occupancy of allowed bands for metal, semi-metal, semi-conductor, and insulator. The illustration also shows how the electron occupancies are different at 0 K and at higher temperatures ($T > 0\text{ K}$).

Doping of semiconductors can produce states in the energy gap, either electron states below the conduction band (n-type doping) or hole states above the

valence band (p-type doping) changes the conductivity and the band gap of the material. Another way of changing the width of the band gap is to change the size of the system. The size when this effect becomes noticeable is in the nm-scale. We may predict this behaviour from quantum mechanics and the solutions to the Schrödinger equation for a particle in a box, *i.e.* a particle in a well of finite extent with infinite potential barriers (see *e.g.* Sakurai for the solution to this problem [63]).

$$E_n = n^2 h^2 / 8mL^2 \quad (2.1)$$

Where h is Planck's constant and m the particle mass. The energy level n of the particle in a box is stated in Equation 2.1, for the same well-size $E_n \propto n^2$. If the well size is changed, the energy shifts, and the spacing between the states change as $1/L^2$.

This is the basic concept behind quantum confinement effects, where for molecules the absorption maximum changes with size. The photon energy needed to excite an electron from state n to $n+1$ behaves quantitatively with changing system size as in the experiment, obtained above in Figure 2.2. Of course a far better description of the actual potential needs to be made to quantitatively capture a real system behaviour.

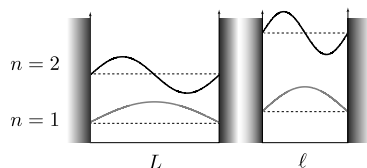


Figure 2.2. The first two energy levels with their corresponding wavefunctions of a free electron of mass m confined to a line with length L . The energy levels are numbered according to the quantum number (n), which gives the number of half waves present in the wavefunction.

2.2 The Iron Oxides

Iron oxides are compounds widespread in nature. This class of compounds have a rich palette of possible oxygen to iron ratios, as well as many different phases for each composition [49]. Iron compounds are widely used as pigment, in catalysts, in thermite, and one biological example is haemoglobin. The stability and non-toxic nature of the iron oxides makes them suitable to be used as pigments and coatings. As pigments the iron oxides gives colours from yellow to brown and black. Some colours of hematite, maghemite and magnetite are shown in Figure 2.3. The range of colours suggest that the electronic structure change with composition.

The iron oxides discussed in this thesis are hematite (α - Fe_2O_3), maghemite (γ - Fe_2O_3) and magnetite (Fe_3O_4). Wüstite (FeO) is also mentioned regarding the Fe^{2+} satellite in HAXPES. This section summaries the difference and similarities of the iron oxides in this thesis.

2.2.1 Hematite (α -Fe₂O₃), Maghemite (γ -Fe₂O₃) and Magnetite (Fe₃O₄)

Hematite, α -Fe₂O₃ has a corundum structure, with a hexagonal unit cell. The unit cell of hematite is shown in Figure 2.3. The structure can be described as: hexagonal close packed (hcp) anion (O^{2-}) arrays with two thirds of the octahedral sites filled with a Fe³⁺ cation. It is the most stable iron oxide and often the end transformation of the oxide when annealed in air [49].

Magnetite, Fe₃O₄, has an inverse spinel structure, with a cubic unit cell (Figure 2.3). Magnetite contains multivalent iron in contrast to the other iron oxides, and contains both Fe²⁺ and Fe³⁺. The cations occupy both octahedral and tetrahedral sites which results in both octahedral and mixed octahedral/tetrahedral stacked layers. In a perfect magnetite structure the relationship between Fe²⁺ and Fe³⁺ is 1:2.

Maghemite, γ -Fe₂O₃, has a structure similar to magnetite's. But instead of a mix in oxidation states maghemite has exclusively iron in the trivalent state. Vacancies in the Fe²⁺ positions compensate for the overall charge. Maghemite is cubic, with all the tetrahedral sites occupied with the cations and the remaining cations randomly distributed in octahedral sites (Figure 2.3) [49].

The three unit cells together with a thin film (40 nm) and the iron mineral are shown in Figure 2.3. The unit cell of maghemite illustrates the two different positions of the cations in the anion lattice. The iron which is in the tetrahedral sites are green, whereas the iron in the octahedral site are purple.

Hematite, maghemite and magnetite are all semiconductors. A semiconductor is conventionally defined as when the separation of the valence band of orbitals and the conduction band is less than 4 eV. The Fermi level is positioned in between the valence band and the conduction band for $T > 0K$, illustrated in Figure 2.1. Conductivity in a material is due to motion of the free charge carriers in the material. Those may either be electrons, in an empty conduction band, or hole vacancies in the normally filled valence band. In an n-type semiconductor the conductivity involves electrons at donor levels close to and below the conduction band, whereas in a p-type semiconductor holes are involved at donor levels above and close to the valence band.

For electrons to be excited from the valence band up to the conduction band an energy greater than the band gap is needed. When the band gap is small, heating of the material is enough for this excitation to occur. In the case of a higher band gap excitation of electrons can be achieved by irradiation with light at an appropriate wavelength [49].

Light absorption causes formation of an electron/hole pair (e^-/h^+) in the interfacial region of the solid and, in the presence of an electric field which is more negative at the surface, the electrons migrate inwards towards the bulk of the solid and the holes move towards the surface and react with the FeOH groups, *i.e.* the charges separate. A feature of the iron oxides is a relatively fast electron/hole recombination – many electrons recombine with the holes




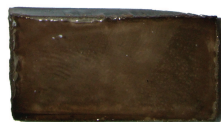


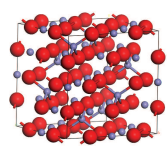
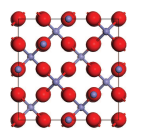
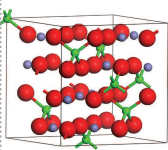
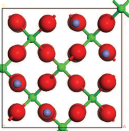
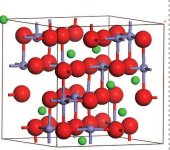
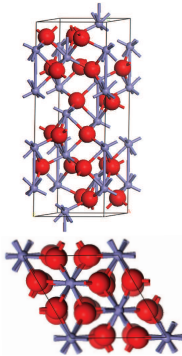
	Magnetite Fe_3O_4	Maghemite $\gamma\text{-Fe}_2\text{O}_3$	Hematite $\alpha\text{-Fe}_2\text{O}_3$
Mineral			
Thin Film			
Crystal structure	<div>Side view</div>  <div>Top view</div> 	<div>Side view</div>  <div>Top view</div> 	<div>Side view</div>  <div>Top view</div> 
	<div> ● - oxygen ● - iron (both Fe^{2+} and Fe^{3+}) </div>		

Figure 2.3. Crystal structure, mineral and thin films of hematite, maghemite [64] and magnetite. Bonds are added for an easier view of tetrahedral or octahedral sites.

and become neutralized – which decreases the photo-activity of the material [49].

Hematite is an n-type semiconductor and have a band gap of about 2 eV, it is stable at $\text{pH} > 4$, cheap to manufacture, and environmentally friendly [49]. This combined with the fact that a reasonable amount (29%) of visible light have energies larger than the hematite band gap, have raised interest for using hematite as an anode for the photo assisted electrolysis of water for hydrogen production [44, 65–67]. In these investigations, the hematite anodes were in the form of nanoparticles, thin films or single crystals.

The photo-electrochemical activity of hematite with respect to solar hydrogen production is unfortunately hampered by a short hole diffusion length [44, 68], short excited-state lifetime in the picosecond range [68], and a poor oxygen evolution reaction kinetics [69]. To increase the efficiency of hematite photoanodes, one approach has been to enlarge the surface area of the hematite by growing nano pillars, or cauliflower structures [70, 71] an example of increased surface is seen in Figure 3.3 a)-c). Another approach has been to improve the transport properties by introducing different dopants into the hematite lattice, either during the deposition process or with an annealing step.

Dopants introduced during the synthesis of hematite reported in literature are, for example: Si [72–75], Ti [72, 76–81], Al [80], Mg [82, 83], Zn [80, 84], Mo [85], Cr [85], Pt [86], Ge [87] and Sn [77, 79, 83, 88].

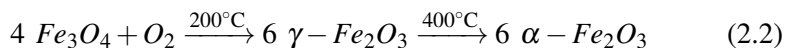
Examples of molecular doping are the use of tetraethyl orthosilicate (TEOS) for doping with Si [73], or $\text{SnCl}_4 \cdot 5 \text{H}_2\text{O}$ which has been used for doping with Sn [89]. Also dual doping with Sn/Be [77] or Ti/Al [80] has been tried.

The second approach has been to introduce dopants in the hematite lattice by annealing hematite. Fluorine doped tin oxide were used as substrate, as tin has been proven to be a suitable dopant. This effect has been investigated by Sivula *et al.* [90] where they show that Sn diffusion where observed when annealing at 800 °C for 10 hours. The effect of Sn dopants in hematite resulted in an increased absorption, with a factor two. Diffusion of Sn has also been seen at 650 °C from FTO into nano wires of hematite [88].

The effect of an increased absorption of Sn is that Sn^{4+} , which is tetravalent, can be substituted in the Fe^{3+} sites in hematite [79, 80, 91], which results in the formation of Fe^{2+} ions. The local pair of Fe^{2+} and Sn^{4+} acts as donor centres in the structure, which increases the electronconductivity [92]. This effect has also been investigated with Ti^{4+} [79, 80] with the similar result.

The material properties are, as discussed (in Section 1), not ideal for the full water splitting reaction. The conduction band edge is slightly too low for unassisted hydrogen production. This could, however, to some extent be overcome by making the hematite quantum confined, which could raise the conduction band edge. The more common approach is instead to target the hematite as a photoanode for the oxygen evolution reaction.

Magnetite has a band gap of 0.1 eV which makes it unsuitable for this kind of application. Maghemite, on the other hand, has a suitable band gap of 2 eV but has not gained as much interest as hematite, probably since hematite is the most stable of these oxides [49]. A common scheme, regarding phase transition/stability of the three iron oxides in ambient atmosphere discussed here, is seen in Reaction 2.2 [93, 94].



Maghemite is ferromagnetic at room temperature and has for example been used in many applications due to its magnetic properties and its needle-shaped

form, *i.e.* in tapes and diskettes [95]. Hematite is weakly ferromagnetic or antiferromagnetic at room temperature and has a Curie temperature of 956 K (paramagnetic) [49, 96]. Magnetite is ferrimagnetic and exhibit the strongest magnetism of any metal oxide [49, 97]. The difference in magnetic properties will influence the Raman spectra, discussed in Section 5.4.

It is easy to see the difference between magnetite, hematite and maghemite. Magnetite is black whereas hematite is dark red and maghemite is brown. When the iron oxides is in the form of a thin film it is difficult to distinguish hematite from maghemite, due to a very small colour difference between them (as seen in Figure 2.3), compared to bulk when the difference in colour is more distinct.

3. Methods for Thin Film Material Synthesis

In this section the deposition techniques used during this thesis are described and discussed. The ALD reactors used and experimental details are also included in this section.

3.1 Atomic Layer deposition

Atomic layer deposition (ALD) is a thin-film deposition technique developed in the early 1970's by the Finnish scientist T. Suntola and his co-workers [15, 98]. In the beginning, the technique was called atomic layer epitaxy (ALE). But since most of the deposited films became amorphous or polycrystalline, the name was changed from ALE to ALD. It should be mentioned that the Russian group of V. Aleskowsky also developed a similar method at the same time called molecular layering, describing alternate surface reactions characteristics to ALD [99–102]. Today a wide range of materials can be deposited with ALD. Pure metals, oxides, nitrides and sulphides can, for example, be deposited. An extensive compilation of the materials deposited with ALD is found in reference [16].

A general overview of an ALD process is given in Figure 3.1. The illustration describes film growth of a binary compound. Binary compounds are the most commonly grown, but ternary compounds have also been deposited [103, 104]. A binary ALD process is normally divided into four steps, completing one cycle (Figure 3.1).

The first step contains in this case the metal precursor, which is transported in the gas phase, to the deposition chamber by a carrier gas. The carrier gas is normally an inert gas. The first precursor adsorbs on the substrate surface, forming one monolayer that chemisorbs to the surface (Figure 3.1 a). The second step in the cycle is a rinse pulse that removes the excess of the first precursor, shown in Figure 3.1 b). This is usually performed by the carrier gas. The third step adds the second precursor, which reacts with the chemisorbed molecules on the surface, seen in Figure 3.1 c). The fourth and last step then removes the excess of the second precursor, seen in Figure 3.1 d). Ideally one cycle should generate one monolayer of film on the substrate. By changing the number of cycles, the number of layers can be determined and the thickness can be controlled [14].

The time for the different precursor and purge pulses in an ALD cycle are customised for each deposition, strongly depending on the substrate and precursors used. For three dimensional substrates, the time for each pulse needs

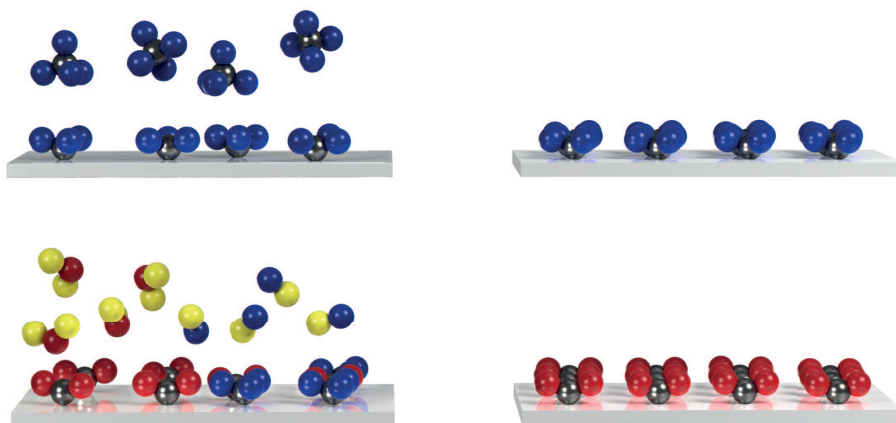


Figure 3.1. The four different pulses completing one cycle in ALD. The four steps completing one cycle are illustrated with TiI_4 and H_2O as precursors, to deposit TiO_2 . First the TiI_4 covers the surface with one monolayer. The first reaction which take place is that the iodine from TiI_4 reacts with the hydrogen from the surface which is OH terminated. The second part of the cycle consist of a rinse with nitrogen to clean the reactor and surface from the residual of TiI_4 . The second precursor, in this case H_2O , is then rinsed into the reactor, and reacts with the monolayer of TiI_3 creating TiO_2 on the surface. The last step in the cycle is then a rinse gas to clean the reactor and surface from the residual of H_2O .

to be long enough so that the precursors have the time to form a monolayer of adsorbates and the excess to be rinsed out of the structure. For a flat surface short pulse times can be used. The pulse lengths also differs depending on the design of the ALD reactor used. The ALD process is optimised to obtain the shortest cycle time.

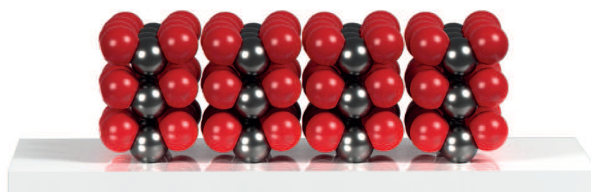


Figure 3.2. Schematic picture after of the deposited film (TiO_2) after three ALD cycles.

For a binary compound a cycle with four steps are necessary, since separation of the two reactive pulses containing the precursors, is necessary. This separation is one of the advantages of ALD, which provides good thickness control of the deposited material. Since ALD have separation of the reactive precursors, more reactive precursors can be used which also can decrease the deposition temperature, compared with CVD [17]. Most ALD processes includes one metal containing precursor, that subsequently reacts with the other

precursor. The second precursor is typically an oxygen, a nitrogen or a sulphur containing compound. The reactions which take place between the two precursors are often simple, like hydrolysis, oxidation, reduction or organic coupling.

Depending on the wanted film thickness, the number of cycles can be tailored. An illustration of three cycles is shown in Figure 3.2. The growth rate per cycle varies and depend on the precursors used in the process but are normally less than a couple of Ångström. This makes the deposition process rather slow compared to other deposition techniques. The large advantages of ALD compared to other techniques are instead an excellent thickness control and also high step coverage where trenches and porous materials can be coated with high uniformity, illustrated in Figure 1.1.

3.1.1 The importance of the precursor

The selection of a precursor is a important step in an ALD process. Typically reactive precursors are used to lower the deposition temperature. Growth rate and precursor residues of the film are two important factors, and has to be taken into account. Etching of the deposited film may occur with some precursors (often chloride based precursors). In general precursors can either be in the form of a gas, a liquid or a solid. The easiest precursor to work with is a gas which can be easily controlled with mass flow controllers. A liquid precursor is also commonly used, and can be controlled by an evaporator, and a pneumatic valve controls the amount of the precursor from each pulse.

There are some basic restrictions for the choice of a precursor. The precursor has to have a reasonably high vapour pressure (for a liquid or a solid) to deliver enough molecules to the reaction chamber, and have a good thermal stability to avoid decomposition. It also needs to chemisorb onto the substrate. To obtain the wanted vapour pressure of the precursor, heating or in some cases cooling is necessary. In the case of a solid precursor a sublimator is necessary. The quantity of the solid needs to be sufficient so that the amount of gaseous precursor is enough for the whole deposition, depending on the number of cycles applied. The rinse pulses, which are in between the two precursor steps, are necessary for separation of the precursor gases which otherwise could react homogeneously in the gas phase and form powdery deposits [17].

If the precursors are chosen with these demands in mind, the purge times are long enough, and when the temperature and pressure in the deposition chamber is correctly chosen, ALD type of growth can be achieved. ALD then has the advantage of precise thickness control, normally in the nanometer range. Since ALD is not a line of sight deposition technique, like physical vapour deposition (PVD), complicated 3D structures may be coated with the same precision as that of a flat substrate, as illustrated in Figure 1.1. Structures like pillars, porous material, pores and trenches are therefore not an issue and

can be conformally coated [36, 105], Paper V. This is illustrated in Figure 3.3 where both a flat surface (a), a porous structure or nano particles (b) and a pillars structure (c) could be deposited with a uniform thickness. A cross section of one of the pillars is shown in Figure 3.3 where two different materials has been deposited (example of multilayers is found in Ref. [36] where TiO_2 and Fe_2O_3 is used).

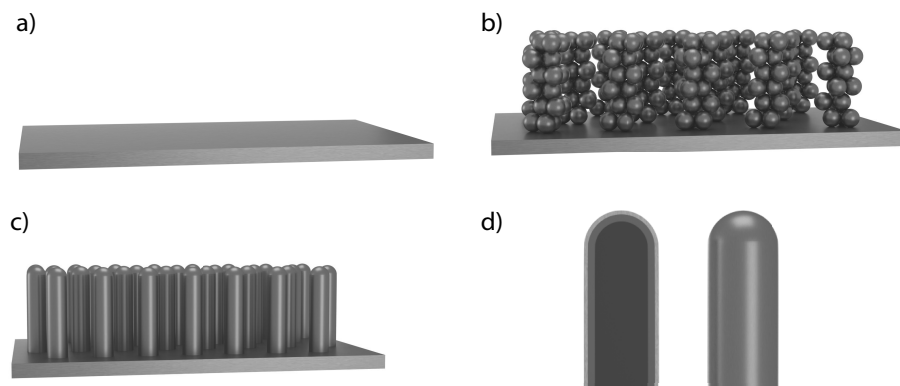


Figure 3.3. Schematic picture of how 3D structures enhance the surface area. (a) A flat surface. (b) Nano particles on a surface. (c) Pillar structured surface. (d) A schematic image how thin films on a 3D substate can look.

3.1.2 ALD Window

The temperature in the reaction chamber is of paramount importance. Some ALD processes like trimethylaluminium (TMA)/ H_2O and $\text{TiCl}_4/\text{H}_2\text{O}$ possess ALD growth in large temperature interval [16]. But most of the known ALD processes have a smaller temperature interval, often limited by the first precursor (step one in Figure 3.1). The temperature interval where a stable growth per cycle as a function of temperature is achieved is called the ALD-window and is shown in Figure 3.4. At lower temperature either condensation (higher adsorption) of the precursor on the substrate can occur, leading to a higher deposition rate. At lower temperature the reactivity of the precursor may also be too low, and higher temperatures are needed to increase the reactivity. At higher temperatures, the deposition rate may increase, due to precursor decomposition, *i.e.* the ALD process becomes a CVD process. The deposition rate can also be smaller at higher temperatures, indicating desorption of the precursor from the substrate.

The ALD-window is a good tool for investigating the temperature window of the precursors. The window can, however, be different for precursor combinations and can also change between different reaction chambers, with an identical pair of precursors. The ALD-window can also be absent in some cases, but ALD growth could still occur, at specific temperatures.

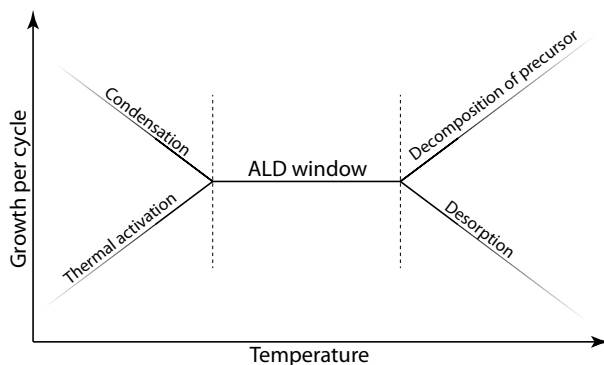


Figure 3.4. Growth per cycle vs. temperature of different growth modes which can occur in ALD. In the middle the ALD window is located. Here a constant growth rate is achieved.

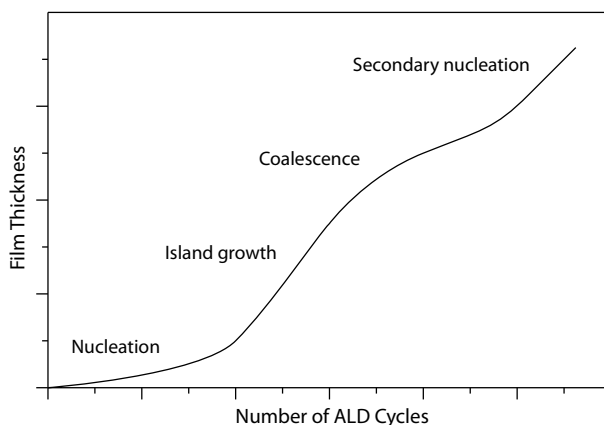


Figure 3.5. Schematic picture of the chemistry that could occur during the initial growth in an ALD process. Ideally a straight line is expected, but nucleation can decrease the growth rate initially. Island growth then gives a higher surface area, and an increased growth rate is observed. When the islands coalesce, the surface area is decreased and a stable value of growth rate is obtained. Secondary nucleation could however occur at a later stage which increases the surface area again, and so forth.

The thickness in ALD is ideally trivially related on the number of cycles. This is however not the case in many precursor combinations used for ALD experiments. During the first couple of cycles there is often a problem with the nucleation on the substrate. This could either have to do with the precursor or the surface of the substrate. Once stable nuclei are formed on the substrate a film starts to grow on top of them. This will initially increase the surface area leading to higher growth rate of the film. As the deposition continue the nuclei coalesce into a continuous film. After this, a stable value of growth per cycle (GPC) is achieved. The same phenomena could, however occur at higher thicknesses. Which implies a form of secondary nucleation which temporary

increase the surface area. This phenomenon is described with an S-shaped curve which is shown in Figure 3.5.

3.1.3 Dependence of deposition temperature

The deposition temperature plays a crucial role on the phase content and microstructure of the deposited material. At a low deposition temperature the deposited film often turns out to be amorphous. At higher temperatures, films become crystalline, as reaction and mass transport kinetics increase with temperature - higher temperature allow diffusion of atoms and molecules more efficiently, and the mobility in the film also increases and influence the crystallinity of the deposited film. As discussed previously, the choice of precursor also determines the temperature interval for the ALD window (Figure 3.4).

Different precursor combinations can be used to obtain the same material but at different deposition temperatures. For example the combination $\text{TiCl}_4/\text{H}_2\text{O}$ produce crystalline films (Anatase, TiO_2) at temperature between 125 - 680 °C, whereas $\text{TiI}_4/\text{H}_2\text{O}$ gives anatase films between 165 - 375 °C [16].

The temperature can also influence the phase content of the deposited material. With $\text{TiCl}_4/\text{H}_2\text{O}$ the resulting film of TiO_2 becomes amorphous at temperatures below 165 °C, between 165 to 350 °C the film crystallise into the anatase phase, whereas above 350 °C the rutile phase is deposited [106].

Impurities in the film also changes with deposition temperature, often the impurities from the decomposition of the precursor decrease with increasing temperature.

3.1.4 Effect of different substrates

The substrates play a crucial role and strongly influence the growth in ALD. The substrate need to have suitable adsorption sites to initiate the growth during the first cycles. If the surface do not contain any suitable surface sites, no growth will occur. As described previously, in Section 3.1.1, the growth per cycle is often smaller during the first cycles, due to nucleation limitations on the surface. This phenomena often occurs when the substrate and the film is different, for instance a metal on an oxide or a nitride on an oxide. But also when depositing oxide on an oxide this phenomena can be observed. One reason for this could be a large difference in the lattice parameters, or if a large precursor, with large side groups block the surface sites on the substrate.

Usually at least three different possibilities of the initial growth of a thin films are observed [107]. The three different modes are called: Volmer-Weber growth, Stranski-Kratanov growth and Frank-van der Merwe growth. These are schematically drawn in Figure 3.6. When Volmer-Weber growth is observed islands form on the surface, since the adsorbate-adsorbate interaction is dominating in the system. The deposited material start to nucleate on the

surface and islands are then formed. This growth mode is present when the deposited material are more strongly bound to each other than to the substrate. The Stranski-Krastanov growth mode, starts with forming a monolayer on the substrate, or a couple of layers. After a few deposited monolayers the layer growth becomes unfavourable, and islands starts to form on top of the deposited monolayers. The cause for the island formation could be the lattice parameters, symmetry, or orientation in the monolayers in a way that a continuing growth into the bulk crystal motif is unfavourable. This results in a high free energy at the interface which favours island formation. The last growth mode is the Frank-van der Merwe growth. Here the deposited material is more strongly bound to the substrate. Substrate-adsorbate interaction is stronger than adsorbate-adsorbate. This produces a monolayer on the surface which continue to grow layer by layer.

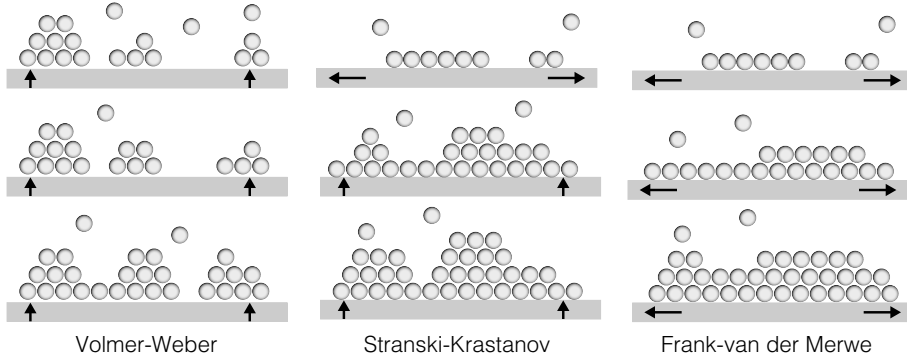


Figure 3.6. An illustration of the three growth mode. left) Volmer-Weber growth, middle) Frank-van der Merwe growth and right) Stranski-Krastanov growth. The arrows in the figure illustrates the primary growth direction.

This classification of growth modes do not account for if, and how, crystallinity occurs. As previously discussed the substrate also influences the growth, *e.g.* yielding amorphous or crystalline growth. In this case there are also three different schemes identified in the literature [16]. The first suggest that films start to grow initially as an amorphous film, containing randomly distributed atomic clusters that transitions into crystallites. As the films continue to grow crystallites grow larger, almost like a wedge in the amorphous material, growing into larger particles. The particles increase in size, to the point where neighbouring crystallites come in contact with each other. From this point on, the film continues to grow as a crystalline material. The growth per cycle is fairly constant during this proposed scheme, but the film would still be mostly amorphous at the interface between the substrate and the film. An example where this is present, is deposition of ZrO_2 and HfO_2 from alkyl amide precursors (tetrakis(dimethylamido)zirconium and tetrakis(dimethylamido)hafnium) [108].

The second proposed scheme is an extension of the first, where the amorphous material crystallise more homogeneously, as more cycles is deposited [16]. These films will be crystalline and like the first scheme a linear growth per cycle value would be expected. This is similar to an annealing of amorphous films to crystalline films, where the crystallinity expands from initial crystallites to the an crystalline film. This scheme well describes the growth of TiO_2 from TiCl_4 and H_2O on various substrates [106, 109–111]. The third and last scheme is similar to the Volmer-Weber growth discussed previously. The growth starts to nucleate at randomly distributed sites on the substrate. The growth continues with growth on the deposited material, giving islands as a result. At the beginning the substrate is therefore not fully covered of the deposited material. The islands then coalesce into a film, when the islands grow into each other, and first then forming a uniform film. This scheme is proposed by Nilsen *et al.*, from calculations [112–115]. This scheme has a lower GPC compared to an ideal ALD process, and has a similar behaviour as the s-shaped curve described previously (Figure 3.5).

When crystalline films are deposited by ALD a columnar growth, with different orientation of the grains, is often observed. When fewer chemisorbed nuclei are present on the surface the grains will be larger, since larger grains must grow before they can coalesce. Smaller grains are grown if many nuclei's are present. The grains will have different orientations, but it is common that an enhanced growth direction is present in a polycrystalline material, often influenced by the substrate. Epitaxial films are also possible to deposit with ALD, and is strongly influenced of the substrate used, and how the substrate is prepared. One example of epitaxial growth is ALD of NiO (100) or (111) films deposited on either MgO (100) or $\alpha\text{-Al}_2\text{O}_3$ (001) using bis(2,2,6,6-tertamethyl-3,5-heptanedionato) Ni(II) and water as precursors [116].

3.1.5 Design of ALD reactors used in this thesis

The thin film depositions described in this thesis were carried out in two different ALD reactors. The first reactor was an in-house built hot walled tube reactor, illustrated in Figure 3.7. The reactor has four furnace zones (indicated with a-d in Figure 3.7), which could be individually controlled, and monitored throughout the deposition. The system consist of three quartz tubes with different diameters and lengths, marked with numbers in Figure 3.7. The inner tube (1) is where the solid precursor is placed and sublimated (zone a). The temperature and gas flow regulates the amount of the precursor which is evaporated at each pulse.

The second quartz tube (2) separates the precursor pulses from each other. The carrier gas flows continuously throughout the whole process in all the quartz tubes, except when the second precursor is introduced. The inner tube then flow in the opposite direction, so called back flow. While the inner tube

gets another direction of the gas flow, the middle tube maintain a flow direction of the carrier gas towards the sample holder and prevents the first precursor from reaching the substrates.

The outer tube (3) contains the sample holder, and here the second precursor is introduced. As the second precursor often is a gas, or a liquid, the amount is regulated using pneumatic valves. The sample holder was custom made and could take up to five samples at the time.

The reaction zone where the ALD growth is obtained is often at a specific distance from the entrance. This region could be changed with the mass flow of the incoming carrier gas. This ALD reactor was designed for deposition temperatures up to 1000 °C.

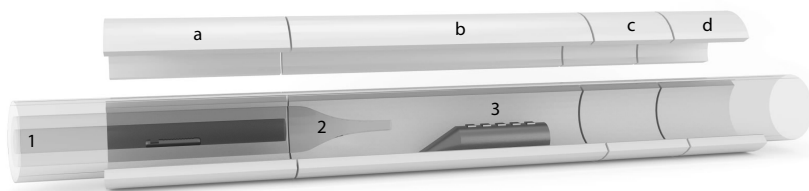


Figure 3.7. The hot walled tube reactor used during this thesis. Flow direction is to the right in the figure.

With this setup it is possible to separate the two precursors which can prevent any CVD growth from a mixture of the precursors (if preferred, this reactor design also permits CVD). The time for each precursor step can be changed with a computer, that controls the necessary pneumatic valves. From the end of the outer tube a vacuum pump is connected to regulate the pressure.

The second ALD reactor used in this thesis was a Picosun R-series reactor [117]. The deposition chamber is shown in Figure 3.8. The Picosun is a hot wall, top flow reactor with different individual inlets of the precursors into the deposition chamber. The different inlets are illustrated in Figure 3.8. The carrier gas is continuously flowing in all the four inlets during the deposition. A computer controls the pneumatic valves, precursor temperatures and the temperature of the deposition chamber. Since the setup provides four individual feed lines, up to four precursors could be used, as well as an extra gaseous precursor (O_2). The precursors are stored in cylindrically formed containers with heating or cooling possibilities, depending on the precursor used. Since the system is more compact than a tube reactor, the pulse lengths can be shorter. Also the distance between the precursors to the deposition chamber is shorter. The sample stage is shown in Figure 3.8 and can accommodate substrates up to 4 inches in diameter. Deposition on a large area substrate can produce a gradient in the thickness of the film, with greater thickness closer to the precursor inlet. The maximal temperature which could be used in our Picosun reactor

was around 450 °C. The vacuum pump line is beneath the deposition chamber. More information regarding the Picosun reactor can be found on the company web page [117].

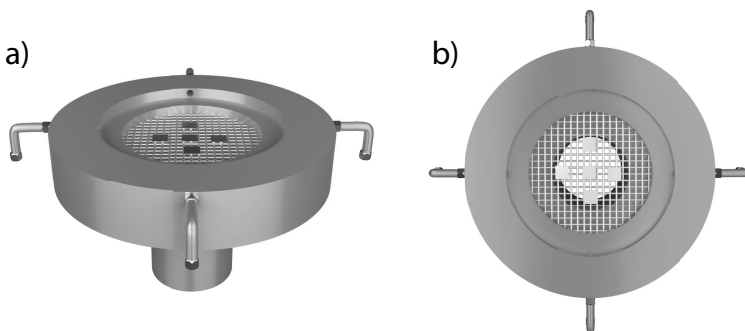


Figure 3.8. Illustration of the deposition chamber in the Picosun. (a) A side view of the chamber and (b) top view.

3.1.6 Deposition parameters for the deposited films

Titanium dioxide (TiO_2)

The TiO_2 was deposited in the hot walled tube horizontal flow type reactor (Figure 3.7) using TiI_4 (illustrated in Figure 3.9) and H_2O as precursors. The precursors available for deposition of TiO_2 are many, as it is one of the most common materials deposited with ALD [16]. The TiCl_4 is a well suited precursor since it is a liquid at room temperature and have a suitable vapour pressure. This precursor has been tested in the hot walled tube reactor used in this thesis. But in some cases it etched the sample, which is not desirable. Therefore the TiI_4 were chosen as the Ti containing precursor. The ALD process using TiI_4 and H_2O as precursors are published by a few research groups [36, 118, 119].

In this case the deposition parameters had to be optimised, for a 3D structure as substrate. The synthesis of the Al rods used are described by Perre *et al.* in reference [120]. The deposition temperatures was 200 °C and 300 °C, since the nano rods otherwise could crack. The evaporation temperature of the TiI_4 was 108 °C. Nitrogen (N_2) was used as purge gas and the pulse sequence was 15 - 15 - 15 -15 seconds. The time of each step was set to 15 s due to the high aspect ratio substrate which can be seen from SEM images in Figure 5.5. The pressure was 6.7 mbar throughout the depositions.

Table 3.1. List of precursors reported for ALD synthesis of iron oxides. Abbreviation: YSZ - yttria-stabilized zirconia, SLG - Soda lime glass, CNT - Carbon nano tubes, Pt/Rh NW - Platinum or Rhodium nanowires, GS - Glassy carbon, FTO - Fluorine doped tin oxide

Iron Precursor	Oxygen Precursor	Substrate	Reference
$FeCl_3$	H_2O	Pt	[121]
$Fe(acac)_3$	O_2	YSL	[122]
$Fe(acac)_3$	O_3	CNT, Si, SiO_2	[123]
$Fe(thd)_3$	O_3	TiO_2 , Si, Al_2O_3 , MgO, SLG, Pt/Rh NW	[124–127]
$Fe(Cp)_2$	O_2	Si, Al_2O_3 , TiO_2 , ZrO ₂	[36, 128, 129], Paper IV
$Fe(Cp)_2$	O_3	Al_2O_3 , Si, SiO_2	[130–132]
$Fe(^tBuAMD)_2$	H_2O	Si, GS, glass	[133]
$Fe_2(^tBuO)_6$	H_2O	Al_2O_3	[130, 134, 135]
$Fe(CO)_5$	O_2	FTO, Si	Paper I & II
$CpFeC_5H_4CHN(CH_3)_2$	O_3	SiO_2 , Si	[136]
$Fe(2,4-C_7H_{11})_2$	O_3, H_2O_2	Si, FTO, fused Si	[137]

Iron oxides

The iron oxides was deposited in both the hot walled tube reactor and in the Picosun R-series reactor. The investigated precursors used to deposit iron oxide found in the literature are listed in Table 3.1, together with their references.

Depositions made in the tube reactor used ferrocene ($Fe(Cp)_2$) and O_2 as precursors while in the Picosun both the previously mentioned combination and iron pentacarbonyl ($Fe(CO)_5$) and O_2 were used. The precursors are illustrated in Figure 3.9. The ferrocene were chosen since it is stable at room temperature which made it easy to handle and to work with.

The sublimation temperature used for ferrocene were different between the two reactors used. In the tube reactor ferrocene was evaporated at 50°C, whereas in the Picosun the temperature were shifted from 120°C up to 150°C. The sublimation temperature for ferrocene had to be increased significantly to obtain any vapour during the depositions in Picosun. The temperature were also increased for each deposition. The reason for the higher evaporation temperature of the ferrocene in Picosun is believed to be a consequence of the experimental setup. The ferrocene was placed in a cylinder and used on the Picosun a number of times, making the actual ferrocene more densely packed compared with the tube reactor where new ferrocene was used at each deposition. This was also evident when the cylinder was taken out for cleaning. The powder which was put into the cylinder was more or less sintered into a hard dense body. The amount of ferrocene used in the tube reactor where 1 gram

at each deposition whereas in the Picosun the container were loaded with 25 grams.

The deposition temperature were varied between 350 °C and 400 °C in the tube reactor and 400 °C in Picosun, as it has been previously reported that hematite is the dominating phase at this temperature [93]. This temperature is, however, in the range where ferrocene starts to decompose [138], so a higher growth rate than normally achieved by ALD, is suspected. The films has, even with decomposition of the ferrocene, been reported to give conformal films with a good repeatability on 3D structures – as shown by Rooth *et al.* [139] and Soroka *et al.* [36].

Depositions were made on Si(100), Quartz in the tube reactor, and TiO₂, Al₂O₃, and FTO in the Picosun reactor. In the tube reactor the number of cycles varied between 25-200 with pulse lengths of 4–6–8–6 seconds, at a pressure of around 4 mbar. The depositions in Picosun had the same number of cycles applied but with pulse lengths of 1–12–16–12 and a pressure of 3 mbar. All the depositions used N₂ as carrier gas. The reason for the longer pulse lengths in the Picosun were to ensure that enough ferrocene could be sublimated at each pulse.

Precursors used in this thesis

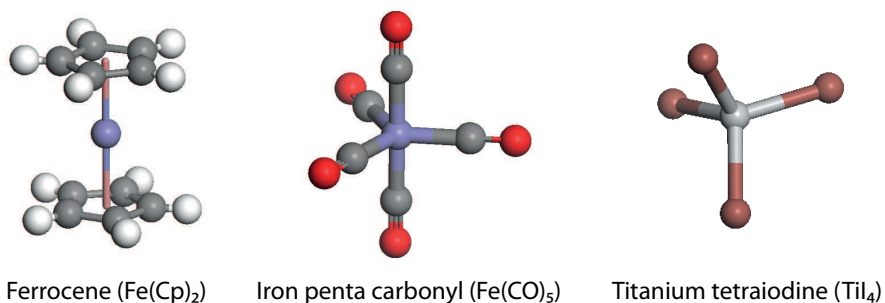


Figure 3.9. Illustration of the precursors used in this thesis.

The liquid precursor used for depositing iron oxide films were iron penta carbonyl, Fe(CO)₅. The Fe(CO)₅, which is a liquid at room temperature, was placed in a cylindric container and cooled to either 12°C or 15°C. This was to reduce the amount of Fe(CO)₅ at each pulse since the vapour pressure is 28 mbar (at 20°C) [140] which is too high, compared with more frequently used precursors as TiCl₄ which has 12 mbar (at 20°C) [141] and trimethyl aluminium (TMA) which has 11.6 mbar (at 20°C) [142].

During the deposition the Fe(CO)₅ decomposed on the way from the precursor container to the deposition chamber. This was probably caused by the heating elements of the deposition chamber being too close to the tube where the Fe(CO)₅ was transported into the chamber. The decomposition of the iron precursor could be reduced by lowering the deposition temperature, but in that case the iron oxide would most probable be amorphous instead of the desired

α -Fe₂O₃ phase. However, the decomposition was observed at temperatures as low as 100 °C. To control and to be able to handle the decomposition of the Fe(CO)₅, a glass tube, was inserted in the stainless steel tube and was changed after each run. The deposit in the tube was elemental Fe which can be seen from the XRD pattern in Figure 3.10. Even though decomposition of the Fe(CO)₅ occurred, the two precursors was separated with a purge pulse in-between. The process is therefore more correctly referred to as a pulsed chemical vapour deposition (pCVD [143]). Because of these peculiarities with the Fe(CO)₅, a constant growth per cycle was not achieved.

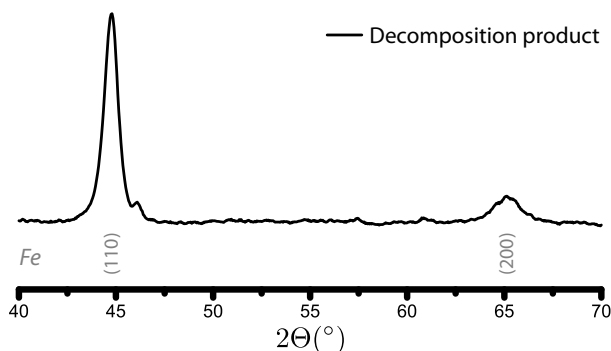


Figure 3.10. Diffraction pattern of the decomposition product from Fe(CO)₅. The ordinate axis' units are arbitrary.

The deposition parameters was set to 0.1–5–3–5 seconds for each cycle, with 0.1 seconds for Fe(CO)₅, and 3 seconds for O₂. The deposition temperature was 300 °C and the total pressure 7 mbar. The Fe(CO)₅ used were purchased from Fisher scientific with a purity of 99.5% and the oxygen used was from an in house supplier with a purity of 99.998%. The carrier gas used during these experiments were N₂, having a purity of 99.999%. As an attempt to reduce the decomposition of Fe(CO)₅, carbon monoxide were also tried as carrier gas during a set of depositions. The result of these experiments are described in Section 5.4.

4. Characterization Techniques and Experimental Details

This section summarise the analytic techniques used in this thesis. X-ray diffraction (XRD) and Raman spectroscopy were mainly used for phase determination. Scanning electron microscopy (SEM) were used for visualising the deposited films and the change in morphology. Transmission electron microscopy (TEM) were used for evaluating the film, with respect to film conformality on 3D substrates. The TEM analysis were performed in collaboration, thus this technique will not be described. X-ray fluorescence (XRFS) were used together with X-ray reflectivity (XRR) to measure the thickness of the deposited iron oxide. UV-vis absorption spectroscopy were used for optical absorption and band gap measurements. Hard X-ray Photoelectron spectroscopy (HAXPES)/X-ray photoelectron spectroscopy (XPS) were used for evaluating the deposited films, regarding their chemical compositions. HAXPES were used for analysing possible diffusion from the substrates into the deposited films. The HAXPES technique is more thoroughly described, as it is believed that this technique is not as common as the other techniques used in this thesis.

4.1 X-ray Diffraction (XRD)

X-ray diffraction is a widely used technique to characterise crystalline materials. The technique is routinely used in both industries and in research facilities to identify polycrystalline bulk material and thin films [144, 145]. XRD can also give information about particle size, relative crystalline orientation, lattice parameters and strain or stress in a material. Figure 4.1 illustrates the basics of an XRD apparatus.

XRD uses the fact that a crystalline material consists of atomic planes which are spaced with a distance d (Figure 4.1), and can be resolved into many characteristic distances between lattice planes in the material, each with a different d -value, illustrated in Figure 4.2 c). To denote planes, Miller indices are used. A set of lattice planes can be indexed with the Miller indices h , k and l . With the meaning a/h , a/k and a/l , where a is the unit cell's edge. This specifies the point of intersection of the lattice planes with the unit cell edges.

The distance between two planes is given by spacing, d_{hkl} , with hkl referring to the Miller indices. For a cubic lattice the inter planar distance depends on the unit cell edge, a , and the Miller indices according to:

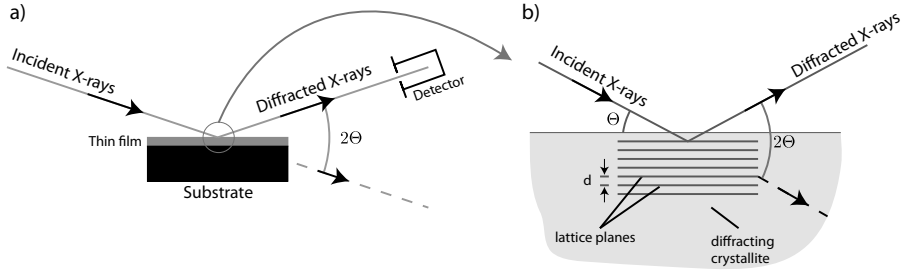


Figure 4.1. a) Basic features of a typical XRD experiment. b) is a magnification of a) illustrating the incoming angle(θ), distance between the lattice planes (d) and the measured angle in XRD (2θ).

$$d_{hkl} = a / \sqrt{h^2 + k^2 + l^2} \quad (4.1)$$

When there is constructive interference from the incidence X-rays scattered by the planes in a crystal, a diffraction peak is observed at a specific angle (θ). The angle for constructive interference from planes with a d -value is given by Bragg's Law [6]:

$$\lambda = 2d_{hkl} \sin \theta_{hkl} \quad (4.2)$$

where λ is the wavelength of the incoming X-rays. To be able to measure the diffracted beam the detector must be positioned in the angle 2θ , indicated in Figure 4.1 b). The crystal also has to be oriented so the surface normal to the plane is coplanar with the incident and the diffracted X-rays. So the angle between the diffracting plane and the incident X-ray is equal to the Bragg angle θ_{hkl} . The Bragg angle is defined as the angle where the peak with the maximum intensity is observed.

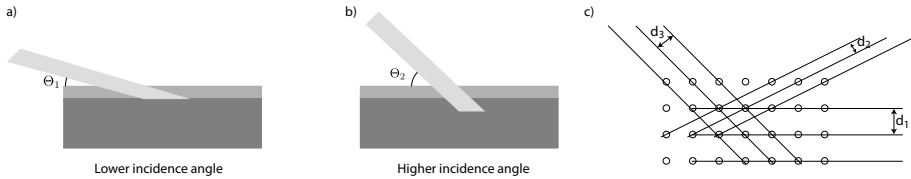


Figure 4.2. a) and b) GIXRD illustration of how the incidence angle penetrate different depths in sample. The left figure has a lower incidence angle, making it more surface sensitive, comparing with the right illustration with a higher incidence angle. c) Several lattice planes and their d -spacing in a cubic structure.

For thin films, grazing incidence XRD (GIXRD) is a useful method [146]. With a low incoming angle of the incidence X-ray maximises the diffraction of the thin film and minimises the background. This is illustrated in Figure 4.2 a) and b), where a) has a lower incidence angle and thereby measure a

larger portion of the thin film than when a higher angle is used, as illustrated in b). GIXRD has been used to characterise films down to one monolayer. In GIXRD the incident angle is small, typically between 0.5° to 1° , and also the angular range used in this thesis. The X-rays then penetrate the top of the sample, the depth is strongly depending on the incidence angle used.

The other XRD setup used during this thesis is the locked couple (Bragg Brentano) geometry [146]. In this setup the incident angle and the angle to the detector is the same, as shown in Figure 4.1 a). Compared with GIXRD where the incidence angle is the same throughout the experiment, and the angle to the detector is ramped, the sample in a Bragg Brentano geometry is fixed, whereas the angle θ , is in this case shifted for both the incidence and the diffraction angle. With the locked couple geometry only lattice planes parallel to the surface give rise to diffraction. The locked couple ($\theta - 2\theta$) scans are extensively used for the investigation of polycrystalline materials.

In this thesis both GIXRD and locked couple ($\theta - 2\theta$) were used. The GIXRD was performed on a D5000 Siemens instrument and the $\theta - 2\theta$ was measured on both the D5000 Siemens but also on a Bruker D8 Advance. In all measurements Cu K α_1 ($\lambda = 1.54 \text{ \AA}$, $\hbar\omega = 8047.8 \text{ eV}$) radiation were used. An

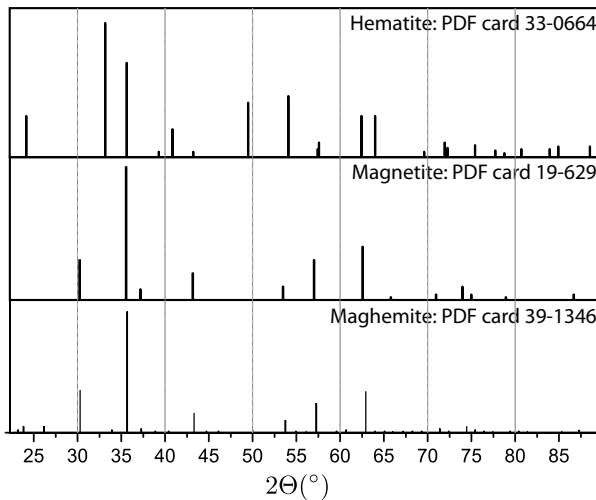


Figure 4.3. XRD patterns of hematite, maghemite and magnetite. Showing the similarities between the three polycrystalline iron oxides.

example of an XRD pattern is shown in Figure 4.3. Where reference data (PDF cards) has been used to illustrate the similarity of certain lattice distances in hematite, maghemite and magnetite. The similarities are described further in Section 2.2.1. The most intense peaks (at about $2\theta = 36^\circ$) of maghemite and magnetite have a very small shift, due to the fact that they both have a cubic unit cell with the only difference that the Fe ions is located in different sites. At almost the same position, hematite has its second most intense reflection.

In a thin film of an iron oxide it could therefore be difficult to determine which phase is present, only using XRD.

4.2 X-ray Fluorescence (XRF)

X-ray fluorescence is a nondestructive technique used primarily for elemental analysis [147, 148]. The sample is irradiated with X-rays with a fixed wavelength, which cause the sample to emit characteristic X-rays. The process is illustrated in Figure 4.6. Briefly, an X-ray with high enough energy knocks out an inner shell electron, resulting in a readjustment with an electron from an outer shell filling the vacancy in the inner shell. Simultaneously, a characteristic X-ray is emitted. The energy is dependent of the energy difference between the binding energies of the outer and the inner shell. This makes the technique element specific, since the energy differences in atoms are characteristic for each element. Almost the whole periodic system can be measured using XRF, from beryllium up to uranium, with a sensitivity of a few parts per million. An XRF system could differ in the setup but an X-ray source, a crystal spectrometer and a detector are the crucial parts.

As discussed, the X-rays need to have greater energy than the binding energy of the inner shell electron (for the inner shell photoionisation to occur). However, if the energy is too high many photons will simply pass through the substrate, only a few electrons will be knocked out since the cross section for photoionisation will be low. If the energy of the incoming X-rays lies closer to the binding energy of the sample's K-shell electrons, the fluorescence yield will increase. The highest yield is reached when the incoming energy lies just above the binding energy of the electron. If the energy is too low, no fluorescence will be observed.

Due to the fact that the incoming energy should be close to the binding energy a secondary target is used. The X-ray source then emits fluorescence from a target with photon energy slightly above the ionisation energy threshold of the sample. The penetration depth in XRF depends on the energy of the incoming X-ray's, but often the information depth is in the μm range.

When an inner core electron is knocked out two processes could occur, as illustrated in Figure 4.6. The probability of either that an Auger electron is emitted or an X-ray is strongly dependent on the atomic number of the material analysed. In Figure 4.4 it is seen that the X-ray yield increases with the atomic number (Z) [149]. When analysing a low Z element the probability is therefore larger that an Auger electron is emitted than that an X-ray. Therefore oxygen in Fe_2O_3 is difficult to measure as it produces almost no X-rays.

Except the information of which elements that are present in the film, XRF could also be used for quantitative measurements. The intensity of the emitted X-rays is proportional to the number of specific atoms present in the sample. To be able to do quantitative measurements a stable system has to be used.

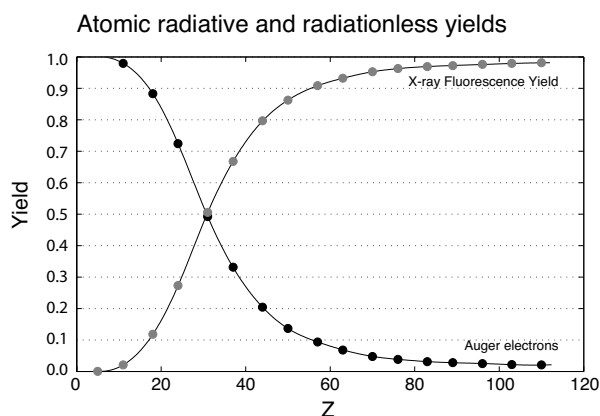


Figure 4.4. Illustration of how the X-ray yield changes with atomic number. Lower atomic number provides more contribution of Auger electrons, whereas higher Z provides more fluorescence.

The measured area and the sample position has to remain the same throughout the experiment.

The XRF equipment used in this thesis were a Epsilon 5, from PANalytical. A germanium target were used as it has a binding close to the energy of iron. For determining the thickness the Fe $K\alpha_1$ peak was used. The XRF signal was together with the XRR measurements calibrated from iron oxide deposited on Si(100) substrates (the calibration curve can be found in the supplementary information in Paper I). This calibration curve were used for all substrates. Some of the substrates used in this thesis had more surface roughness than the Si calibration. The thicknesses are therefore in some cases slightly overestimated. The roughness of the samples were still in the nm range, so the overestimation is believed to be small.

4.3 Raman Spectroscopy

Raman spectroscopy is a powerful tool for determining the phase of crystalline materials as well as characterising amorphous and molecular materials. In materials, the system vibrate with frequencies determined from the mass of the atoms and their bonds [150–152]. A large advantage with Raman spectroscopy is that the measurement, can be performed in air, and it is in most cases a non-destructive technique.

The experimental setup consist of an intense monochromatic light (Laser) beam, which interact with the sample. The electric field from the incoming light beam distorts the electron cloud in the structure, and stores it is energy for a short while. When the field is reversed, as the wave passes, the structure returns towards equilibrium, and the stored energy can be reemitted as pho-

tons. Most of the incoming radiation is reradiated at the same frequency as the incoming, this is known as elastic or Rayleigh scattering. A small portion of the absorbed energy excites or deexcites vibrational modes in the structure, and the reemitted photon is inelastically scattered, *i.e.* it has not the same energy as the incoming photon. A prerequisite for the vibration to be Raman active is that the polarisability of the electron cloud change during the vibration. This gives rise to Raman bands which can be measured with a photodetector. As discussed above, the Raman bands depends on the atoms and bonds in a material, and the Raman spectrum measured is therefore different for different materials. An example are the iron oxides $\alpha\text{-Fe}_2\text{O}_3$ and $\gamma\text{-Fe}_2\text{O}_3$, which has the same structural formula but different crystal structures. The two Raman spectra are completely different where $\alpha\text{-Fe}_2\text{O}_3$ has Raman bands at 225, 247, 293, 299, 423, 498 and 613 cm^{-1} and $\gamma\text{-Fe}_2\text{O}_3$ have broad bands at 350, 500 and 700 cm^{-1} . The difference is evident in Figure 5.15, as well in the supplementary information in Paper VIII.

The Raman instrument used in this thesis was a Renishaw micro Raman system using the 532 nm (green) line of an argon ion laser.

4.4 Scanning Electron Microscopy (SEM)

Scanning electron microscopy is a very common technique for visualising the morphology of a surface. With SEM one gets a higher magnification and a larger depth of field compared to an optical microscope. An optical microscope has a resolution limitation according to Rayleigh's criteria [153], which gives us the information of the smallest objects which could be resolved according to:

$$\delta = 0.61\lambda / \mu \sin\beta \quad (4.3)$$

where the wavelength (λ) of visible light is the limiting factor in an optical microscope (μ is index of refraction and β half angle of the maximum cone of light entering the lens). Since the wavelengths used is in the visible range the maximal resolution is around 300 nm (with blue light), Figure 4.10. When using an electron microscope, smaller wavelengths are reached. The resolution in an electron microscope is in practice limited by other factors, *e.g.* the aberration in the electron lens system. The wavelength of electrons is related to their momentum p (according to the relation given by de Broglie, $\lambda = h/p$ [154]), and thus depends on their energy (with E in eV) as $\lambda \approx 1.33/\sqrt{E}$. The resolution in a SEM is therefore theoretically, below 1 Å.

A typical SEM consists of an electron gun, anode, condensor lenses, objective lens, scanning coil, and an detector. The sample is under vacuum to elongate the mean free path of the out-coming electrons (as is done in electron spectroscopy experiments, as described below). As the technique is based on

electrons hitting the sample, a conducting material is preferred as it can transport the electrons down to the sample plate and avoid charging of the surface.

A SEM uses electron for visualising the surface of a sample. The electrons could either undergo inelastic scattering or elastic scattering. Elastic scattering implies that the incoming electron have been scattered without energy loss (but may change direction), by the nucleus of an atom. This is referred to as back scattered electrons, and have an energy close to the accelerating voltage. An inelastically scattered electron, lose some energy due to interactions or collisions in the sample, and therefore has lower energy than elastically scattered electrons. Due to the loss of energy the information depth for the inelastic scattered electron is smaller than the elastic scattered electrons.

The number of back scattered electrons increases with the atomic number of the atoms, akin to Rutherford scattering. This means that high atomic numbers appears brighter than a low atomic number [155], *i.e.* contrast do not only depend on topography. This is in some way an built in contrast that origins by the elemental differencies. The detector is often placed above the sample, as a "donut" with the incoming electron beam in the middle.

The advantage of using the inelastically scattered electron (secondary electrons) is that they give better information of the surface structure. Because of the low energy of the secondary electrons, often below 50 eV [155], the detector attract them using an electrically biased grid (positively charged). The brightness in the pictures origins from the amount of secondary electrons which hits the detector, less electrons gives a darker image.

The SEM used in this thesis were both a Zeiss 1550 and a Zeiss Merlin. The acceleration voltage were between 2-3 kV and the working distance were normally set in between 2-6 mm. The samples visualised using SEM had some surface structure, so even if a higher magnification than 200000 were possible, this was enough to obtain the wanted information. For an easier comparison between the images, the magnification was fixed within a figure in this thesis.

4.5 X-ray Photoelectron Spectroscopy (XPS) and Hard X-ray Photoelectron Spectroscopy (HAXPES)

Photoelectron spectroscopy (PES) is based on the photoelectric effect. The photoelectric effect is when negative particles are emitted from a surface which is exposed to light. This was observed by J.J Thompson in 1899. In 1886 Henirich Hertz discovered that electromagnetic radiation could be used to ionise atoms, but he did not offer any explanation of why this phenomena occurred [156]. In 1902, P. von Lenard observed that the emitted particles kinetic energy did depend on the frequency (color) of the light and not the intensity. The ionisation was described by the absorption of a "light quantum" and that different materials had different onset frequencies for electron emission. The incoming energy had to be large enough to overcome the first

ionisation potential of the material [157]. Einstein formulated the equation, which explained the photoelectric effect.

$$E_{kin} = \hbar\omega - \phi \quad (4.4)$$

Where E_{kin} is the kinetic energy of the photoelectron and is related to the frequency of the light and the work needed for the electron to escape from the material. \hbar is Planck's constant divided by 2π , ω ($\omega=2\pi f$) is the angular frequency of the light and ϕ is the work function.

In PES the kinetic energy of an ejected electron is analysed, and from the fundamental energy conversion equation, in photoemission the binding energy can then be calculated[158].

$$E_B = \hbar\omega - \phi - E_{kin} \quad (4.5)$$

Where E_B is the binding energy, $\hbar\omega$ the incoming energy, ϕ the work function and E_{kin} the measured kinetic energy of the electron. The work function for a solid is defined to be the energy separation between the vacuum level and the Fermi level of the measured sample. When the sample is a conductor, thermodynamic equilibrium between the sample and spectrometer requires that the Fermi levels, or electron chemical potentials should be equal. The common convention for the electron binding energy scale is to place its zero at the Fermi level.

The PES technique uses the fact that each element have specific energy levels. In this way it is possible to separate one element from another. Core level photo electron spectroscopy also gives information about the chemical state of the elements in the system, via the chemical shift – discovered by K. Siegbahn and co-workers [159]. Different valence contributions (covalent bonds etc.) gives a perturbation of the core level binding energies: this is called the chemical shift in X-ray photoelectron spectroscopy (XPS). In an qualitative way one may use the electronegativity of the other atom to predict if the chemical shift is positive or negative. This is an approximation which is not always valid, but may serve as a starting point. For instance, oxygen remove electron-density from *e.g.* Sn. The electrons in the Sn core levels then experience less screening of the nuclear charge than it normally does in a pure Sn environment. The core electrons of Sn in SnO_2 should then be bound harder to the nucleus due to the increased attraction from the Sn nuclear charge. This effect shifts toward higher binding energy, and can be seen in Figure 5.2. If the "ligand" is electropositive the added electron density induce a shift towards lower binding energies.

The PES experiments are conducted in vacuum, which increase the mean free path of the electrons, which reduces the possibility for the emitted photoelectron to scatter on the way to the detector. PES can be used to analyse the energy levels in atoms in gases, in liquids or in solids. During each experiment electrons are emitted from the measured sample. For gases and liquids

this is not a problem since they are continuously renewed. When measuring on a solid, electrons have to be transported to the measured solid, so it will stay neutral. This demands that the sample has a good conductivity, otherwise charging of the sample could occur, resulting in a shift of the binding energy. If the sample is not conducting, an electron gun could be used to neutralise the sample.

As described by Equation 4.5 for a certain photon energy, lower kinetic energy of the emitted photoelectrons gives a higher binding energy. In PES the amount of the emitted photoelectrons are counted as a function of kinetic energy. Every atomic level therefore gives rise to a peak in the measured spectrum. As seen in Figure 4.5 where both the binding and kinetic energy is indicated on the x-axis. Quantitative information could be determined, since the peak area is dependent on the number of emitted photoelectrons at a specific binding energy. Quantitative information is easier to obtain from a core level spectrum – valence levels need a theoretical model to be evaluated.

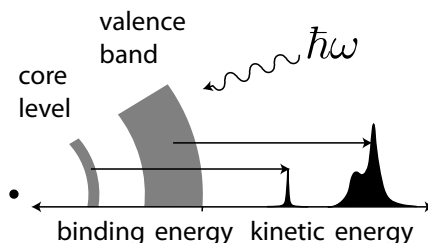


Figure 4.5. An illustration of an atom (to the left) and the corresponding XPS spectrum (to the right). [160].

Core level spectra interpretation

Except the intensity at different binding energies, a measured spectra also have photoelectrons which are inelastically scattered which is referred to as the background of the measurement. An example of this can be seen in Figure 5.1. The phenomena where the background rise after measuring a certain core level can be modelled with a Shirley type background [161].

In the previously described figure the main peaks for the Sn core levels is from an ionised atom in the ground state, shown in Figure 4.6. It is also possible that the resulting ion is in an excited state, where the photoelectron excite valence electrons. When this occur the photoelectron will reduce in kinetic energy resulting in a shake up at the higher binding energy side of the core level measured. The difference between the shake up and the main core level peak strongly depend on the sample measured.

When the photon energy is chosen so a core hole is created, the hole is filled with an electron from an energy level above the core hole and an Auger electron can be emitted. The Auger electron comes from an outer energy level, shown in Figure 4.6, and the kinetic energy is the difference between the initial ion and the double charged ion. Therefore the Auger electrons have a constant kinetic energy and the photoelectrons have a constant binding energy when the photon energy is varied.

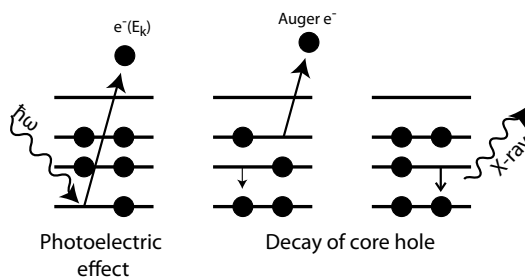


Figure 4.6. The creation of a photoelectron and a core hole (left) and subsequent core hole decay through emission of an Auger electron (middle) or a photon (right).

Spin-orbit coupling

The core levels measured with PES are indicated using the main atomic quantum numbers ($n = 1, 2, 3, \dots$) and the angular momentum quantum number ($\ell = 0, 1, 2, 3, \dots$ i.e. s, p, d, f, \dots) of the energy level whether the photo electron originates. The splitting of a peak in two components, for example Fe $2p$ which both has an Fe $2p_{3/2}$ and an Fe $2p_{1/2}$ component that arise from the coupling of the orbital and spin angular momentum. The splitting is observed for all levels, except s -states, associated with the two possible states of the quantum number j ($j = \ell \pm s$, with $s = \pm 1/2$) [162]. The intensity change between the two spin orbit components is dependent on the degeneracy of the state.

Chemical shift

The electrons in the material are only emitted if the incoming photons have energies larger than the electron binding energies. The binding energy of an electron is specific for each element/orbital and makes it possible to measure specific element with PES. Materials also have unique electronic structures and could therefore be used to obtain information at the atomic level. The binding energy is also influenced by the chemical bonding in which the element participates. This makes it possible to separate the binding energy between pure metal-metal bonding, metal-oxide, metal-sulfur, metal-nitrogen for example. This is valid as long as the resolution is high enough for separation. In an experiment the emitted electrons are counted in a chosen energy range. This gives rise to the intensity versus binding energy curve.

The resulting broadening for a peak in an experiment consists in the simplest case of a Gaussian and Lorentzian contribution. The Gaussian part comes from the used instrument and other experimental conditions, while the Lorentzian part is specific to what binding energy and what material which is analysed. It also depends on the life time of the singly ionised state.

The line shape therefore has two symmetric contributions and can be modelled by a convolution of both, this is called a Voigt function.

In metals the ejection of the photoelectron may excite electrons in the partially filled uppermost band, the photoelectron then loses some energy, this

gives an asymmetric line shape on the higher binding energy side. This is described by Doniach-Šunjić's line shape [163].

In insulators and semiconductors asymmetric line shapes may also arise if Auger electrons interact with the photoelectrons, so called post collision interaction (PCI) (see *e.g.* [164] and references therein). This process give rise to loss of kinetic energy of the photoelectron, and an increase in energy for the Auger electron, if the photoelectron's kinetic energy is smaller than the Auger electron's from the outset. The amount of PCI is thus highly photoenergy dependent, in contrast to the asymmetry occurring in line shapes of metallic systems. In a metal the change of the cationic state between photo and Auger electrons emitted is effectively screened which diminish the PCI-effect.

The cross section value reflects the probability that incident photons cause ionisation from a core level of a specific element and are therefore dependant on what energy the incoming photons possess. Cross section values are measured or calculated from theory and could be found in literature, or in several databases [165, 166].

Information depth

The intensity in PES depends of the information depth from where electrons can escape. This is linked to the electron mean free path in the material studied, defined as the average distance an electron can travel in a material without any energy loss. The intensity of the emitted electrons decay is a function of the distance d that the electron has to travel. This decay follows the Beer Lambert law:

$$I(d) = I_0 e^{(-d/\lambda \sin(\theta))} \quad (4.6)$$

I_0 is the intensity of the electron at the depth d , λ is the inelastic mean free path for the measured element, θ is the angle between the sample surface and the emitted electron, Figure 4.7 a)-c).

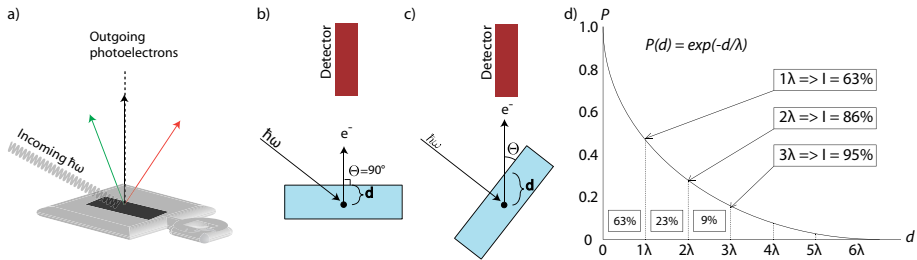


Figure 4.7. a) Illustration of the sample holder used in the HAXPES measurements during this thesis. b) Normal emission mode, 90° between the samples surface and the detector. c) illustration of how the information depth decrease when the angle between the detector and the surface of the substrate is smaller than 90°. d) Intensity of the emitted electrons as a function of depth of the analysis. Valid in normal emission.

The ratio of $I(d)/I_0$ could be seen as the probability that a photoelectron emitted from the depth d , escapes without any inelastic energy loss. When the angle between the surface and the outgoing photoelectrons are 90° it is called normal emission. In Figure 4.7 d) the relation between $I(d)/I_0$ and the inelastic mean free path is plotted. As seen in the figure, 95% of the intensity are emitted from depths between 0 and 3λ . This is valid for normal emission and for a homogeneous material. In this thesis, normal emission was chosen during the HAXPES measurements, whereas an angle of 45° were used during the measurements with Al $K\alpha$ radiation at the in-house XPS experiments.

The inelastic mean free path depends on the kinetic energy of the emitted photoelectron. This will therefore be different for all elements, and core levels of an element. This dependence is usually given from the universal curve, Figure 4.8. There are models proposed in literature [167, 168], which infer that a common curve is not valid for all systems, and a difference exist between inorganic/organic materials, as well as single elements/molecules. The curve is still a practical tool, giving an indication of the inelastic mean free path for the photoelectrons at a specific kinetic energy. And the curve always have the same qualitative appearance, where the inelastic mean free path increases monotonically with kinetic energy after around 50 eV.

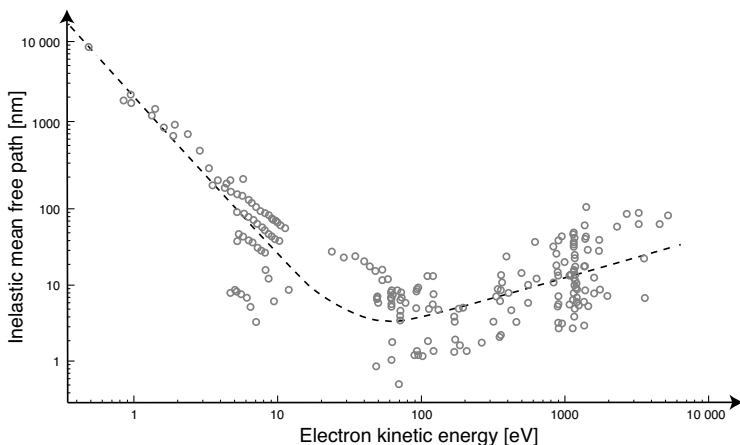


Figure 4.8. The inelastic mean free path of the photoelectrons, for inorganic material vs. kinetic energy [167]. Note that both axes are logarithmic.

The incoming photons penetrate a large volume of the sample (photons are considered, at the energies considered, to have a mean free path in the μ range), and the limiting factor for the intensity is the inelastic mean free path of the emitted photoelectrons. When using Al $K\alpha$ radiation the maximal information depth is reached at 1487 eV in electron kinetic energy. This corresponds to less than 10 nm in information depth for normal emission. At

Table 4.1. *The analysing depth (information depth) in the three iron oxides α -Fe₂O₃, γ -Fe₂O₃ and Fe₃O₄ at the photon energies used during this thesis [169]. The inelastic mean free path (λ) is the value in the parenthesis, whereas the information depth, 3λ , is the actual depth where 95% of the intensity comes from. 90° corresponds to normal emission.*

Photon energy (eV)	α -Fe ₂ O ₃	γ -Fe ₂ O ₃	Fe ₃ O ₄
1487 (45°)	5.7 nm (1.9 nm)	5.9 nm (2.0 nm)	5.7 nm (1.9 nm)
1487 (90°)	8.1 nm (2.7 nm)	8.3 nm (2.8 nm)	8.1 nm (2.7 nm)
2005 (90°)	10.3 nm (3.4 nm)	10.5 nm (3.5 nm)	10.2 nm (3.4 nm)
3000 (90°)	14.2 nm (4.7 nm)	14.5 nm (4.8 nm)	14.2 nm (4.7 nm)
6015 (90°)	25.2 nm (8.4 nm)	25.8 nm (8.6 nm)	25.2 nm (8.4 nm)

45 ° the information depth is less compared to normal emission, illustrated in Figure 4.7 c).

In Table 4.1 the information depths for three iron oxides are compared, calculated with the TPPM-2M formula [169] using the Quases software, Quases-IMFP-TPP2M [170]. They are quite similar compared with each other but when the kinetic energy is changed the difference in the information depth is visible. As the information depth for Al K α is less than 10 nm this technique is very surface sensitive. At higher kinetic energy, the measured intensity include information from distances further into the film. The technique then becomes more bulk sensitive because the relative contribution from the surface becomes smaller.

4.6 Synchrotron radiation

Photoelectron spectroscopy requires X-rays with a defined photon energy. This could be achieved by an X-ray tube giving a fixed photon energy, *i.e.* Al K α = 1487 eV or Mg K α = 1254 eV. Or light emitted from a synchrotron source, which use accelerated electrons. In a synchrotron the light is polarised, tunable, has a high brilliance and can thus be focused to a narrow beam. In this thesis photoelectron spectra were measured with both Al K α radiation, and with X-rays from a synchrotron facility.

An illustration of a synchrotron facility is shown in Figure 4.9. The principle for a synchrotron is that charged particles, typically electrons, emit radiation when they are accelerated [171]. In a synchrotron storage ring this is achieved by accelerating the electron in a circular path at relativistic speed. The electrons are produced by an electron gun, where a cathode is heated, leading to an electron cloud. The electrons are then transported using an electric field to a linear accelerator, which accelerate the electrons to higher energies. A booster (Figure 4.9, 2) is then used to increase the energy even further. In the booster the electrons can reach up to several MeV, or even a couple of

GeV's. At this point the electrons are almost at the speed of light. After the booster they are injected in the storage ring.

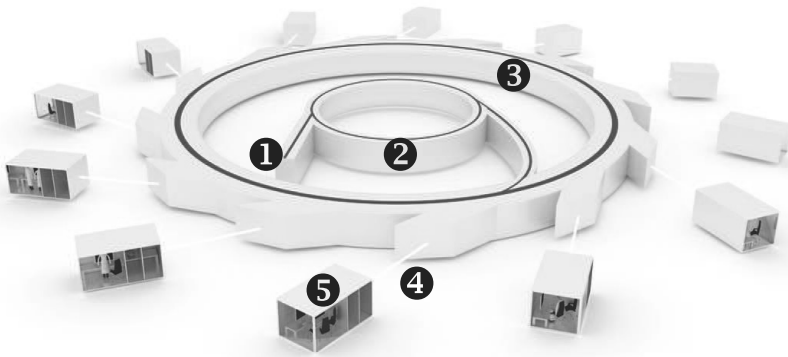


Figure 4.9. A schematic illustration of the main parts of a synchrotron. 1) electron gun, 2) synchrotron booster, 3) the storage ring with bending magnets and undulators/wigglers, 4) outgoing light from the synchrotron, 5) end station where the experimental setup is placed.

In the storage ring (Figure 4.9, 3), which is almost circular, there are magnets which bend the electron beam. When the electrons are accelerated they emit radiation. This is the most simple way to produce synchrotron radiation [172]. The linear acceleration of electrons is also less efficient [173].

The produced radiation contains a wide spectrum of energies, from IR to hard X-rays, shown in Figure 4.10. The more the electrons are accelerated, the higher the photon energy. When the electrons are in the storage ring they need to travel in an almost circular orbit. If the magnets used are too strong or too weak, the electrons will be bent out of the orbit. If magnets are used in series, the electrons can stay on the path of the storage ring. A consequence which occurs when the array of magnets is used is that the brilliance of the light increases, which leads to a high intensity in a small spot. The array of magnets used is called an undulator or a wiggler [174, 175]. They are located in straight sections in the storage ring, between the bending magnets. The difference between an undulator and a wiggler is that in the undulator the electron beam are being bent multiple times and do not deviate too much from the circular orbit and emitted light may interfere positively [172], which results in higher brilliance. A wiggler can use stronger magnets and thereby produce more energetic photons.

The photon energy of the emitted light is not only dependant on the acceleration of the electrons but also on the speed, or energy of the electrons present in the storage ring [174]. Higher photon energy thereby requires higher energy (speed) of the electrons. To maintain the electrons in a circular path at high energies, strong magnetic fields are required, or a large diameter of the storage

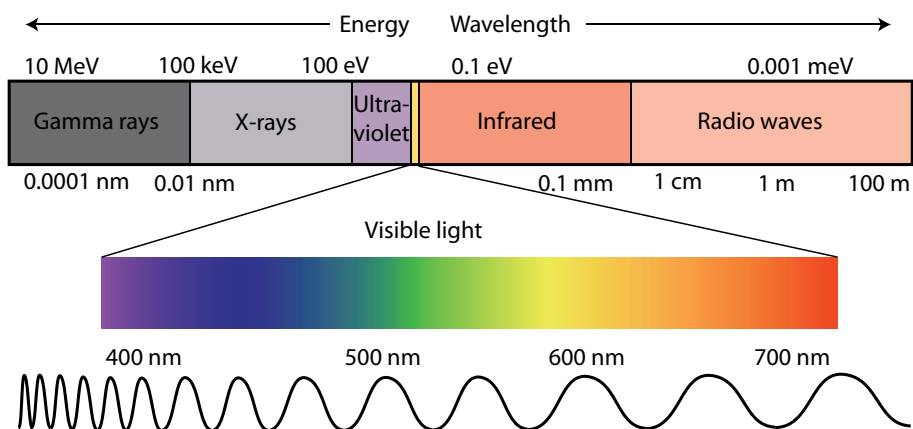


Figure 4.10. Illustration of how the electromagnetic spectrum is related to photon energies (eV) and wavelengths (nm) [176].

ring. The storage ring used for the experiments discussed here has energies of 3 GeV (HZB/Bessy).

The emitted light from the storage ring then passes through a beam line, indicated by the number 4 in Figure 4.9. Before it hits the sample it passes through a monochromator, slits and mirrors that focus the beam on the sample and define the photon energy. A crystal monochromator were used as it is suited for higher energies, at lower photon energy a grating monochromator is better suited. One definition of hard X-rays is when the grating monochromator no longer works, which occurs at energies above 2000 eV [177]. When hard X-rays are used the photon energy is tuned by using the Bragg reflections in a single crystal. An HAXPES beam line often operated between 2 and 10 keV where the upper limit is set by the maximal voltages in the photo detection spectrometer's hemisphere. At the end of the beam line the experimental setup is placed. In the measurements the HIKE end station [178, 179] at beam line KMC-1 were used [180]. An illustration of the end station used is shown in Figure 4.11.

Before the photoelectrons reach the end station they pass the monochromator. At this end station a crystal monochromator equipped with Si(111), Si(311) and Si(422) is used. The three different crystals are suited for a specific photon energy range, and can give photon energies between 2 - 12 keV. The light comes into the analysing chamber and hit the sample at a grazing incidence angle. The spectrometer is positioned so the surface normal of the sample is close to 90° (normal emission). This setup makes the technique more bulk sensitive, compared to an instrument where the spectrometer is placed in an angle below 90°. This can also be seen in Figure 4.7. The samples are introduced into a loading chamber, separated from the analysing chamber, and

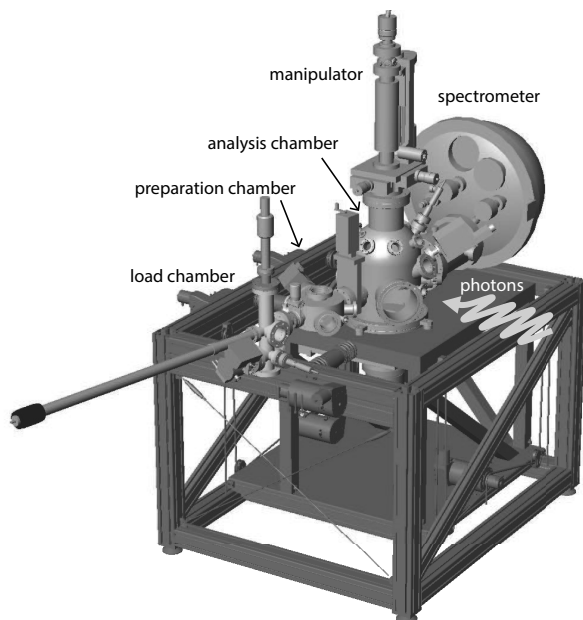


Figure 4.11. A figure showing the HIKE end station at KMC-1 at BESSY II [178].

then transported into the analysing chamber under vacuum. At this end station it is also possible to do experiments at elevated temperatures, and sputtering with Ar^+ ions. The manipulator in Figure 4.11 is used to position the sample.

The electron energy analyser used for the photoelectron spectroscopy experiments were a hemispherical Scienta R4000 10 keV spectrometer, configured to be able to measure high kinetic energy photons [181]. The detector is illustrated in Figure 4.12 a). The hemispherical electron energy analyser is based on two hemispherical electrodes, where the photoelectrons pass in between them, the trajectory of the photoelectrons is dependent on their kinetic energy. If the kinetic energy is too high or too low, the photoelectrons will end up in either the inner or outer hemisphere, illustrated with a cross section of the hemisphere in Figure 4.12 b). In the bottom (Figure 4.12 a) after the photoelectrons pass the hemisphere a detector is placed. The detector in the Scienta R4000 is a multichannel detector. Only the electrons with the kinetic energy close to the one following the radius of the central trajectory (*i.e.* hence the so called pass energy, E_p) between the hemispheres will hit the detector. A system of electrostatic lenses are placed before the hemisphere to either accelerate or retard the electron emitted from the sample. So that the kinetic energy of electrons with a certain energy can pass through the hemisphere and hit the detector. The pass energy, the entrance slit width (s) and the radius of the analyser (r_0) determines the resolution of the the spectrometer, see Equation 4.7. At each measurement made, the pass energy is set to a specific value, but the voltages for the lenses used for retardation or acceleration is changed in

order to scan over all possible kinetic energies. Equation 4.7 explains why different pass energies are used on different instruments, to compensate for that the radius of the analyser could change between spectrometers – if the resolution is to remain constant. For each measured energy the detector counts the electrons which results in the measured spectra.

$$\Delta E = E_p \frac{s}{2r_0} \quad (4.7)$$

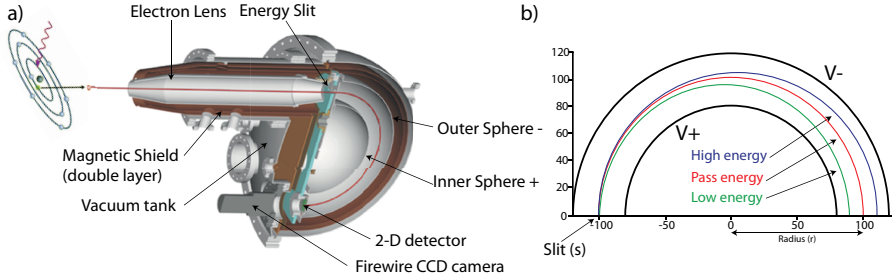


Figure 4.12. A hemispherical spectrometer of type Scienta R4000 10keV. The electron passes through a system of electrostatic lenses and the hemisphere before hitting the detector. a) Hemispherical spectrometer parts, b) Cross section of the hemisphere. Figure courtesy of VG Scienta AB.

4.6.1 Measurements with hard X-rays

During this thesis the HIKE (High Kinetic Energy electron spectroscopy) end station at beamline KMC-1 at Bessy II, Helmholtz Zentrum in Berlin was used [182, 183]. A double crystal monochromator were equipped with three crystal, Si (111), Si (422) and Si (311). In this thesis the Si (111) crystal were used because it gave us the best resolution at 2005 eV and 3000 eV. The measurements at 6015 eV were done with the same crystal but with the third order of light. The beam passed through a capillary resulting in a spot size on the measured sample of around 100 μm . The pressure in the analysing chamber was below 10^{-8} mbar and the pass energy was 200 eV. The analyser used was a Scienta R4000 with a 200 mm mean radius and optimised for high kinetic energies, up to 10 keV (Figure 4.12 a). The HIKE regime is general in the range of 2-12 keV in kinetic energy.

4.6.2 Experimental details for reference measurements of Sn, SnS, SnO, SnO₂, Fe₂O₃ and FeO.

The HAXPES measurements were performed at Bessy II using the KMC-1 beam line, described in Section 4.6.1. Photon energies used were 2005 eV and

3000 eV, the latter photon energy were used on all the Sn core levels, whereas 2005 were used for obtaining relative intensity difference between the two photon energies used.

The recorded spectra were calibrated using a gold standard with the knowledge that Au $4f_{7/2}$ is located at 84.00 eV [167]. The Lorentzian life-time width of the Au $4f$ core level used in the least square fit are found in reference [184]. All measurements were recorded in normal emission in the transmission mode of the analyser. Recoil effects of the photoelectrons are neglected, owing to the comparatively large mass of the Sn atom [185].

For an easier interpretation of the HAXPES measurements on diffused Sn and characterisation of the iron oxides, reference measurements were performed. The samples measured were metallic tin (Sn), SnS, SnO and SnO₂ to determine their position mainly regarding the Sn $3d$ and Sn $3p$ regions. But also for most of the core levels available when using 3000 eV in photon energy.

The powders used were fine grind and attached on a carbon tape to ensure good contact before introduced into the analysing chamber. The elemental tin sample was a foil and cut into a suitable size and mounted on carbon tape. For Sn and SnS, sputtering were necessary to get rid of surface oxides. The Ar⁺ ion sputtering parameters used for both these samples were 1 kV for 20 minutes.

The resulting binding energies were obtained from a least squares fit to the data using Voigt functions. For elemental Sn, Doniach-Šunjić's line shape was used [163], as it is a metal. A constant background and a Shirley-type background were used in all the fitting of the data [161]. The SPANCF macro package (E. Kukk) were used to carry out the least squares curve fitting.

Sn, SnS, SnO, SnO₂

The samples prepared for the reference measurements were purchased from either Alfa Aesar or Sigma Aldrich. The manufacturer and purities are summarised in Table 4.2. The purities of the powder samples (SnO, SnS and SnO₂) were also checked using XRD (Paper VI). The samples showed very high purity due to no other, or very weak peaks from other compounds were visible. This does not exclude any amorphous contribution to the samples, but is a good indication that the purity is high enough for using as references.

Table 4.2. *Supplier and purities of the measured samples.*

Compound	Purity	Supplier
Sn	99.9985%	Alfa Aesar
SnO ₂	99.9%	Alfa Aesar
SnO	99.99%	Aldrich
SnS	99.99%	Aldrich

Fe₂O₃ and FeO

Single crystalline FeO(100) and Fe₂O₃(0001) were used for reference measurements of the Fe 2*p* and O 1*s* regions. The single crystalline iron oxides were purchased from MaTeck. The samples were mounted with metal clips on the sample holder and no charging were observed from the measurements, evident from the constant energy difference between the Fe 2*p* and the Au 4*f* reference, used for calibration. The photon energy used during the measurements on FeO and Fe₂O₃ was 3000 eV.

4.7 UV-Visible spectroscopy / Optical absorption spectroscopy

The optical absorption was measured using UV-visible spectrometry. The technique measures the light absorption as a function of wavelength and could give information regarding the electronic transitions occurring in the analysed material. The portion of transmitted light for each wavelength is described by Beer-Lambert's law:

$$A = \epsilon cl = -\log_{10}(I/I_0) \quad (4.8)$$

where A is the absorption in the analysed material, ϵ is the molar absorptivity coefficient of the material, c is the concentration of the species absorbed and l is the length of light through the sample. I_0 is the incident intensity of the light and I is the dependant on the pathlength of light in the sample.

The absorbance could be normalised to the path length (l) of the light through the analysed film (*i.e.* the film thickness, the substrate are excluded), to obtain the absorption coefficient α [186], via Equation 4.9.

$$\alpha(\text{cm}^{-1}) = \ln(10) * A/l(\text{cm}) \quad (4.9)$$

For semiconductors this technique can be used to obtain optical band gaps, since it probes the transitions between the conduction and valence band. This band gap is not necessarily the same as the electronic band gap, though it is often assumed to be similar since there are few techniques which can measure the electronic band gap.

The band gap in a spectra corresponds to the point at which the absorption increases from the baseline. This is an indication of the minimum amount of energy required for a photon to excite an electron between the conduction and valence band, and thus be absorbed in the measured semiconductor. In an transmission experiment, the intensity is not only observed by the absorption of the material, also scattering and reflectance influence the measurement. These effects often occur when the measured film possess morphology, which will increase the light scattering. This effect is seen in the spectra if the baseline is above zero.

The direct transition can be evaluated by plotting the normalised absorption data (Equation 4.9) to the square root of the energy difference between the band gap and the photon energy (Equation 4.10). This is common known as a Tauc plot [187–189].

$$\alpha \propto c(h\nu - E_g)^{(1/2)} \quad (4.10)$$

From the measured optical absorption the square of the absorption versus the photon energy are plotted. The optical band gap could then be extracted by extrapolating the linear region found for photon energies slightly above the "expected" band gap down to the baseline.

For an indirect transition the same equation is used, with the difference that instead of a square root it is raised to two. Whereas the square root of the absorption is plotted versus the photon energy. By extrapolating the linear region down to the base (zero absorption) line in the spectra the indirect transition could be obtained. An example of the Tauc plot and the extrapolation of the linear regions are seen in Figure 5.27 a) and b).

A UV-vis spectra are typically reported with wavelength rather than the corresponding energy. The convention between wavelength (nm) and band gap (eV) could easily be transferred accordingly to:

$$h\nu(\text{eV}) = hc/e\lambda = 1239.8(\text{eV} * \text{nm})/\lambda(\text{nm}) \quad (4.11)$$

The UV-vis measurements in this thesis were performed on a Ocean Optics spectrophotometer, HR-2000+, with a halogen and a deuterium lamp. In all the measurements presented in this thesis a full spectrum between 190 to 1100 nm were measured. To obtain good statistics an average of 100 spectra were collected.

5. Results and Discussion

This section summaries both the results from the Papers included in this thesis, and result not yet published. The thin films depositions of titania and iron oxide are from Paper I, II, IV and V. The diffusion measurements are from Paper III, whereas Paper VI, VII and VIII are closely related and contain reference measurement of Sn, SnS, SnO and SnO₂, comparing depth profiling using HAXPES or use of Ar⁺ ion sputtering and a study of Sn core levels and their plasmon loss features.

5.1 Haxpes measurements on Sn, SnS, SnO and SnO₂.

The Sn, SnO, and SnO₂ substances were characterised around the Sn 3*d* and Sn 3*p* regions, because of the interest concerning the diffusion of Sn oxides in iron oxides, where Sn 3*p* overlap with the Fe 2*p* region, seen in Figure 5.22. SnS were also measured, since ALD of iron sulphides are planned to be studied later.

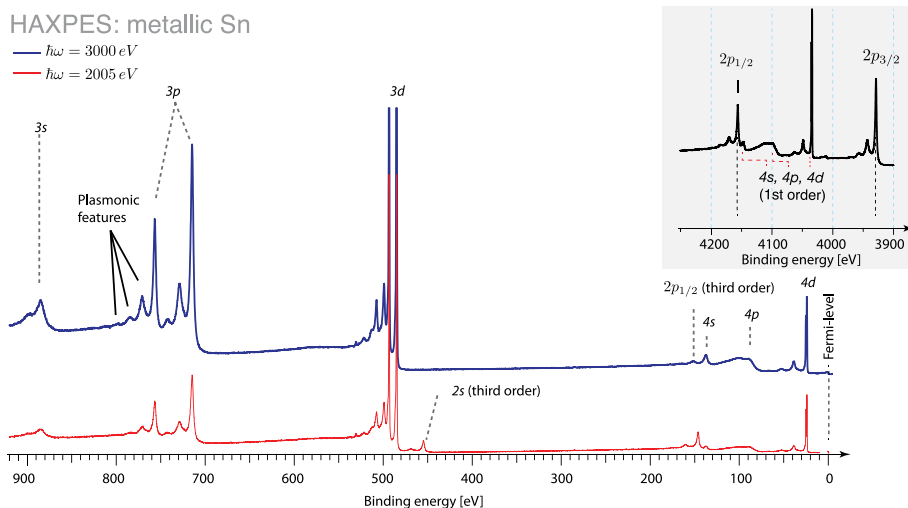


Figure 5.1. Survey spectra for metallic tin recorded at 2005 eV and 3000 eV photon energies. The Sn 2*p* region, inset in the upper right corner, have been recorder with 6015 eV photon energy (the third order diffracted light of the 2005 eV). The plasmonic loss features, accompanying each core level photoelectron line are indicated for the 3*p* level.

On metallic tin all the reachable core levels were recorded. They are shown in Figure 5.1(Paper VI). For the Sn 3d region the measured and fitted spectra are shown in Figure 5.2.

The metallic tin were sputtered in the analysing chamber, but a small amount of SnO were still present. This is evident from the shoulder on the higher binding energy side of both spin orbit components of Sn 3d, visible in Figure 5.2. The position of the spin orbit components of Sn 3d is 493.3 eV and 484.9 eV, and is in line with previous reported data, *e.g.* Barr [190].

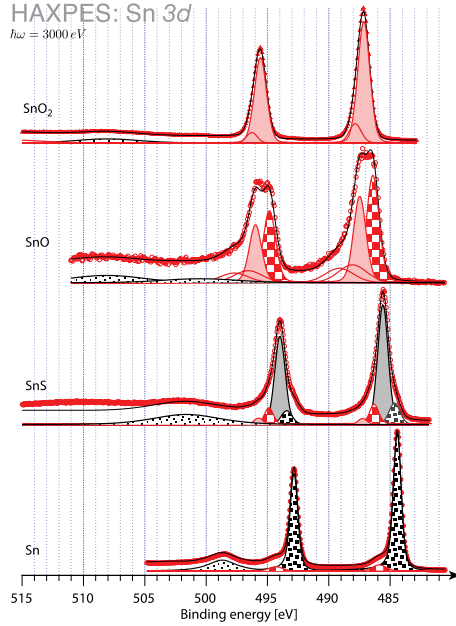


Figure 5.2. HAXPES measurement over the Sn 3d region using 3000 eV photon energy. Different shadowing in the fitting corresponds to one of the four measured samples. Sn - black squares, SnS - grey, SnO - red squares and SnO₂ - pink

The feature located 14.3 eV from the Sn 3d_{5/2} (Sn) are due to excitations of plasmons. This feature is marked with black dots, in Figure 5.2 and is an excitation of valence electrons upon photoionisation [191, 192]. This shift is well in line with previously reported data [193]. In Sn, every core level main line has an accompanying plasmon, visible in Figure 5.1. In Sn the excitation progression is distributed as exponentially decaying (discussed more thoroughly in Paper VII).

SnS were also sputtered, and both metallic tin and the Sn oxides were needed to obtain a good fit for the Sn 3d core levels (Figure 5.2). It is believed that the sputtering induce reduction of SnS to Sn to some extent, since sputtering damages is a known phenomena on sulphides, *i.e.* WS₂ [194]. The oxides present in the fitting is due to a shadowing effect when sputtering SnS. Even though the powder were finely grinded, this could occur. The position of

both spin orbit components of Sn $3d$ in SnS is, however, clear at 494.0 eV and 485.6 eV (Figure 5.2). The measured value for the Sn $3d_{5/2}$ from SnS are in good agreement with literature [195–197]. Other values of the Sn $3d_{5/2}$ have also been recorded, with a maximum shift of 0.9 eV from our value [198].

The SnO were not sputtered and had to be fitted with two components. For SnO there should, however, just be one component. The contribution on the higher binding energy side, the second component comes from SnO₂, which is evident from the fitting (Figure 5.2). The peaks were well separated and positions for the SnO were 494.8 eV and 486.5 eV (Sn $3d$). Additional peaks needed for a good fit (at higher binding energies), are marked with a black dotted area. These are assigned to loss features from SnO. This part did not change during the measurements.

The SnO₂ was fitted with one peak and a small feature on the higher binding side. These are effects from the sample where the powder was not in good contact with the carbon tape, leading to a small charging of that part of the sample, however, this part did not change during the measurement. The positions for the SnO₂ (Sn $3d$) were 495.6 eV and 487.2 eV.

For the SnO and SnO₂ a wide binding energy spread are found in the literature. Our values deviate 0.1 eV [199, 200], 0.5 eV [201] and 0.9 eV [202]. The closest binding energy found in literature are from Kövér *et al.* [203], where our values coincide for SnO and a shift of -0.1 eV for SnO₂.

The shift between the sulphide and oxides are expected as their electronegativity differs, where O is more electronegative than S.

The Sn $3p_{3/2}$ position of Sn, SnS, SnO and SnO₂ follow the same trend as the Sn $3d$ region, shown in Figure 5.3. From 714.7 eV (Sn), 715.1 eV (SnS), 716.0 eV (SnO) and 716.8 eV (SnO₂). The SnO have two components in the peak, where the peak on the higher binding energy side is from SnO₂, similar to the Sn $3d$ peaks for SnO.

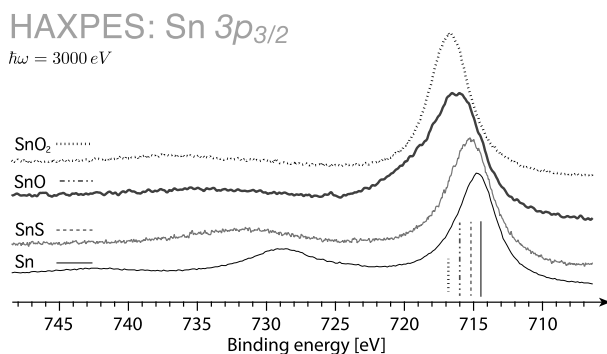


Figure 5.3. HAXPES measurement over the Sn $3p_{3/2}$ region using 3000 eV in photon energy. The vertical lines indicate the main line of the Sn $3p_{3/2}$ peak for the four measured samples.

The previously reported binding energy for the Sn $3p_{3/2}$ in SnS at 715.2 eV [196, 204] are in agreement with our observed value of 715.1 eV.

The positions of the $3p_{3/2}$, $3d_{3/2}$ and $3d_{5/2}$ for Sn, SnO, SnO₂ and SnS are summarised in Table 5.1.

Table 5.1. Sn core levels of Sn $3p_{3/2}$, $3d_{3/2}$ and Sn $3d_{5/2}$ for Sn, SnO, SnO₂ and SnS measured at 3000 eV. The units are eV for all Sn core levels.

Core Level	Sn	SnO	SnO ₂	SnS
Sn $3p_{3/2}$	714.7	716.0	716.8	715.1
Sn $3d_{3/2}$	493.3	494.8	495.6	494.0
Sn $3d_{5/2}$	484.9	486.5	487.2	485.6

5.2 Haxpes measurements on FeO and Fe₂O₃

The measurement over the Fe $2p$ and O $1s$ regions are shown in Figure 5.4. The positions for both the spin orbit components are well separated between the FeO and Fe₂O₃. In FeO the positions for the Fe $2p_{1/2}$ and Fe $2p_{3/2}$ are located at 723.3 eV and 709.7 eV, whereas for Fe₂O₃ they are shifted towards higher binding energy at 724.3 eV and 711.0 eV. This is close to the reported data by Grosvenor *et al.* [205] where the Fe $2p_{3/2}$ for FeO are at 709.5 eV and for Fe₂O₃ at 710.8 eV. Other values has also been observed for the FeO and Fe₂O₃ but are not positioned more than 0.2 eV from our values [206, 207].

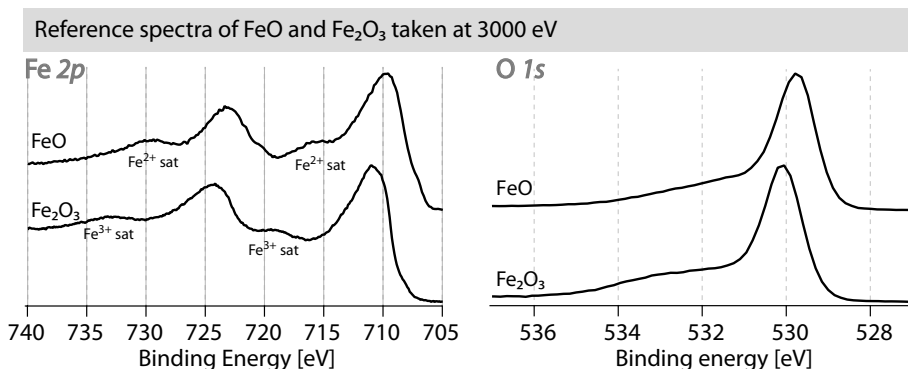


Figure 5.4. HAXPES measurement over the Fe $2p$ and O $1s$ region using 3000 eV in photon energy.

For the Fe $2p$ region a number of peaks were necessary to obtain a good fit. For an easier interpretation of the measured samples in this thesis the binding energy is given where the intensity is highest.

There is also a visible difference of the satellite structure, especially seen in between the two spin orbit components of Fe $2p$. For FeO, Fe²⁺ and in Fe₂O₃ the Fe³⁺ is present. The Fe²⁺ satellite is located at 715.4 eV and the

Fe^{3+} satellite is at 719.4 eV. This is also in line with Grosvenor *et al.* [205] where the Fe^{2+} were located at 715.4 eV (in FeO) and the Fe^{3+} at 719.3 eV (in Fe_2O_3).

The O 1s position for FeO and Fe_2O_3 were located at 529.8 eV and 530.1 eV. Literature values from reference [205] is for FeO at 529.9 eV and for Fe_2O_3 at 530.0 eV. Generally, the O 1s peak for iron oxides differs very little in binding energy: at 529.9 eV for $\gamma\text{-Fe}_2\text{O}_3$, $\alpha\text{-FeOOH}$, $\gamma\text{-FeOOH}$ and FeO, at 530.0 eV for $\alpha\text{-Fe}_2\text{O}_3$ and at 530.2 eV for Fe_3O_4 [205, 208]. The O 1s is therefore mostly used as a indication of molecules absorbed to the surface, *i.e.* water, CO, CO_2 , O_2 or hydroxyl groups, usually with binding energies above 530 eV.

5.3 Thin film deposition

In this thesis ALD/CVD of titania, alumina and iron oxides were investigated. The precursors used for the deposition of TiO_2 was TiI_4 and H_2O [36, 209]. For the iron oxide, both $\text{Fe}(\text{Cp})_2$ [139] and $\text{Fe}(\text{CO})_5$ [71, 210, 211] were used and O_2 was used as second precursor. The TiI_4 was used in Paper [V], $\text{Fe}(\text{Cp})_2$ in Paper [IV] and the $\text{Fe}(\text{CO})_5$ in Paper [I,II,III]. Trimethylaluminium (TMA, $\text{Al}_2\text{C}_6\text{H}_{18}$) and TiCl_4 were together with H_2O used to deposit TiO_2 and Al_2O_3 to use as substrates in the investigation of nucleation of the iron oxides.

5.3.1 Titanium dioxide (TiO_2)

The TiO_2 was deposited in the hot walled tube reactor, using TiI_4 and H_2O as precursors (Figure 3.7). The deposition parameters are described in Section 3.1.6. The substrate used were Al nano rods, with a high aspect ratio which can be seen from SEM images in Figure 5.5.

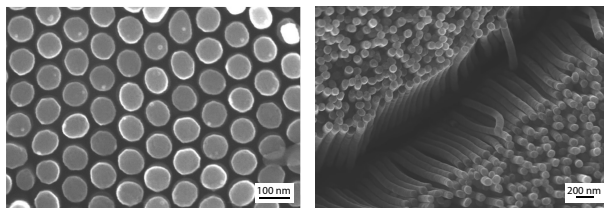


Figure 5.5. SEM images from the substrate used for the TiO_2 depositions. The left picture is a top view and the right image is to demonstrate the 3D structure of the aluminium substrate [120].

The resulting film deposited at 200 °C consisted of anatase in a amorphous matrix of TiO_2 . This is evident from comparing XRD (Figure 5.6) and the TEM images of the film (Figure 5.7). The strongest peaks is from the substrate and the smaller peaks corresponds well with anatase. From the TEM images

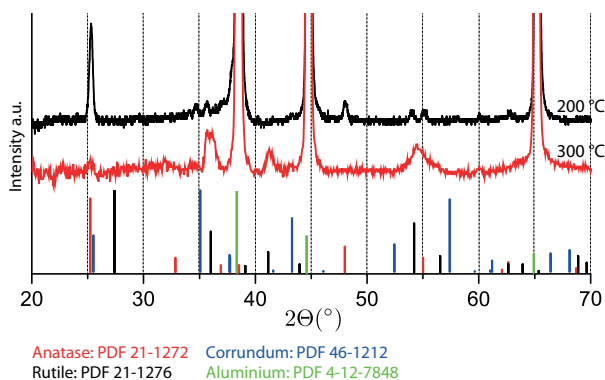


Figure 5.6. XRD on deposited TiO_2 at 200°C (black) and at 300°C (red). The identified peaks are indicated below the measured XRD. PDF cards are included in the bottom of the picture.

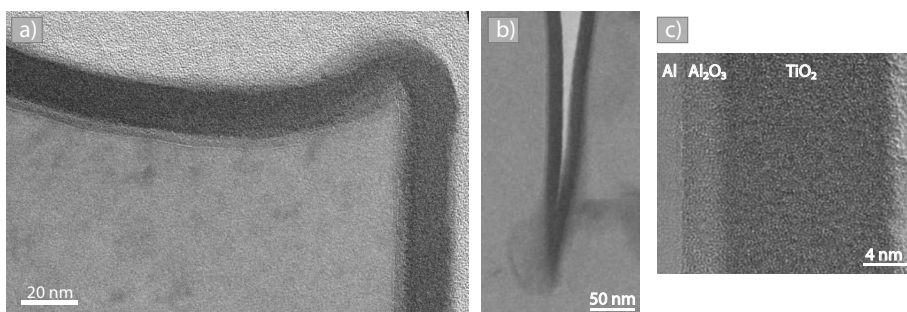


Figure 5.7. TEM images of the deposited TiO_2 film on top of Al pillars at 200°C. a) an image on the top of the nano pillar. b) presents a certification of that the film is covering the whole substrate, since it smoothly covering a deep trench. c) a cross section of the deposited film.

it is evident that a smooth film covered the whole substrate since both the top of the nano rods (Figure 5.7 a) and the trenches in between (Figure 5.7 b) the nano pillars are coated evenly with TiO_2 . The TEM also reveals a surface oxide of Al_2O_3 on top of the Al pillars. The thickness of the Al_2O_3 is around 4 nm and can also be seen from the XRD measurements, in the deposition at 300°C where the Al_2O_3 (012) diffraction peak is visible.

The film deposited at 300 °C showed peaks from rutile and especially the rutile (111) peak is visible which is not overlapping with either anatase or Al_2O_3 . Rutile has previously been observed at temperatures from 375 °C by Aarik *et al.* [209] using identical precursors as in our study. We believe that the substrate play a crucial role when forming rutile at 300 °C.

The sample examined with TEM (Figure 5.7) were deposited with 150 cycles at 200 °C, which gave a thickness of 17 nm. This corresponds to a growth rate of 1.1 Å/cycle which is slightly higher than values found in literature

[212], at this low temperature. Schuisky *et al.* had a growth rate of 0.5 Å/cycle at 230 °C and 1.3 Å/cycle at 455 °C [212], while Aarik *et al.* observed 1.0 Å/cycle at 200 °C and 1.2 Å/cycle at 300 °C [209]. The slightly higher growth per cycle (GPC) is probably caused by the substrate. The characterised material is best characterised by that of anatase in an amorphous matrix of TiO₂ when the deposition temperature is 200 °C and rutile at 300 °C.

5.3.2 Iron oxides (α -Fe₂O₃, γ -Fe₂O₃, Fe₃O₄)

The Iron oxide was deposited in both the hot wall tube reactor and in the Picosun R-series reactor. Depositions made in the tube reactor used Fe(Cp)₂ and O₂ as precursors while in the Picosun both the previously mentioned combination and Fe(CO)₅ and O₂ were used. The deposition conditions and parameters are described in Section 3.1.6.

5.3.3 The importance of the substrate during the deposition (Ferrocene as Iron precursor)

The in-house built hot wall tube reactor and Picosun were used for depositing iron oxide from Fe(Cp)₂ and O₂. The deposition parameters are described in detail in Section 3.1.6. The different substrates used for evaluation the importance of the substrate was Quartz (SiO₂), TiO₂, Al₂O₃, FTO and Si(100). The deposited films on Quartz, Si(100), TiO₂ and Al₂O₃ were analysed regarding growth rate per cycle, growth mode and phase composition. Whereas the films deposited on SiO₂ and FTO were analysed with Raman, XRD and SEM.

The thickness of all the samples was measured using a calibration curve made from XRR and XRFS, described in Paper I. Due to different surface roughness of the samples, the actual thickness will be overestimated for a slightly more rough surface, compared with a smooth. The difference should be constant regarding each substrate and correct conclusions could therefore be drawn.

Quartz as substrate

Figure 5.8 shows the as deposited samples and Figure 5.9 shows the annealed iron oxide films. From the SEM images in Figure 5.8 it is evident that the iron oxide film start to nucleate as islands on the quartz and coalesce to a film around a thickness of 22 nm. This is commonly referred to as Volmer-Weber growth [213], where particles form and coalesce to a film after a certain thickness. This is in contrast to Stranski-Krastanov [214] growth where a layer is formed on the substrate and particles grow on top of the deposited layer (Section 3.1.4). At 50 nm the deposited iron oxide forms a continuous film with some roughness.

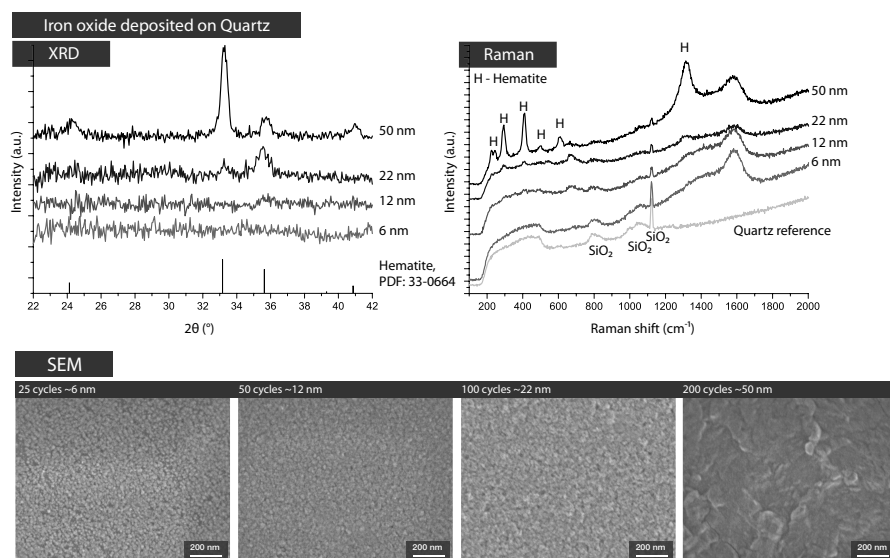


Figure 5.8. XRD, Raman and SEM images of iron oxide deposited on Quartz.

The thickness where the islands coalesce to a film (from SEM) correlates well with the thickness where Raman and XRD give rise to peaks from α - Fe_2O_3 . At lower thicknesses the film is amorphous or have a very small amount of crystallites which is difficult to detect with Raman or XRD. However, the signal from the Quartz substrate (included in the Raman at the bottom, Figure 5.8) decreases with the number of cycles applied, especially the peak at around 1100 cm^{-1} . This is a strong indication that the iron oxide film even at lower thicknesses occupy a large part of the surface. The peak visible at 1600 cm^{-1} is from a maghemite band [93]. Broad bands in this region are generally linked to magnetic properties of grains, this peak could therefore not be taken as a characteristic Raman band from maghemite vibrations [215] (since maghemite is ferromagnetic at room temperature (section 2.2.1)).

After annealing at $400\text{ }^\circ\text{C}$ for 2 hours in air the 12 nm film crystallised to α - Fe_2O_3 , evident from both the XRD and Raman measurements. The film which was 22 nm also gave more intense peaks from XRD and especially from the Raman measurements. A possible cause for the more defined in the 12 and 22 nm case is that the deposited material had time to coalesce and in that way form larger areas and larger crystallites. The Raman band at 1600 cm^{-1} were not present in any of the Raman spectra after annealing, indicating that the effect described above was valid. The XRD pattern also showed more narrow peaks compared with before the annealing step. A phase transition from maghemite to hematite normally occurs at $400\text{ }^\circ\text{C}$ [93], which was the annealing temperature used here. Since maghemite and hematite XRD pattern has

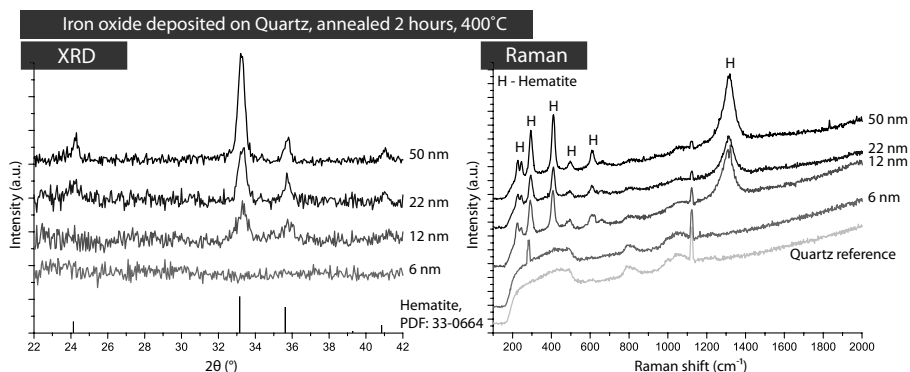


Figure 5.9. XRD, Raman and SEM images of iron oxide deposited on Quartz, annealed at 400°C for 2 hours.

overlapping peaks the presence of maghemite could not be excluded, before the annealing step.

TiO₂ as substrate

From the SEM images in Figure 5.10 it is evident that the iron oxide starts to nucleate as islands and coalesce to an intact film between 8 and 25 nm. This is similar to the previous example and Volmer-Weber growth (Section 3.1.4). At a thickness of 56 nm the iron oxide was in the form of a structured surface instead of a smooth film. This can be due to stresses in the film, a lattice mis-match from the TiO₂ to the iron oxide or a combination of both.

The TiO₂ substrate is used as reference and is included in the bottom of the Raman spectra in Figure 5.10. The most intense peaks from the substrate belong to the underlying Si at 521 cm⁻¹ and around 950 cm⁻¹. There is also a small peak from TiO₂ at 640 cm⁻¹ which belongs to anatase [216]. The other anatase peaks either lie close to the Si peak at 521 cm⁻¹ or are too small to be seen. The laser filter used here extends beyond 150 cm⁻¹, hiding the otherwise strong anatase peak at around 141 cm⁻¹.

From the iron oxide, the peaks start to be visible at a thickness between 25 and 43 nm. Also at 18 nm a small peak is seen at hematite (but also magnetite and maghemite very close) around 300 cm⁻¹. From XRD the iron oxide peaks are visible from a thickness of 18 nm and increase in intensity with the number of applied cycles. At lower thicknesses it is difficult to determine which iron oxide is present but at 55 nm it was mostly hematite, which can be concluded together with the Raman measurements. The peak at around 30° and 42.5° comes from magnetite, and a magnetite peak at 660 cm⁻¹ was also seen in the Raman (strongest in the thickest film). This is believed to be a hematite signal which could be seen when the hematite lacks long range order or has a slightly defect structure [217]. It has also previously been reported that around 30% magnetite is needed to give rise to a signal strong enough to be visible,

when a combination of magnetite and hematite is present in a film [218]. The two other magnetite peaks at 300 and 532 cm^{-1} were absent which strengthen the explanation given here.

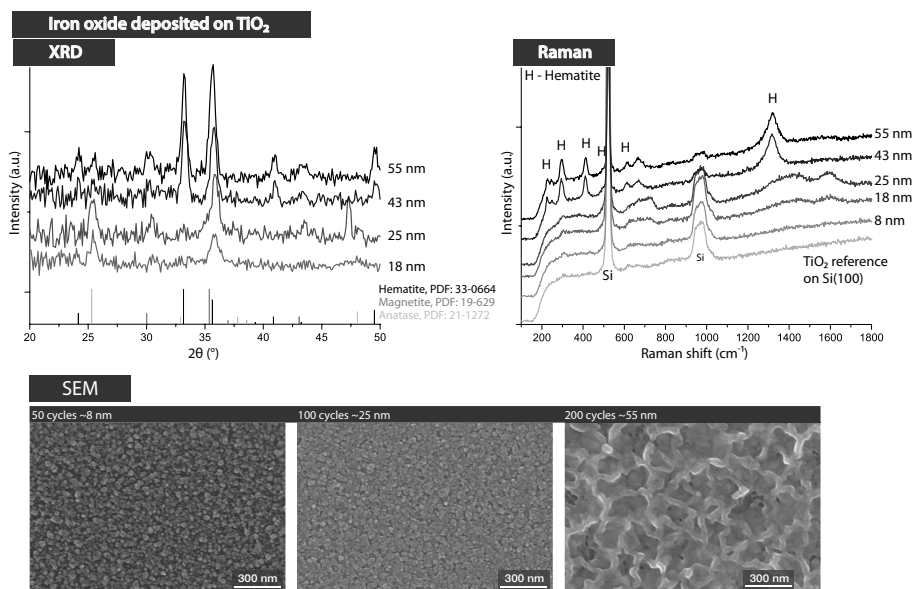


Figure 5.10. XRD, Raman and SEM images of iron oxide deposited on TiO_2 .

A Raman band at 1600 cm^{-1} was visible in the samples with thickness of 18 nm and 25 nm. The origin of this peak has been debated in literature (see Paper IV) but it could imply that maghemite is present in those films. From XRD a shoulder on a slightly lower angle at the peak at around 35° , especially on the sample which is 25 nm. This is in the region where maghemite has a diffraction angle, whereas it could not be excluded that this sample were a phase mixture for the as deposited films. At higher thicknesses the phase was mostly hematite, but since magnetite is less Raman active than hematite (when using 514 nm laser) a phase mixture can be present, since small diffraction peaks from magnetite were visible.

Al_2O_3 as substrate

The SEM micrographs of the deposited film on Al_2O_3 is seen in Figure 5.11. The deposited Al_2O_3 on Si(100) have a surface morphology which makes it difficult to see the actual deposited iron oxide. What can be seen is that the iron oxide have a more three-dimensional morphology. This can especially be seen in the image of a 45 nm thick film. From Raman no signal from any of the iron oxide phases was visible and as amorphous iron oxide is Raman inactive this indicates amorphous films. XRD diffraction peaks were seen at a thickness of 45 nm. In this case it is difficult to draw any certain conclusions.

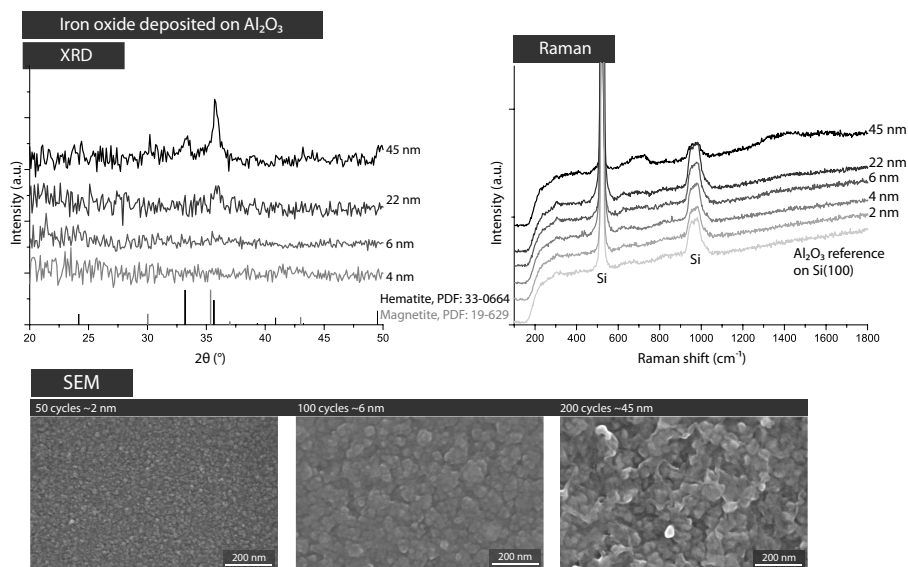


Figure 5.11. XRD, Raman and SEM images of iron oxide deposited on Al_2O_3 .

Since only XRD gives us information the data indicates that the iron oxide was amorphous with small amounts of crystallites in the film. The crystallites could either be hematite, maghemite or magnetite.

Fluorine doped tin oxide (FTO) as substrate

Since the FTO substrate possess a certain surface roughness it is difficult to see any clear differences in the SEM images (Figure 5.12). However, the

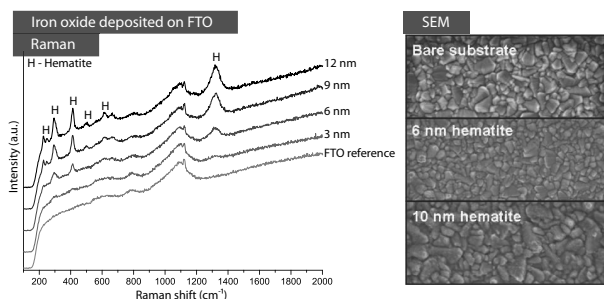


Figure 5.12. XRD, Raman and SEM images of iron oxide deposited on FTO.

iron oxide seems to nucleate in a similar way on all substrates used. This can especially be seen in the image where 10 nm of iron oxide is deposited (Figure 5.12). From the Raman measurement it is clear that the iron oxide peaks can be observed at a lower thickness compared to the other substrates used here. At 6 nm the hematite patterns is clearly visible and also at 3 nm film the peaks can be observed around 300 and 1300 cm^{-1} . The reason for this

early formation of hematite is probably a good lattice match between the FTO and the deposited hematite.

Si(100) as substrate

The analysis of the depositions made on single crystalline silicon is seen in Figure 5.13. From the SEM images it is clear that the iron oxide start to nucleate and form islands up to a thickness of around 10 nm where the islands starts to coalesce into a film. Similar to depositions made on both TiO_2 and Quartz a Volmer-Weber growth is seen. At greater thicknesses the ALD growth was visible as the films seems to grow in one direction. The deposited iron ox-

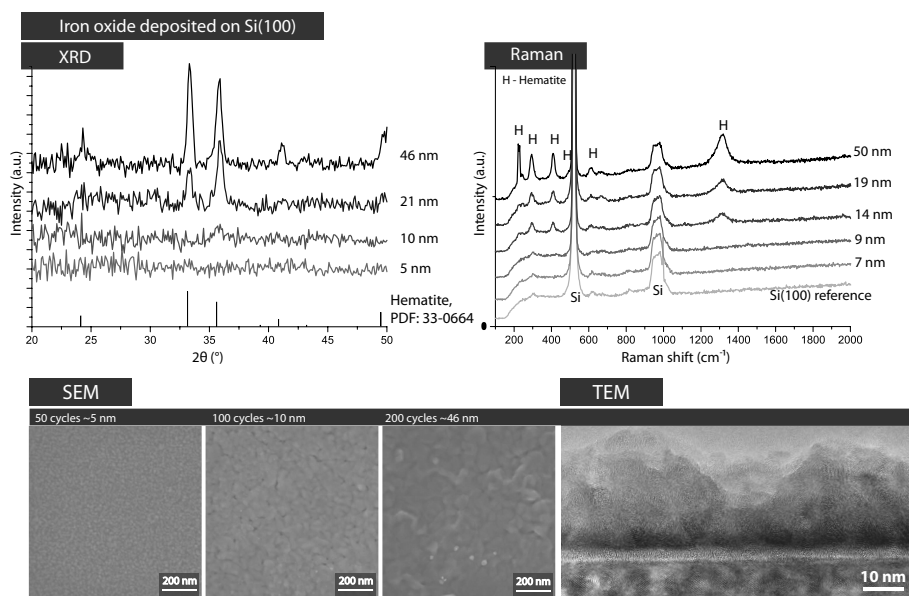


Figure 5.13. XRD, Raman, SEM and TEM images of iron oxide deposited on Si(100). The TEM image has a nominal thickness of 18 nm, determined by XRFS

ide on Si was evaluated with Raman and XRD to investigate the crystallinity. From the Raman measurements it can be concluded that the deposited iron oxide needs around 21 nm before it becomes crystalline, in our case hematite was formed at a thickness interval between 21 nm and 46 nm. This is in good agreement with the XRD measurements.

Growth rate per cycle, GPC, on the different substrates

The growth rate of the iron oxide deposited on Quartz, Si(100), Al_2O_3 and TiO_2 was evaluated regarding thickness vs. number of cycles and growth rate per cycle (GPC), seen in Figure 5.14.

On Si(100) no constant growth with time was observed. The GPC increased with number of cycles. From 0.3 \AA/cycle (after 50 cycles) up to 2.4 \AA/cycle (after 200 cycles). The nucleation part with a lower GPC in beginning is often

observed but the continued increase in GPC is probably due to an increase in surface area of the deposited iron oxide, even though this is not clearly observed in SEM.

A similar behaviour is observed when using Al_2O_3 as substrate. No constant growth rate was observed which changes from 0.3 Å/cycle (after 50 cycles) up to 2.3 Å/cycle (after 200 cycles), as seen in Figure 5.14. However, it was observed that when using Al_2O_3 as substrate the films has a higher surface roughness compared to when Si(100) was used. The growth could therefore have higher surface area, which could be one explanation of the increase in GPC when using Al_2O_3 as substrate.

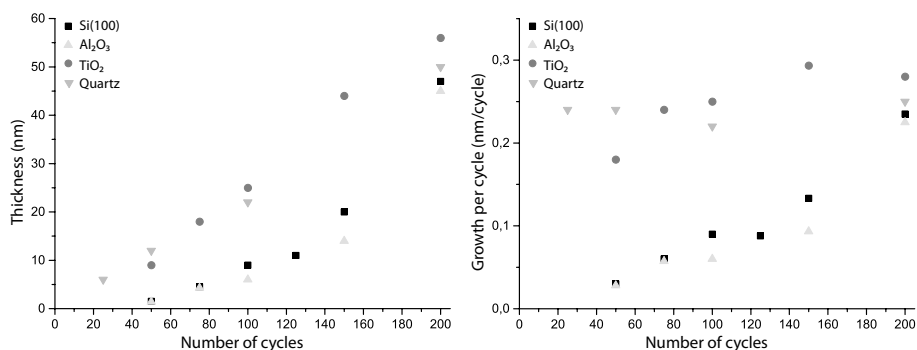


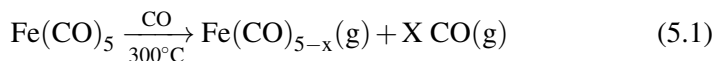
Figure 5.14. Left: Thickness vs. number of cycles for iron oxide on Si(100) (black squares), Al_2O_3 (green triangles), TiO_2 (red circles) and Quartz (blue triangles). Right: GPC vs. number of cycles for the same systems in the left figure.

On TiO_2 the growth rate was fairly constant with a lower GPC in the beginning of the deposition. After the initial nucleation with a GPC of 1.8 Å/cycle (after 50 cycles) the growth rate varies between 2.4 Å/cycle to 2.9 Å/cycle when increasing the number of cycles. From the thickness vs cycles diagram the slope is fairly constant which is a good indication that ALD type of growth is present. On Quartz the growth rate was constant with a variation of 3 Å between the four depositions, from 2.2 Å/cycle (after 100 cycles) and 2.5 Å/cycle (after 200 cycles). The constant slope in the thickness vs. cycles is also observed which is expected when ALD growth is present (Section 3.1.2).

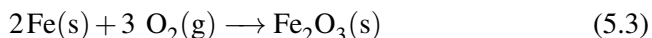
From Figure 5.14 it is evident that the substrate play a crucial role for deposition of iron oxide from ferrocene and O_2 . With Si(100) and Al_2O_3 a lower growth rate is observed compared to TiO_2 and Quartz and no constant GPC or constant slope regarding thickness vs. cycles was observed. This can be compared to both TiO_2 and Quartz where a constant GPC was observed at 400 °C.

5.4 Choise of carrier gas during thin film deposition

For an investigation of the importance of the type of carrier gas used during deposition of iron oxide from $\text{Fe}(\text{CO})_5$ the commonly used N_2 was changed to carbon monoxide (CO). The reason for this change was to inhibit spontaneous decomposition of $\text{Fe}(\text{CO})_5$ (shown in Figure 3.10). The use of CO can therefore be used to suppress decomposition and push the decomposition reaction back, as indicated in Reaction 5.1. Whereas, when using N_2 as carrier gas the situation in Reaction 5.2 may occur. The different carrier gases can therefore control the rate of decomposition¹ of the iron precursor not only on the way to the deposition chamber but also on the sample surface.



When iron is attached to the surface it is most likely to be oxidised by the second precursor, as indicated in Reaction 5.3.



The substrates used were Si(100) and FTO. Ten FTO samples and six Si (100) samples were used with N_2 as carrier gas and six FTO/Si (100) samples were used with CO as carrier gas. They were cleaned prior to the deposition in an ultrasonic bath in a beaker with ethanol for 15 minutes and dried under N_2 -flow. The deposition parameters was set to 0.1–5–3–5 seconds for each cycle at 300 °C and a pressure of 7 mbar. The $\text{Fe}(\text{CO})_5$ used were purchased from Fisher scientific with a purity of 99.5% and the oxygen used was from an in house supplier with a purity of 99.998%.

Because of the decomposition of $\text{Fe}(\text{CO})_5$ the deposition was divided to four separate depositions when using N_2 and two when using CO as carrier gas. The deposition schedule of iron oxide on FTO is summarised in Table 5.2 where the thickness was measured after each deposition. From the table it is evident that when CO was chosen as carrier gas the GPC values increased compared to the N_2 case. This confirms that the reaction was pushed to the left when choosing CO (Reaction 5.1) as carrier gas. The number of cycles used to obtain a similar thickness was therefore 1450 cycles for N_2 and 700 cycles for CO. The increase in growth per cycle was probably a cause from either nucleation in the beginning or from the cauliflower like structure the iron oxide forms on FTO. Because of the different choice of precursor the GPC values could not be compared to those deposited with ferrocene and O_2 . But one

¹A naïve way to picture this is via Le Chatelier's principle: We imagine the system being in a quasi equilibrium with its surroundings, changing in steps on the way towards the substrate – increasing the CO concentration will tend to move the equilibrium towards the side of Reaction 5.1 that opposes the increase in CO concentration, *i.e.* towards left.

conclusion which can be drawn is that the decomposition of the precursor did not lead to a large increase in GPC, rather the opposite, a smaller GPC. This could be an effect of mass transport limitations of material to the substrate or desorption of iron species from the surface. The latter explanation is the most probable because an examination of the substrate showed an excellent step coverage.

Table 5.2. Thicknesses after each deposition of iron oxide using nitrogen (series 1) or carbon monoxide (series 2) as carrier gas on FTO substrates. The numbers 1–10 refers to positions in the reaction chamber, i.e. samples denoted 1 have been in the same position for the two series.

Series:	1. FTO (N ₂)				2. FTO (CO)	
Cycles:	400	800	1200	1450	300	700
Pos.	Thickness [nm]					
1	7.3	18.5	37.8	62.5	9.9	46.2
2	5.6	17.2	34.6	55.8	8.3	44.1
3	6.5	15.1	28.3	45.8	12.1	39.4
4	7.8	17.7	34.0	59.5	13.3	51.3
5	6.9	14.0	35.9	60.9	8.6	44.8
6	6.6	15.9	34.8	57.5	11.7	41.4
7	8.9	17.4	35.0	56.2		
8	9.8	17.4	37.7	62.6		
9	4.5	14.2	32.2	53.2		
10	6.4	13.5	36.3	57.8		

The films were characterised with XRD, Raman, SEM and HAXPES, to determine the phase content and morphology of the surface. From the SEM its difficult to see any clear difference between the films deposited using different carrier gas. There was, however, a clear difference from the uncoated substrate (Figure 5.15 e) and the deposited films, using either CO or N₂ as carrier gas (Figure 5.15 f,g). The films seem to start to nucleate as islands which coalesce. From the images can be concluded that when using N₂ as carrier gas the film consisted of smaller grains than when CO was used.

From the XRD measurements made on FTO (Figure 5.15 a)) it is difficult to draw any clear conclusions. The reason for this is that the strongest peaks from α -Fe₂O₃, γ -Fe₂O₃ and Fe₃O₄ overlap (Figure 4.3); the substrate peaks from FTO is the dominating peaks in the diffractograms. One could only conclude that iron oxide peaks are visible, especially at around 36°. When adding the Raman measurements it is clear that there is a difference between different carrier gases. When N₂ is used (Figure 5.15 c, black line)) the resulting raman peaks can all be attributed to α -Fe₂O₃.

The peak at around 660 cm⁻¹ is close to a Fe₃O₄ peak at 661 cm⁻¹ [93]. This α -Fe₂O₃ peak at 660 cm⁻¹ is often wrongly assigned to another iron oxide polymorph which has a peak in this region [93, 219]. It has for example been assigned to Fe₃O₄ by Sartoretti and coworkers [80], no Fe₃O₄ peaks were

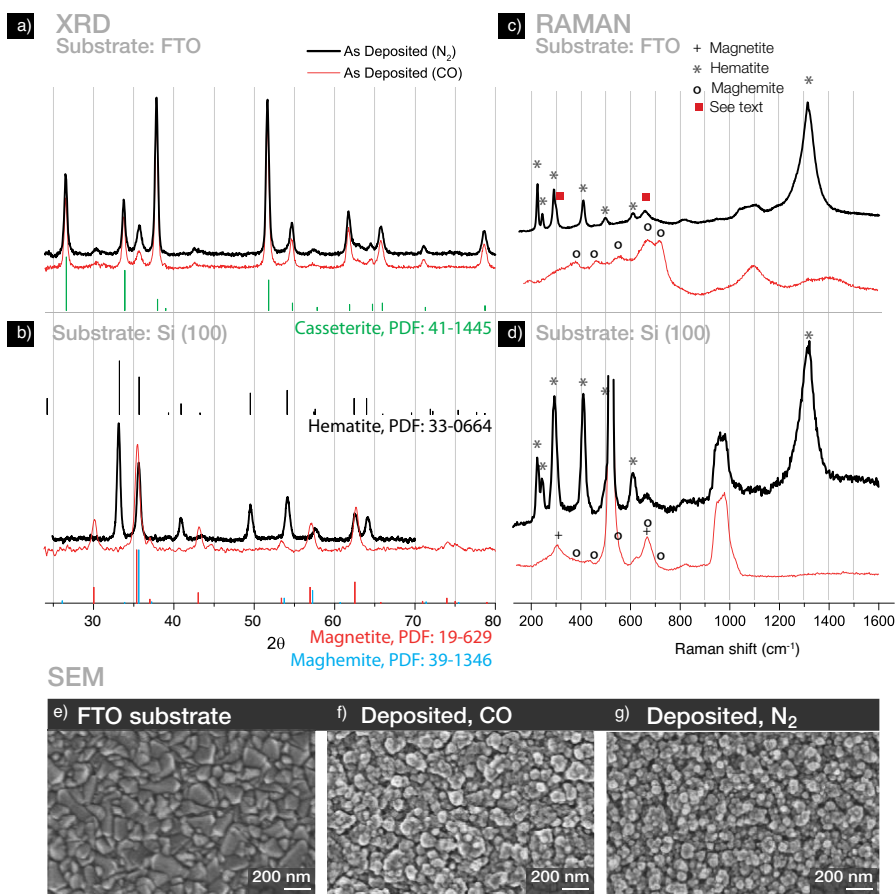


Figure 5.15. (a,b) Diffraction patterns of iron oxide deposited on FTO and Si(100), deposition with N₂ as carrier gas is black and with CO red. (c,d) Raman measurements of the same samples as in a and b. (e) SEM image of the substrate. (f) SEM image of the deposited iron oxide on FTO, with CO as carrier gas. (g) SEM image of iron oxide deposited on FTO using N₂ as carrier gas.

visible in the diffractograms. It has been shown by Beerman *et al.* [220] and Leon *et al.* [221] that the signal at 660 cm⁻¹ belongs to α -Fe₂O₃ and is related to disorder or dislocations in the α -Fe₂O₃ structure. Furthermore it has been shown that more than 30% of magnetite in hematite is needed for the magnetite peak to be visible [218, 219]. This large amount of magnetite in the film should be seen by XRD or in our case by HAXPES, where the line shape of hematite and magnetite are easily separated. The peak has also been suggested by Bersani *et al.* to be related to surface and grain boundary disorder. This is a possible explanation to why the peak is not always present, and in our case this could be the reason why this peak appear since the microstructure of the film varies with deposition conditions.

When CO was used as carrier gas the iron oxide phase was $\gamma\text{-Fe}_2\text{O}_3$, Figure 5.15 c) (red line). The probable cause for this phase shift on the same substrate is that CO reduces the film to maghemite, whereas N_2 most probable does not.

When Si (100) was used as substrate the difference between the two different carrier gases are clearly shown in their XRD-pattern Figure 5.15 b). Similar to what was previously discussed, N_2 gave rise to an $\alpha\text{-Fe}_2\text{O}_3$ pattern whereas when CO is used, $\gamma\text{-Fe}_2\text{O}_3$ or Fe_3O_4 was observed. From Raman the as deposited film using N_2 as the carrier gas shows a hematite pattern with two additional Si peaks (at 521 cm^{-1} and the broad peak at 975 cm^{-1} Figure 5.15 d). The as deposited film using CO as carrier gas did not show the maghemite pattern which it did when FTO were used as substrate (Figure 5.15 c). Instead a Magnetite pattern was observed with addition of the Si peaks from the substrate. It is believed that the CO have the same impact here, continuously reducing the film during the deposition.

The reason why the film becomes maghemite when using FTO as substrate and magnetite when using Si(100) as substrate can be explained by different lattice matching between the substrates and the deposited film.

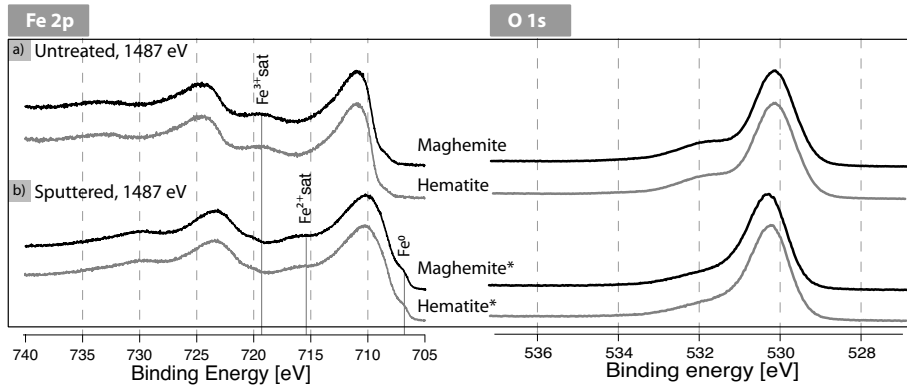


Figure 5.16. a) X-ray photoelectron spectroscopy of the Fe 2p and O 1s region on the samples deposited with either N_2 and CO as carrier gas. The satellites of Fe^{2+} and Fe^{3+} are marked with vertical lines in the left Fe 2p image. b) XPS spectra of Fe 2p and O 1s region after sputtering.

XPS (Al $K\alpha$, $\hbar\omega = 1487\text{ eV}$) were used to compare the two different films. The maghemite and hematite have similar chemical shifts and line shapes, compared with each other. This is because they almost have identical orientation of the cations in the structure (hematite - hexagonal, maghemite - cubic). In hematite the cations (Fe^{3+}) are octahedrally coordinated to the anions (O^{2-}), whereas in maghemite 75% of the cations are octahedrally coordinated and 25% are tetrahedrally coordinated [49]. To balance the over all charge, vacancies in the cation positions are present in maghemite. There is however a small shift of 0.2 eV for the $\text{Fe } 2p_{3/2}$ peak, 710.8 eV for hematite and 711.0

eV for maghemite found in literature [205]. The Fe^{3+} satellite is located at 719.3 eV in both the maghemite and hematite [205].

From the XPS measurements recorded for the two different carrier gases no difference could be seen, Figure 5.16 a). This was valid in both the Fe 2p and O 1s case where the line shape for the regions was identical. The small shift for the Fe 2p_{3/2} peak was not observed, but the line shape for both hematite and maghemite correspond well with the line shape found in literature [205]. The shoulder on the higher binding energy side of the O 1s is due to hydroxy-groups or carbon bound to the surface [222, 223]. When sputtering the samples it is evident that the sputtering damage the sample, see below.

The as deposited film using CO as carrier gas was also measured using HAXPES, Figure 5.17. The investigated regions were Fe 2p and O 1s with three different kinetic energies for depth profile without sputtering. In Figure 5.17 a) reference spectra of Fe₂O₃ and FeO are included. When comparing the as deposited film with the reference spectra it is clear that the film has the line shape of Fe₂O₃. The Fe^{3+} satellite located at 719.2 eV is present in both the as deposited film as well as in the Fe₂O₃ reference spectra. The position of the satellite is in good agreement of previously reported data for hematite or maghemite by Grosvenor *et al.* [205].

In Figure 5.17 b) the as deposited film is measured with 2005 eV, 3000 eV and 6015 eV to see if there is any difference of the iron oxide at different depths. No significant change in positions in the Fe 2p area were observed which is a good indication that the oxidation states are uniform in the film. In

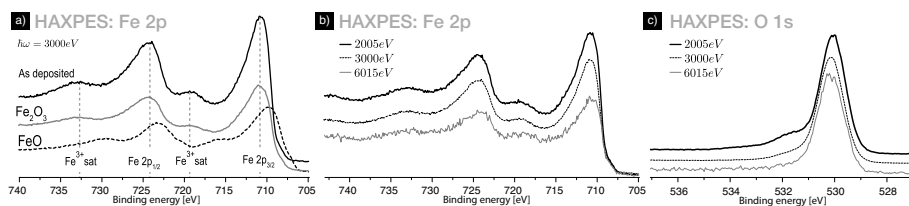


Figure 5.17. (a) HAXPES measurements of the as deposited film using CO as carrier gas. Reference spectra of FeO and Fe₂O₃ are included in the bottom of the figure. (b) Same film as in (a) but with 3 different measured energies. (c) The O 1s peak of the as deposited film using CO as carrier gas, measured at three different energies. The ordinate axis' units are arbitrary.

Figure 5.17 c) the O 1s core level is examined by HAXPES, at the same energy used in Figure 5.17 b). The line shape over the O 1s core level using 2005 eV consist of two components, whereas at higher energies the part at a the higher binding energy side becomes smaller. This is often seen and the component on the higher binding energy side comes from the surface of the film. This could be absorbed molecules on the surface or hydroxyl groups attached, the latter have been proposed in a similar system by others [222, 223].

Sputtering of the films were also tested with the lowest possible energy available by the instrument. The sputtering were performed on one maghemite film and one hematite film (one from each carrier gas used) on the in house XPS with Al- $K\alpha$ radiation. The settings were set to 8 minutes using 200 V Ar^+ ions. Eight minutes were chosen since this time was required to remove carbon on the surface. This was checked with the C 1s core level peak.

The result of the sputtering were compared with the HAXPES made on the sample where CO was used as carrier gas. From the sputtering the most prominent difference were that the Fe^{3+} satellite at 719.3 eV were missing, and instead the Fe^{2+} satellite at 715.4 eV became visible (Figure 5.16). The positions of both the spin orbit components of Fe 2p were also shifted to lower binding energy. The O 1s peak were also shifted to a slightly higher binding energy and the shoulder on the higher binding energy side were smaller compared with the sample before sputtering.

As mentioned, the O 1s peak is difficult to use for determination of which iron oxide phase is present. The binding energy range from 529.9 eV (γ - Fe_2O_3 , α - $FeOOH$, γ - $FeOOH$, FeO), 530.0 eV (α - Fe_2O_3) to 530.2 eV (Fe_3O_4) includes all the iron oxides. But it is still a good indication if any hydroxyl-groups are attached to the surface, since hydroxyl groups have binding energies separated from the iron oxides [222].

With the knowledge from the HAXPES measurements, the depth profile (visible in Figure 5.20) did not change up to 25 nm (using 6015 eV in photon energy). Using Al $K\alpha$ radiation the information depth was around 8 nm, as seen in Table 4.1. The XPS setup used an outgoing angle of 45° from the sample which makes the information depth even smaller, around 6 nm (Section 4.5 and Figure 4.7).

The sputtering of the surface changed the iron oxide from hematite and maghemite to FeO after the sputtering. Metallic iron were also detected on the lower binding energy side of Fe $2p_{3/2}$ component. The effect of sputter damage is well known [194, 224–227], and even when the lowest sputtering energy was used, some sputter damage were present.

5.5 Diffusion of Sn, Si and F in iron oxide upon annealing

The diffusion experiments were performed on the samples described in section 5.4. The samples varied in thickness between 40 to 60 nm. This variation should, however, not influence the conclusions regarding the diffusion. The annealing schedule are summarised in table 5.3, which also includes thicknesses and type of carrier gas used during deposition. The annealing took place at the Ångström laboratory except for the sample III and VI which were annealed in the HAXPES chamber at Bessy, prior to the measurement. Due to the different annealing chambers, the annealing times were different because

Table 5.3. Summary of the annealing step performed on 9 samples. The samples annealed in the analysing chamber at Bessy are marked with an asterisk after their sample number.

Sample	Carrier gas	Thickness	Temperature	Vacuum/Air
I (RT)	CO	39.4/44.1 nm	RT (300°C)	-
II	N ₂	54.5 nm	RT (300°C)	-
III*	CO	44.1 nm	550°C	Vacuum
IV	N ₂	55.8 nm	550°C	Vacuum
V	N ₂	53.2 nm	550°C	Air
VI*	N ₂	45.8 nm	650°C	Vacuum
VII	N ₂	59.5 nm	650°C	Air
VIII	N ₂	57.8 nm	700°C	Vacuum
IX	N ₂	56.9 nm	700°C	Air
X	CO	44.8 nm	800°C	Air
XI	CO	41.4 nm	800°C	Vacuum

of cooling times. However, the time for annealing at the specific temperature was still believed to be in the same region.

As reference for the diffusion the thinnest sample (39.4 nm) was used as the room temperature (RT) sample. This to ensure that the film had no trace of either Sn, Si or F during the HAXPES measurements, *i.e.* to ensure that the probing depth was smaller than the film thickness. Neither Sn, Si or F could be observed for this sample in the HAXPES measurements which is seen in Figure 5.20, 5.21 and 5.22, where the black lines are from the measured RT sample.

The annealed film were also analysed using XRF, XRD, HAXPES, SEM and Raman. XRF for thickness measurement, SEM to visualise the surface and XRD/Raman for phase information.

The SEM images are shown in Figure 5.18 where the FTO substrate also are included. From the SEM images it is evident that there is a difference in the films annealed in air and in vacuum. The samples annealed in air (Figure 5.18 e), f) and g) had a coarser surface structure because of grain growth and grain coalescence, especially on the samples annealed at 700 °C and 800 °C. The opposite effect happens for the samples annealed in vacuum (Figure 5.18 d) and h), where no grain growth occurred and the surface structure consisted of smaller grains. This is especially seen when comparing the RT samples (Figure 5.18 b) and c) with the ones annealed in either air or vacuum. A similar effect has previously been reported by Wang *et al.* [228], where annealing in air above 600 °C leads to coalescence into larger grains and that annealing in argon suppress grain growth, leading to smaller grains. In our case it is believed that annealing in vacuum acts similarly to annealing in argon.

XRD were performed on a selection of the films shown in Figure 5.19 a) and b). In the figure reference data from cassiterite (SnO₂), hematite (α -Fe₂O₃),

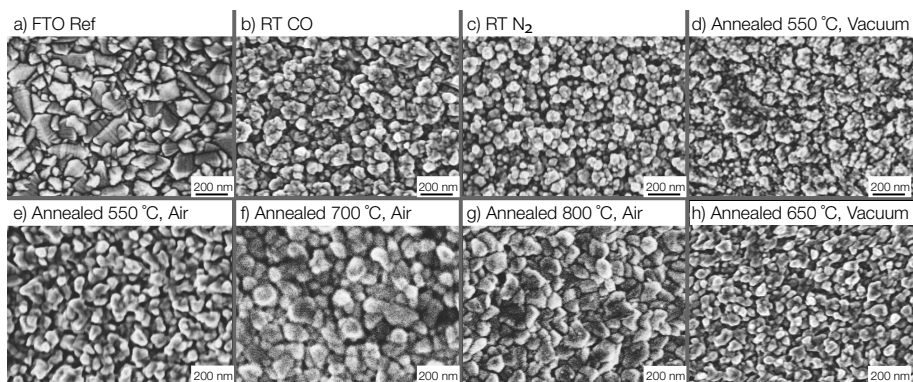


Figure 5.18. SEM images from an FTO reference, RT and annealed samples (air and vacuum). The magnification is alike on all the images for an easier comparison. The RT samples with either CO or N₂ are the same samples used in Section 5.4

maghemite ($\gamma\text{-Fe}_2\text{O}_3$) and magnetite (Fe_3O_4) are included, and visualised with vertical lines in Figure 5.19 a) and b).

From the as deposited sample the iron oxide phase is difficult to determine using only XRD. And as previously discussed the strongest diffraction angles are almost identical for $\alpha\text{-Fe}_2\text{O}_3$, $\gamma\text{-Fe}_2\text{O}_3$ and Fe_3O_4 . However, upon annealing more peaks from the deposited iron oxide can be observed, indicating a more crystalline structure or larger crystallites. Comparing the iron oxide annealed in air/vacuum (Figure 5.19) different diffraction angles are observed. For the films annealed in air the diffraction pattern is in good agreement with hematite and when annealed in vacuum the diffraction pattern is a good match with magnetite (and maghemite).

The Raman measurement corroborates the results from XRD with one exception. The film annealed in vacuum at 650 °C (Figure 5.19 d) show shifts which belongs to both hematite and magnetite, hematite shift is marked by asterisk (*) and magnetite by plusses (+). Maghemite's Raman shift are also included with circles on the red dotted recorded spectrum in 5.19 d). As previously discussed in Section 5.4 hematite is much more Raman active than magnetite [217–219]. If a small amount of hematite is observed with large amount of magnetite this must imply that the amount of hematite indeed is very small.

From the samples annealed in air, Figure 5.19 c), the hematite shifts is seen already from the as deposited and for all samples up to 800 °C. The only peak which changed in intensity compared to the others are the shift at 660 cm^{-1} . As previously discussed this shift is absent in a perfect hematite crystal. But when the hematite has a disorder or possible dislocations this shift is observed [220, 221]. The intensity of this Raman shift also increased with annealing temperature, compared to the other hematite peaks. This is probably caused

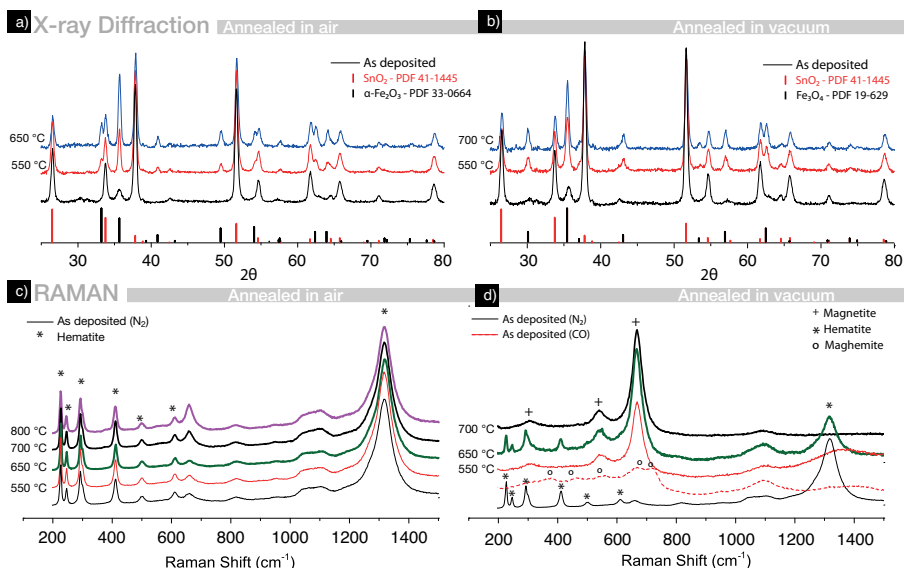


Figure 5.19. XRD and Raman measurements on films annealed in vacuum a), b). XRD and Raman measurements on films annealed in air c), d). The dashed and the thin lines in the Raman spectra indicate the RT samples where CO and N_2 were used as carrier gases during the growth procedure.

by diffusion of elements from the substrate, leading to more disorder in the hematite lattice.

To examine diffusion from the substrate the Fe $2p$, Sn $3d$, Si $1s$, O $1s$ and F $1s$ core levels were measured using HAXPES. The samples chosen were those annealed at 550 °C and 650 °C in vacuum, and those at temperatures of 550 °C, 700 °C and 800 °C annealed in air. Three different photon energies were used to investigate the composition throughout the film. All samples were measured using a photo energy of 3000 eV. The analysing depth in iron oxide discussed here are summarised in Table 4.1. The mean free path (λ) for each photon energy and iron oxide were calculated from the inelastic mean free path from the TPP2M formula by Tanuma *et al.* [169].

The Fe $2p$ core level region is shown in Figure 5.20 measured with 2005 eV, 3000 eV and 6015 eV. The measured reference spectra of FeO, Fe_2O_3 , Sn(foil), SnO, SnO_2 and FTO are included. Sn references are included since the Sn $3p_{3/2}$ lies at a binding energy in-between the two Fe $2p$ spin orbit components.

From the as deposited film there is no large differences between the samples when the annealing take place in air (Figure 5.20 b). The as deposited films examined during the HAXPES measurements was the one using CO as carrier gas, giving a maghemite film as discussed previously in Section 5.4. There is, however, a small distinct difference of the Fe $2p_{3/2}$ region in transition from a smooth line shape of the as deposited sample into a distinct peak with a

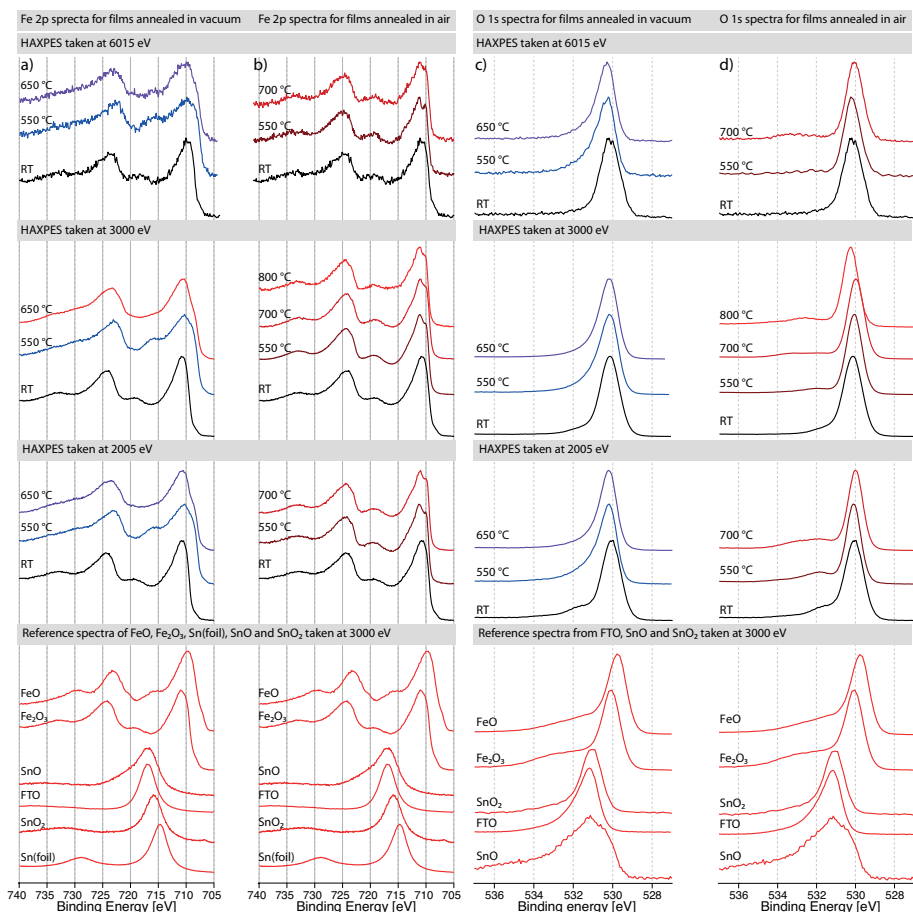


Figure 5.20. Fe 2*p* core level spectra of samples annealed in vacuum (a) and in air (b), O 1*s* core level spectra for samples annealed in vacuum (c) and in air (d). Reference spectra of the Fe 2*p* and O 1*s* core level regions in hematite, FeO, Sn, SnO, SnO₂ and FTO are also included. The ordinate axis' units are arbitrary.

shoulder on the lower binding energy side for the annealed samples. This line shape over the Fe 2*p*_{3/2} region is well in line with previously reported data for hematite [208].

Each spin orbit component in the Fe 2*p* spectra for the samples annealed in air and the as deposited film (Figure 5.20 b) have an accompanying Fe³⁺ satellite, located at 719 eV. In between the main spin-orbit components there is a, more or less a shallow valley, especially in between the Fe 2*p*_{3/2} and the Fe³⁺ satellite. Going from an annealing temperature of 700 °C to 800 °C, this valley flattens visibly in the spectra. This is especially seen using 3000 eV where the difference between the valley (around 716 eV) and the Fe³⁺ satellite disappear. This effect could be an indication of a Fe²⁺ satellite from a

magnetite or wustite phase, seen in the reference spectra from FeO (displayed in the bottom figure). No indications from these phases are, however, found in the Raman measurements or in the XRD patterns.

From the three different photon energies used, no clear difference could be observed. This is a good indication that the film has the same chemical states throughout the film, at least when looking at the Fe 2*p* core level.

For the films annealed in vacuum a clear difference from the annealed in air/as deposited can be seen (Figure 5.20 a)). The satellite structure between the two Fe 2*p* spin orbit components almost disappear for the sample annealed at 650 °C in vacuum. This is a typical line shape for magnetite where the mixed valance between Fe²⁺ and Fe³⁺ flattens out the satellite structure between the two spin orbit components [205, 229]. Magnetite has a stoichiometric ratio of Fe²⁺ and Fe³⁺ of 1:2 which results in the observed intensity distribution [229]. From the Raman measurement this sample showed that only a small amount of hematite was present in the film. This is not observed in the HAXPES from either of the photo energies used. One explanation to this is that the hematite phase is present in the film below the information depth (25 nm (Table 4.1)) when 6015 eV is used.

The film annealed at 550 °C has a similar line shape as FeO. This is not seen from either XRD or Raman making it more probable that this intensity comes from diffused Sn into the hematite. The Fe 2*p* positions and the overall line shape resembles that of magnetite. No difference between the different photo energies were visible for the samples annealed in vacuum, for the Fe 2*p* positions.

From the O 1*s* spectra recorded at 2005, 3000 and 6015 eV no large differences between the three different photon energies were observed for either annealing in vacuum or in air as can be seen in Figure 5.20 c) and d). There is however a clear shift between the films annealed in air or in vacuum. Between magnetite and hematite a shift of the O 1*s* peak is expected to be 0.2 eV. The hematite peak is well in line with the Fe₂O₃ reference, visible in the bottom of Figure 5.20.

For magnetite films (Figure 5.20 c)) the oxygen peak is located at 530.2 eV for both the annealing temperatures used. In the films annealed in air the position of the oxygen peak is at 530.1 eV for the film annealed at 550°C, 530.0 eV for the film annealed at 700 °C and 530.3 eV for the film annealed at 800 °C. The position of the O 1*s* signal in magnetite and hematite is in good agreement with Grosvenor *et al.* [205] with one exception. The 800 °C annealed in air is shifted to a higher binding energy. From Raman no magnetite or maghemite can be seen and the line shape of the Fe 2*p* region resembles that of hematite. The shift is instead believed to be a result from the diffusion of Sn from the substrate as discussed later. The shoulder on the higher binding energy side is different for the different annealing environments. A part of this is a contribution from hydroxy groups on the surface, this is clearly visible from the RT sample where the shoulder decrease with higher photon energies

(Figure 5.20 c) and d)). This is also believed to be a cause from the diffusion of species from the substrate. Beneath the measurements of the annealed films, reference spectra of SnO₂, SnO and FTO are shown (Figure 5.20 c) and d)). The tin oxides have binding energies on the higher binding energy side of iron oxides, as can be seen in Figure 5.20 c) and d). The shoulder is therefore believed to be a cause from either Sn or Si diffusion into the hematite.

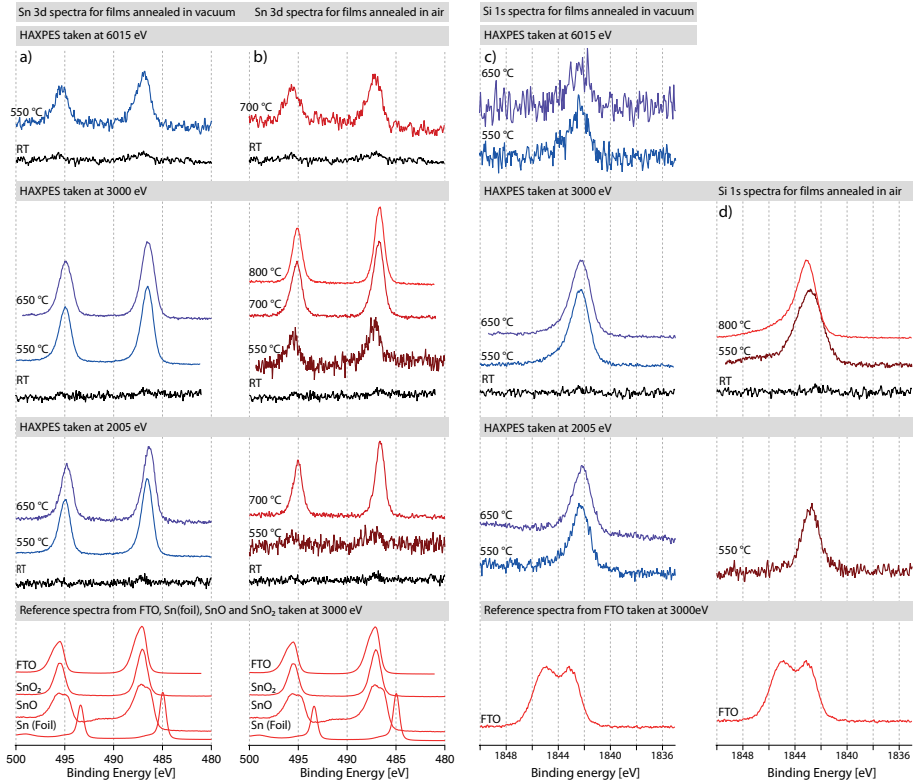


Figure 5.21. Sn 3d core level spectra of samples annealed in vacuum a), and in air b). Si 1s core level spectra of samples annealed in vacuum c), and in air d). Reference spectra of the Sn 3d region for FTO, SnO₂, SnO and Sn are included beneath the measured samples Sn 3d region. For Si 1s, FTO is included as reference. The ordinate axis' units are arbitrary, the spectra has been scaled for fit in the figure.

Regarding the Sn 3d region the as deposited samples show no signal from Sn. Shown in Figure 5.21 a) and b) where the black lines refers to the as deposited sample, which was the thinnest sample in the series. Annealing in both vacuum and air gave rise to a signal from Sn. The different annealing temperatures exhibit a variation in the signal strength. The sample annealed in 550 °C in air showed a smaller signal compared to the samples annealed at higher temperatures. This is evident when comparing the signal to noise ratio between the 550 °C with the 700 °C and 800 °C.

The Sn 3*d* features from both the samples annealed in air and vacuum has a symmetric peak shape and the chemical shift corresponds to SnO_x , where *x* is somewhere in between 1 and 2. This could be seen comparing the annealed samples with the reference of SnO₂ and SnO which are included at the bottom of Figure 5.21 a) and b).

The positions of the Sn 3*d*_{3/2} at 495.1 eV and Sn 3*d*_{5/2} at 486.7 eV (samples annealed in air) is well in line with previously reported data [90, 230]. There is, however, a small shift present between the two different annealing environments. The shift follows the same trend with temperature for the films annealed in vacuum and in air. The shift for the Sn 3*d* core level for films annealed in air was 0.2 eV. As the shifts are independent of the annealing environment, it likely stems from diffusion of Sn from the substrate into the hematite film, and could be a sign that the oxide of the formed Sn is oxygen deficient. The resulting tin oxidation state should thus be described as SnO_{2-x}, where *x* shifts with the amount of diffused Sn and oxygen available.

The amount of Sn, inferred from the peak areas of *e.g.* Fe 2*p* and Sn 3*d* for the same sample is also different throughout the sample. The sample heated at 650 °C and deposited with nitrogen as carrier gas contains the least diffused amount. The ratio between the Sn 3*d* and the O 1*s* peak's area is 3 % for this sample, whereas it is 10% for the sample heated to 550 °C and deposited with CO as carrier gas. Although the heating times differ by ten minutes we believe that the presence of a mixture of iron oxide phases is responsible for the slower diffusion.

When 6015 eV photons are used the information depth is 25 nm compared to 14 nm using 3000 eV. The line shape of the samples measured at 6015 eV is a little bit broader than the ones measured with either 2005 eV or 3000 eV. The peak positions are also shifted to higher binding energies. This suggest that the chemical states are different in the film. The shift towards higher binding energies indicate that the Sn compound formed is SnO_{2-x}, where *x* either is 0 or very close to 0. This can be explained by a gradient in the Sn diffusion, which would be expected. The amount of tin in the film decrease from the interface up to the surface. The interface is therefore believed to be not sharp because of the diffusion of Sn which clearly takes place during annealing of the iron oxide.

The Sn diffusion is more clearly visible in the extended Fe 2*p* region from 700 to 800 eV as shown in Figure 5.22. This region also includes both the spin orbit components of Sn 3*p*. FTO is also included in the figure as reference for both the Sn 3*p*_{1/2} and Sn 3*p*_{3/2}. From the figure its clear that Sn diffusion take place in both the measured samples. It also shows the influence of the Sn 3*p*_{3/2} region which appear in between the two Fe 2*p* components. The diffusion of Sn has a strong influence for especially the sample annealed at 550 °C in vacuum where the shoulder on the higher binding energy side of Fe 2*p*_{3/2} is a tin oxide, and not FeO, as discussed previously. This sample also shows the strongest Sn intensity. In the 800 °C annealed in air sample the

diffusion of Sn is shown from the "absent" valley between the Fe^{3+} and the $\text{Fe } 2p_{3/2}$ components (Figure 5.20 b)).

The diffusion of Si follow the same trend as the diffusion of Sn into the iron oxide. From no Si signal visible in the RT sample, and that the diffusion is clearly visible from 550 °C in both the annealing environments as shown in Figure 5.21. The FTO substrate is used as reference for the Si 1s core level. The reference were measured using 3000 eV which gives us the information that the FTO film on top of quartz is at least below 12.6 nm (Calculated with TPP2M formula [169], λ around 4.2 nm), otherwise no signal from the Si would have been observed. In the case of the samples treated in air, more oxidation states in the film were observed, as deduced from the asymmetry of the Si 1s line shape. However, except for the difference in line shape a shift of the Si 1s core level between the annealing environments are also visible.

The shift was 0.9 eV where the sample annealed in air at 800 °C was located at 1843.0 eV, and the samples annealed in vacuum at 550 °C and 650 °C had peaks located at 1842.1 eV. The Si 1s core level for SiO_2 is located at 1844.7 eV [231] and Si^0 at 1839.4 eV [232].

The other oxidation states: Si^{3+} , Si^{2+} , and Si^+ are located in between those extremes. The position of the Si^{4+} in SiO_2 can vary in binding energy depending on film thickness [232]. When compared to the Si^0 : this variation is shown to be up to 0.8 eV from thicknesses ranging from 0.37 nm (1843.8 eV) to 2.87 nm (1844.6 eV), and could be one reason for the line shape of Si 1s on the higher binding energy side [232].

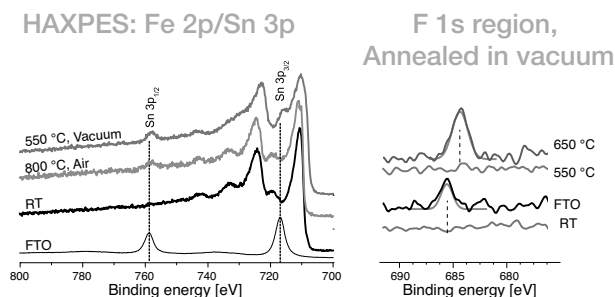


Figure 5.22. Left) Extended Fe 2p core level region from 700 eV to 800 eV, including both the spin orbit components of Sn 3p. Right) F 1s core level for samples annealed in vacuum, FTO reference and the RT sample.

For Si the distribution of oxidation states was between 0 and +4. In the case of the samples treated in air, more oxidation states in the film were observed, as deduced from the asymmetry in the Si 1s line shape. For the samples annealed in vacuum the line shape was more narrow which indicates less oxidation states, compared to the in air annealed samples.

Except for both the Sn and Si as discussed in this section, fluorine was detected in the annealed sample in vacuum at 650 °C. The F 1s signal was

only observed in this sample, which can be seen in Figure 5.22. The shift from the FTO shows that the fluorine is not from the FTO substrate but from another environment, *i.e.* the iron oxide film. Because of the diffusion into iron oxide the binding energy of the F 1s decreases.

A subset of the films were analysed with UV-Vis, shown in Figure 5.23 a). The hematite films, the ones annealed in air and the as deposited film show similar absorption behaviour. Whereas the magnetite films, those annealed in vacuum show a absorption behaviour stretching beyond the hematite films, as expected from the lower band gap in magnetite. The photocatalytic performance where measured in a three electrode setup shown in Figure 5.23 c). This measurement was performed to see what influence the annealing had on the water splitting properties. The films annealed in vacuum showed no significant photo oxidation activity (Figure 5.23 b), which is not surprising, since they contained magnetite in the films. The as deposited film was essentially not photoactive. The films annealed in air were equally beneficial, regarding the measured photocurrent. These films contained the hematite phase, which also the as deposited film did. The difference between the film are the diffusion of Si and Sn, which is present in the annealed films. This show that annealing is a necessary step to obtain any photocurrent from these thin hematite films.

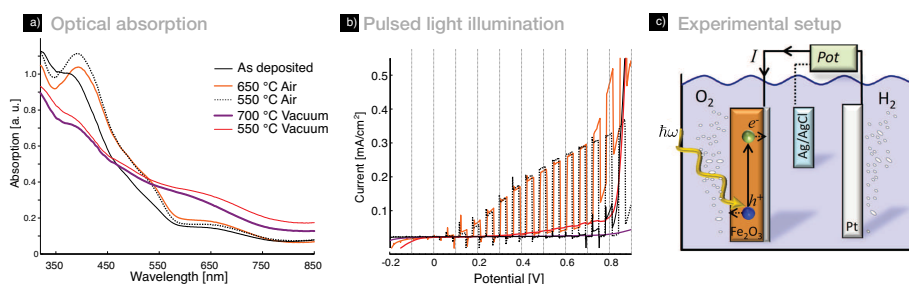


Figure 5.23. a) Optical absorption for films annealed in air, vacuum and as deposited. b) Photoactivity of water oxidation under pulsed light. c) The three electrode setup used.

5.6 Optical quantum confinement in low dimensional hematite

Because of the limitation in the charge carrier transport in hematite, the material needs to be in the form of low dimensional particles or thin films to work in several applications, *i.e.* photoelectrochemical cells for solar hydrogen production. When hematite are in this size region (nm) the optical properties are effected, introducing additional complications for efficient design of a device.

To investigate this phenomena a thickness series with a total of 35 samples were deposited, ranging from 2 nm up to 70 nm, the thicknesses are sum-

marised in the supplementary information in Paper I. The iron oxide were deposited on FTO substrates with different number of ALD cycles (50 to 600 cycles) to obtain the different thicknesses. Since the decomposition of the precursor occurred, each deposition gave similar, but not the exactly same thickness. A total of seven depositions were therefore necessary for the thickness series. This behaviour is more thoroughly described in Section 5.4.

Carbon monoxide were used as carrier gas to deposit thicker films (Section 5.4). To obtain hematite films, a post annealing step at 500 °C for 8 hours in air were performed on all the samples. This was necessary since the deposited film using CO as carrier gas consist of maghemite (Section 5.4). After the annealing step, the films were characterised using Raman and XRD, shown in Figure 5.24.

From the XRD data it is evident that the desired phase transition from maghemite to hematite occurs. When Si(100) was used as substrate this was straightforward (Paper I) but when FTO were used the peaks from hematite were difficult to detect, due to the signal from the substrate. As the θ -2 θ geometry were used for the FTO films the substrate became more visible, comparing with GIXRD which was used for the films deposited on Si(100) (found in Paper I). However, the observed peaks were in agreement with hematite reflexes, especially at 33°, where no overlap from maghemite is present.

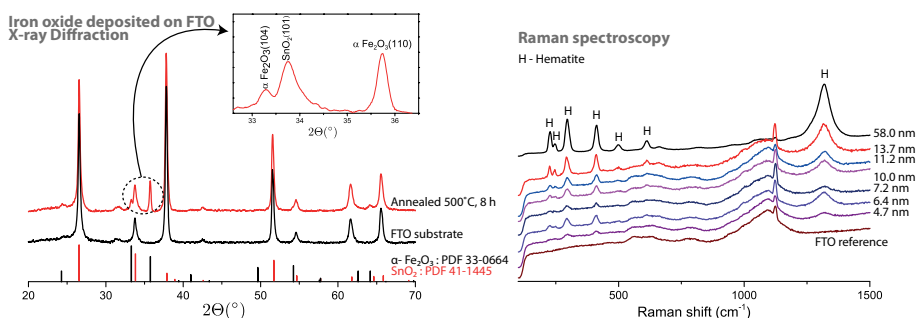


Figure 5.24. Left) XRD on annealed iron oxide (red) and the FTO substrate (black). The inset is the region where the hematite reflexes are visible. Right) Raman spectra from a selective number of films in the thickness series. The FTO substrate is included in the bottom of the figure. The ordinate axis' units are arbitrary.

Raman measurements were carried out on a selective number of the films and hematite was observed in all the samples. At a lower thickness the signal from hematite were smaller and almost indiscernible from the background. Compared with similar films annealed at higher temperature (described in section 5.4) the shift at 660 cm^{-1} was missing or very small. The annealing were necessary when using $\text{Fe}(\text{CO})_5$ and O_2 as precursors, while if ferrocene would be used this step would probably not be necessary.

To be able to compare the relative intensities regarding the film thickness, the background was removed and all the spectra were normalised to the 412

cm^{-1} shift, shown in Paper I. The Raman data show no anisotropic phonon confinement in the films thicker than 5 nm, as no relative peak intensities, broadening or shift could be detected. However, the data show a general suppression of all phonon modes with a vaguely stronger suppression of the shift at 297 cm^{-1} . This general suppression thus seem to be an effect of isotropic phonon confinement.

XPS were performed to investigate the carbon content in the films (Supplementary information in Paper 1). A sputter profile showed that carbon was detected on the surface, but in the film the signal decreased down to the detection limit of the instrument, which is below 1%. The origin of the carbon on the surface is due to that the sample had been exposed to air prior the measurement. However, this conclude that no ligands from the $\text{Fe}(\text{CO})_5$ were left in the film. Either they reacted with the O_2 pulse, or decomposed, and were flushed away by the purge pulse.

The SEM images (Figure 5.25), show that films starts to nucleate as islands. The islands coalesce to a film at a thickness between 6 nm and 11 nm. From the SEM images it can be seen that the deposited iron oxide films are nano structured, as described more in detail in Section 5.5.

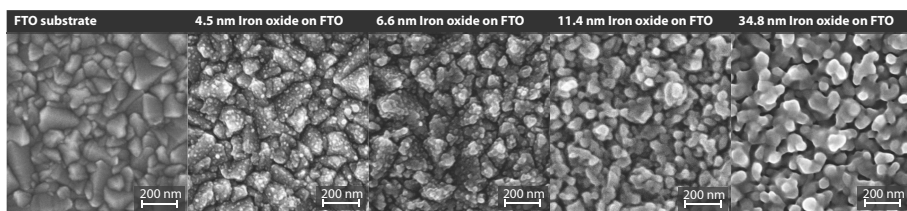


Figure 5.25. SEM images of four different thicknesses of the deposited iron oxide. The FTO substrate is included for easier interpretation.

The UV-Vis measurement were performed on all the deposited films (settings described in Section 4.7). With UV-Vis, several features could be extracted. The optical measurements are shown in Figure 5.26 b,c). For an easier interpretation, all the curves in the figure are normalised, using the peak around 380 nm. From the figures it can be seen that both the absorption maxima, and the band gaps, are shifted to higher energies for the thinner films. There is also a dependence of the relative absorption in the visible, between 450 and 650 nm – here the behaviour of the shoulder at longer wavelengths is different depending on the thickness.

The maximum of the absorption change to longer wavelength (red shift). The red shift was in the order of 200 meV, when going from thicknesses 4 to 20 nm. After 20 nm, the absorption maximum becomes independent on the thickness of hematite, illustrated in Figure 5.27 c). A shift of the absorption edge is an indication of quantum confinement [233]. The blue shift of the absorption maximum for thinner films is an indication of a change in the density

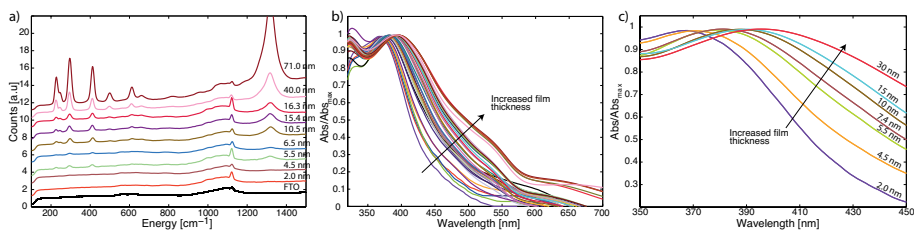


Figure 5.26. a) Raman measurements for a subset of the hematite films. b) Optical measurements of all the films, the data are normalised with respect to the absorption maximum. c) Optical measurements of a subset of the film for an easier view how the absorption maximum changes with thickness of the film.

of states in the valence and/or conduction bands (as described in the model in Section 2.1), or in the orbital overlap for thin hematite films.

As previously mentioned (Section 2.2.1), hematite is an indirect semiconductor. The indirect band gap vary between 1.9 to 2.2 eV [48, 234] depending on the synthesis route used. All indirect semiconductors also possess a direct transition located at higher energies. Quantum confinement, arising from film thickness, could potentially affect the positions of both indirect and direct band gaps, as well the probability for these transitions. Both transitions can be sorted out from the experimental optical measurements, from which also a quantitative measure of the thickness dependence can be achieved.

For the indirect band gap, a plot of the square root of the absorption versus photon energy can be made. With an extrapolation of the linear region of the data down to zero absorption gives the indirect band gap. Such a plot is shown in Figure 5.27 b). The linear region is between 2.17 to 2.27 eV for films from 5 nm. For thinner films, below 5 nm, this linear region was less distinct and for even thinner films this region was absent. This makes the model not reliable for the thinner films. Until this point a shift towards smaller wavelength (blue shift) of the indirect band gap was observed. The shift was 0.3 eV, as shown in Figure 5.27 b). For thicker films an indirect band gap of 1.75 was observed, whereas for the thinnest films the indirect band gap was slightly above 2 eV. These values are in the lower region of values found in literature [48, 234].

The slope of the linear region, between 2.17 to 2.27 eV (Figure 5.27 b) is an estimation of the absorption coefficient (transition probability). This slope is similar down to 10 nm film thickness, for even thinner films the slope decreases rapidly. This is in agreement with the disappearance of the indirect transition for the thinnest films. The most probable cause for this behaviour is from correlating the absorption to the phonon behaviour present. As an indirect transition involves both the momentum transfer of a phonon and the absorption of a photon. For small structures with small extensions in some dimensions the spatial confinement could lead to a phonon suppression. This is seen for the Raman data in Figure 5.26 a), which point to the phonons to

be collectively suppressed for the thinnest films. This would decrease the probability of photons and phonons interacting, which is a necessity for the indirect transition. This is a reasonable explanation for the observations.

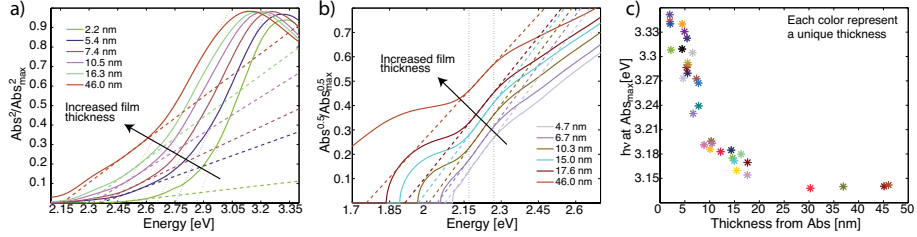


Figure 5.27. a) Determination of direct band gaps for a subset of the films. b) Determination of the indirect band gap for a subset of the films. c) Positions of the absorption maxima as a function of the thicknesses of the hematite films.

A direct transition is located at a higher photon energy, as discussed above. The absorption in this narrow energy interval is proportional to the square root of the energy split between the energy of the light and the band gap. The direct band gap can therefore be obtained by plotting the square of the absorption versus photon energy and extrapolating the linear region slightly above the band gap down to zero absorption. For an indirect semiconductor, this process is superimposed on the absorption, from the indirect transition. This could interfere with the analysis of the direct transition. However, the direct transition is a more probable process, which thus is stronger than the indirect transition and therefore make the analysis to be fairly accurate. In Figure 5.27 a), the square root of the absorption is plotted versus photon energy where two linear regions are found: the first between 2.45 to 2.60 eV and the second at slightly higher energies as expected.

The first region point to the presence of a direct transition for the thicker films around 2.15 eV. A blue shift for this transition is also observed where a shift of 0.3 eV is shown, Figure 5.28 b). For the second direct transition the blue shift is as large as 0.45 eV. The blue shift starts to occur at around 20 nm and accelerate towards the thinner films. This is an expected behaviour of an indirect transition.

The slope of the linear regions in Figure 5.27 a), relative to the probability of transition, differs with film thickness, as seen in Figure 5.28 c). The first direct transition decrease around 20 nm, and give very low probabilities for transition for the thinner films. For the second transition the slope increases with similar behaviour as the first transition. It is thus found that the probability of absorption for more energetic photons is increased in the thinner films at the expense of the absorption for the less energetic. This behaviour can be explained by electronic quantum confinement for the thinner films, which decrease the density of states for the lowest lying states in the conduction band.

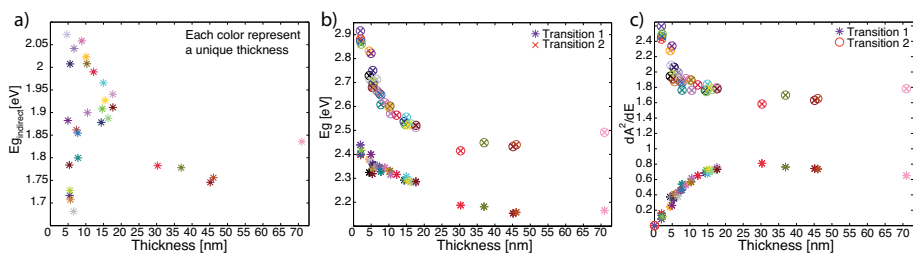


Figure 5.28. a) Indirect band gap as a function of the thickness of the deposited iron oxide. b) The energetic positions for the two direct transitions versus the film thickness for all the samples. c) Slope of the linear regions in 5.27 a) as a function of film thickness.

To summarise the optical measurements, a blue shift is observed for the absorption maximum for films with a thickness below 20 nm. This shows a change in the electronic structure, either a change in the density of states or in the orbital overlap for thin hematite films. A blue shift is also found in the absorption edges for both the direct and indirect transition, for the thinner films (<20 nm). It is also seen that the probability for absorption for the indirect transition at shorter wavelengths becomes smaller for the thinner films. This corresponds to a decrease in total optical absorption, in the visible region of the electromagnetic spectrum.

When hematite is used as a photo anode, the surface region will experience band bending where the holes are migrated to the surface and the electrons to the back contact. After this region, any charge separation is controlled by diffusion, with a hole diffusion length for hematite of only 2-4 nm [44, 68]. The thickness of the effective charge separation layer is then in the order of 17 nm or thinner [235]. The results here show that the absorption in this region is smaller than previously thought and has to be considered in an optimal device design.

6. Summary and Conclusion

In this thesis, atomic layer deposition a thin film deposition technique has been used to deposit the metal oxides: TiO_2 , $\alpha\text{-Fe}_2\text{O}_3$, $\gamma\text{-Fe}_2\text{O}_3$ and Fe_3O_4 . The aim of the study of the iron oxides were to investigate how the substrate influences the deposited film, what influence a carrier gas can have on the film, and how annealing of hematite films can enhance their photoelectrochemical performance. The aim of the TiO_2 films were to study how ultra thin films can improve 3D structured anodes.

Titania

TiO_2 were deposited from TiI_4 and H_2O as precursors on high aspect ratio aluminium pillars, with an excellent step coverage as deduced from TEM studies. At 200°C the anatase phase was deposited, whereas at 300°C the rutile phase was obtained. By using an thin film as cathode material in a battery, on the current collector the total capacity were increased 10 times, compared to a 2D system for the same footprint area 6.1 (Paper V).

Iron oxides

Iron oxide were deposited using two different iron precursors: ferrocene ($\text{Fe}(\text{Cp})_2$) and iron pentacarbonyl ($\text{Fe}(\text{CO})_5$) together with O_2 . The $\text{Fe}(\text{CO})_5$ and O_2 were used for depositions in Picosun while $\text{Fe}(\text{Cp})_2$ and O_2 were used for the iron oxide depositions in a hot wall tube reactor, as well in Picosun.

Nucleation and substrate dependance

The nucleation and substrate dependance study were performed with $\text{Fe}(\text{Cp})_2$ and O_2 . The different substrates used were TiO_2 , Al_2O_3 , Si (100), FTO and Quartz. The substrate dependence was obvious. A higher growth rate was observed on TiO_2 and Quartz, whereas on Si(100) and Al_2O_3 the growth rate

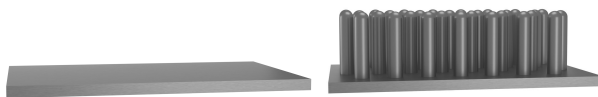


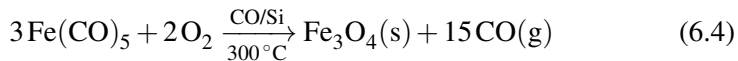
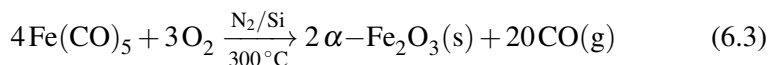
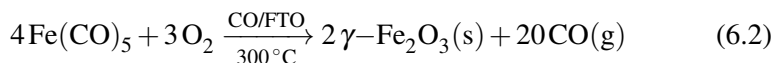
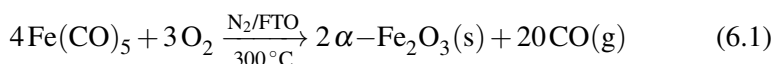
Figure 6.1. Illustration of how the surface are increases with pillars compared with a flat surface on the same footprint area.

was smaller, shown in Figure 5.14. The deposited material started to nucleate as islands on all the samples, and crystalline material was first observed at 20 nm film thickness. The exception was the iron oxide deposited on FTO, where hematite were observed below 10 nm. Annealing of the iron oxide deposited on Quartz showed that hematite could be formed at lower thicknesses.

Substrate dependance and carrier gas dependance

The $\text{Fe}(\text{CO})_5$ and O_2 as precursors were used to examine the diffusion of species from the FTO substrate in iron oxide upon annealing in different environments, influence of another carrier gas, and the optical properties of hematite films from 2-70 nm.

The influence of carrier gas, N_2 and CO together with either FTO or $\text{Si}(100)$ substrate was tested. The results are summarised in the reactions below:



The three iron oxides, hematite, magnetite or maghemite could be deposited by changing either the substrate or the carrier gas (at the same temperature and precursor used). This could be of interest if a multilayer structure is aimed for. Instead of working with two different metal containing precursors the carrier gas could be altered during the process giving a multilayer structure.

Diffusion of species from FTO into iron oxide upon annealing

The diffusion experiment was motivated from the knowledge that when hematite is doped the photocatalytic performance is increased. A set of iron oxides films on FTO were deposited and annealed in either vacuum or air, at temperatures between 550°C and 800°C .

Diffusion of silicon, tin and fluorine were observed using HAXPES. At higher temperatures the diffusion of the species increased. But the diffusion was also seen at the lowest annealing temperature. Figure 6.2 illustrate the tin diffusion, from the Fe 2p core level region it is visible that the tin signal ($\text{Sn } 3p_{3/2}$) increase with temperature. By using HAXPES, depth profiling was possible by changing the photon energy, revealing that the film did not change in composition, at the information depth reached using 6015 eV in photon energy. Sputtering of the samples made the film oxygen deficient, inducing a phase transformation from maghemite/hematite into wustite and metallic iron. This made the HAXPES measurement crucial for depth profiling.

The annealing also influenced the morphology of the iron oxide. For films annealed in air the structure coalesced to form bigger grains, whereas in vacuum the grains were smaller, since the environment suppressed grain growth.

The annealing environment also played a crucial role since the annealed samples in air were hematite, whereas the films annealed in vacuum were magnetite. This was observed using a combination of Raman spectroscopy, X-ray diffraction and hard X-ray photoelectron spectroscopy.

The films annealed in air showed an improvement in their photocatalytic behaviour, and photocurrent up to 0.23 mA/cm^2 was observed in the photooxidation of water. The as deposited film (hematite) and the films annealed in vacuum, were not photoactive at all. It can be concluded that the doping of hematite is crucial for the use of hematite in photoelectrochemical devices.

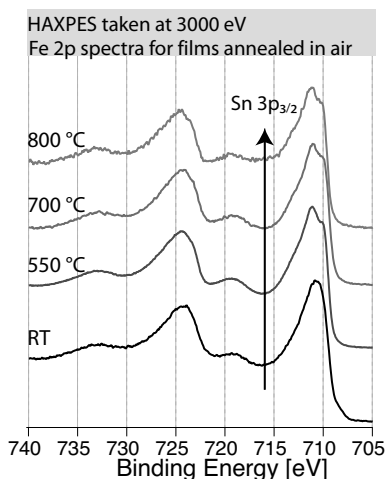


Figure 6.2. HAXPES for the Fe 2p core level, showing the Sn diffusion.

Quantum confinement

For the investigation of optical properties in low dimensional hematite a series of samples, ranging from 2-70 nm were produced.

The films were annealed at 500 °C for 8 hours in order to form hematite, and investigated with Raman spectroscopy and XRD to be certain of good film quality. The absorption maximum was shifted to higher energies for films thinner than 20 nm, visible in Figure 6.3. Revealing that the electronic structure change for films thinner than this. For the thinner films a blue shift were observed for both the indirect and the direct transition. This knowledge is of great importance for application of hematite as material for solar water splitting or other light active applications.

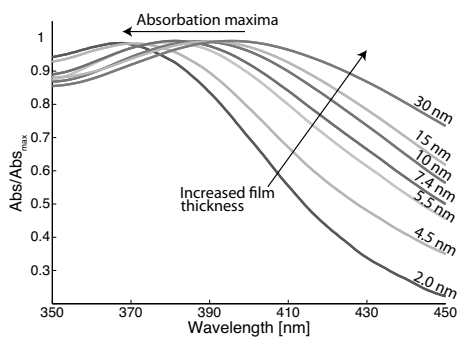


Figure 6.3. Absorption maximum change with film thickness.

Future prospects

For future work it would be interesting to locate the optimal annealing temperature, time, thickness and doping ratio in hematite. So a tailor made device could be tried to evaluate the limits of hematite for a solar water splitting application. Also to investigate the diffusion process of Sn, Si and F would be of great interest. Since there are very few articles investigating the diffusion of Si and F.

The logical following step is to deposit pyrite FeS_2 which is a very interesting material for solar cells due to its extraordinary high absorption coefficient. Precursors for an ALD process for depositing FeS_2 should be possible to find since there is a large amount of articles of metal sulphides deposited with ALD. Similar investigations would then be necessary to obtain the same information given in this thesis, how the band gap varies with size, absorption properties, possible dopants to mention a few areas.

7. Svensk sammanfattning

Egenskaper hos material är av yttersta vikt när de är tillverkade för ett specifikt användningsområde. Med hjälp av tunna ytskikt kan man ändra egenskaper på ytan av materialet som ligger under. Det kan räcka med allt ifrån ett par nanometer (1 nanometer (nm) är en miljarddels meter – 0.000000001 m) till mikrometer (1 mikrometer är en miljondels meter – 0.000001 m) tjocka filmer. För att kunna göra högkvalitativa filmer behövs en pålitlig tillverkningsteknik. Och när man kommer ner till tjocklekar i nanometer området så ställer det höga krav på tillverkningsprocessen, då det inte är många atomlager som utgör en nm. Till exempel så har det visat sig vara tillräckligt med 3 nm Al_2O_3 på litiumpartiklar för att ett batteri inte skall tappa i verkningsgrad med tiden. 2010 års nobelpris var baserat på grafen som är ett atomlager med kol, hexagonalt ordnade, vilket har en tjocklek på endast 0.34 nm.

Tjockleken på de filmer som diskuteras i den här avhandlingen är mellan 2 och 70 nm. Detta är väldigt tunt, men kan ändå ändra egenskaperna och materialets utseende helt.

En teknik som klarar av att deponera ett atomlager åt gången är atomlager deponering ("atomic layer deposition") (ALD). Tekniken bygger på att man har molekyler (reaktanter) i gasfas som reagerar med en yta, men inte med varandra i gasfas. Genom att ha två reaktanter och separera dem med hjälp av en inert gas kan man bygga upp material atomlager för atomlager. Genom att styra hur många pulser av de olika reaktanterna man använder kan man bestämma tjockleken av det deponerade materialet. Figur 7.1 är en illustration av tre atomlager av en substans med strukturformeln AB_2 . ALD har fördelen att man får en jämn tjocklek av materialet på ytan – även på porösa och på strukturerade material, detta tack vare att reaktanterna separeras.

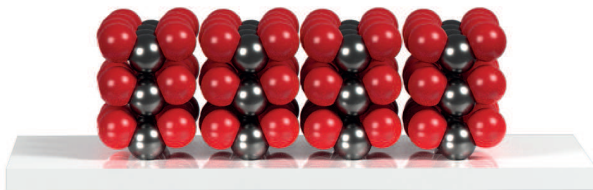


Figure 7.1. Illustration av tre cykler.

Ett exempel på en ALD process är om man skulle kombinera titantetraklorid (TiCl_4) och vatten (H_2O) som bildar titandioxid TiO_2 (Figur 7.1) med saltsyra

(HCl) som restprodukt. Restprodukten forslas bort av en inert gas varpå cykeln kan börja igen och ytterligare lager med titandioxid deponeras.

ALD är en tillverkningsteknik som används industriellt, t.ex. vid produktion av RAM-minnen till datorer. I RAM-minnen är man ute efter att ha en bra stegtäckning (d.v.s. täcka en strukturerad yta helt och hållet) i väldigt små kretsar. Andra applikationen kan vara ute efter att livslängden skall öka på en komponent, ofta är dessa filmer är tjockare.

Under min tid som doktorand har jag använt ALD för att göra tunna filmer av titandioxid och olika järnoxider. Det stora målet i projekten jag har varit involverad i har handlat om att försöka lösa någon form av energirelaterad fråga. Mitt fokus har dock främst varit på deponeringen, och analys av olika typer av filmer som växts med hjälp av ALD eller liknande tekniker.

TiO₂ deponerades på aluminiumstavar. Den stora anledningen till att använda 3D strukturer är att man ökar den effektiva ytarean, vilket illustreras i Figur 7.2. Dessa stavar kan användas i mikrobatterier, eller solceller. Genom att ha en nanustrukturerad yta med TiO₂ lyckades vi öka kapaciteten hos batteriet 10 gånger, jämfört med en plan yta. Tunnsfilmen gjorde även att batteriet ej matades ut, utan kom upp i likvärdig kapacitet efter att urladdning hade gjorts.

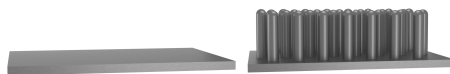


Figure 7.2. Jämförelse hur ytarean ökar när man har struktur på ytan. Bilden visar exempel när man har pelare på ytan.

Järnoxider som behandlas i avhandlingen är wustit FeO, hematit α -Fe₂O₃, magnetit Fe₃O₄ och maghemit γ -Fe₂O₃. Järnoxider är intressanta eftersom de är miljövänliga och stabila – två nödvändiga egenskaper om de ska användas i stor skala för någon tillämpning. Till exempel är rost en form av järnoxid – ett nödvändigt ont kanske man tänker – men järnoxider har många intressanta applikationsområden. Ett område som ökat intresse det senaste årtiondet är att använda hematit som solcellsmaterial, alternativt för vätgasproduktion med hjälp av solljus.

Alla materialegenskaper hos hematit är dock inte ideala för den senare applikationen – den största nackdelen är att hematit besitter en "kort diffusionslängd för de fotogenererade hålen". När solljus träffar materialet så absorberar materialet energin genom att en negativt elektron hamnar i ett högre energitillstånd, den lämnar efter sig ett "hål" som är positivt laddat (summan av laddningarna skall vara noll). För att vi ska kunna dra nytta av elektronen och hålet måste de kunna separeras – stannar de för länge i närheten av varandra så finner de varandra åter och energin absorberas som värme eller återutsänds som en foton. Att hålen har en kort diffusionslängd innebär att de stannar länge på samma ställe och det är alltså lätt för elektroner att hitta dessa. Detta medför att hematit måste vara i form av nanopartiklar eller tunna filmer för att de skall fungera inom ovanstående föreslagna applikationer, vilket potentiellt minskar materialets konkurrenskraft i förhållande till andra material.

Jag har till stor del fokuserat på tillverkande av tunna filmer av järnoxid. Detta för att karakterisera ett flertal olika aspekter hos materialet: kunna deponera rätt fas av järnoxid, då det är små skillnader hos de ovan nämnda järnoxiderna, betydelsen av vilket substrat som används, hur den bärgas som används under tillverkningsprocessen påverkar slutprodukten, samt hur diffusion från substratet kan förbättra egenskaper hos hematit.

Det substrat som användes, visade sig ha stor betydelse på den deponerade järnoxiden. Vid användandet av fluordopad tennoxid (FTO) kunde man se att hematit tillkom redan vid en tjocklek av runt 5 nm. På de andra substraten observerades hematit först vid en tjocklek av runt 20 nm. Även tillväxthastigheten skiljde sig åt beroende på substrat. Anledningen till dessa olika beteenden är troligen att vissa substrat matchar hematits struktur bättre än de andra – detta gör att tillväxten blir hastigare på dessa substrat.

Betydelsen av vilken bärgas som användes under ALD processen visade att man kunde styra vilken fas av järnoxid som deponerades. Genom att använda kolmonoxid (CO) istället för kvävgas (N_2) som kunde vi växa antingen $\gamma\text{-Fe}_2\text{O}_3$ (med CO) eller $\alpha\text{-Fe}_2\text{O}_3$ (med N_2) på FTO. När kisel användes som substrat fick man dessutom Fe_3O_4 vid användandet av CO som bärgas. Genom att skräddarsy tillverkningsprocessen kunde vi därför deponera tre olika järnoxider.

Ett möjligt sätt att öka prestandan hos hematitbaserade komponenter för vattensplittring är att värma den film som deponerats på FTO i luft till ca. 800 °C. Ett alternativ eller komplement till detta är att modifiera innehållet i filmen genom att addera andra atomslag (dopning). Båda strategierna har till syfte att ändra på de elektroniska egenskaperna hos kombinationen av substrat och tunnfilm så att vattensönderdelningen blir så effektiv som möjligt.

För att se om det fanns någon diffusion av ämnen från substratet vid uppvärmning av hematit gjordes det filmer med ungefär samma tjocklek, mellan 40-60 nm. För att kunna undersöka möjlig diffusion utfördes analyserna med hjälp utav synkrotronljusbaserad fotoelektronspektroskopi (XPS). Den stora fördelen med den här tekniken är att man kan undersöka olika djup i provet, genom att ändra den inkommande fotonenergin, utan att förstöra provet. För att kunna göra en djupprofil genom att ändra fotonenergin utfördes dessa experiment med hjälp av synkrotronljus på Bessy II i Berlin. Värmebehandling gjordes vid temperaturer mellan 550 °C och 800 °C i luft och i vakuum. Diffusion från substratet var tydlig vid alla temperaturer, med en ökning vid de högre temperaturerna. Från resultaten kunde man se att både tenn och kisel diffunderade från substratet, även fluor observerades på ett prov.

Efter värmebehandlingen sågs även att de prov som värmebehandlades i luft omvandlades till hematit, och de som värmebehandlingen i vakuum omvandlades till magnetit.

Med hjälp av diffusionen fick vi en ökad fotokatalytisk aktivitet på filmerna som värmebehandlades i luft. Medan den ursprungliga filmen och de behandlade i vakuum inte visade upp någon fotokatalytisk aktivitet alls. Vilket visar

att värmebehandling är viktigt om tunna filmer av hematit skall kunna användas för vätgasproduktion genom att med solljus att sönderdela vatten, $2 \text{H}_2\text{O} \longrightarrow 2 \text{H}_2 + \text{O}_2$.

Det gjordes även en undersökning om hur tjockleken på hematit påverkade absorptionen av fotoner. En tjockleksserie mellan 2 till 70 nm av hematit på ledande glas deponerades med ALD. De optiska mätningarna visade att absorptionen ändrades och berodde på tjockleken. Absorptionsmaximat ändrades mot högre energier för hematitfilmer tunnare än 20 nm. Våra resultat visar att hematit behöver en större absorptionsvolym än vad tidigare angivits, då den optiska absorptionen minskar i det synliga området för tunnare filmer än 20 nm.

Det betyder inte att hematit blir ointressant för vätgasproduktion, men att det finns hinder att övervinna för att få materialet att fungera optimalt i denna tillämpning. I den här avhandlingen så har vi undersökt ett antal olika sätt att kringgå några av dessa hinder.

Acknowledgements

First I would like to address my appreciation to my main supervisor Mats Boman. You were the one who inspired me and also gave me the opportunity to start my Ph D studies, and introducing me to a very interesting research field, from AAO to ALD. The dinners in Järlåsa is something I will remember. Tomas, thank you for great conversations and all help with the projects and always having the door open when I have questions. Andreas, for introducing me to HAXPES and taking me on board. For all the help with writing (L^AT_EX), imaging (Adobe Illustrator) and great trips to Bessy. For always being available either during night shifts in Berlin or during the Summer Suite -14. Rebecka for help during the beamtime and for the hospitality in the end. To Isak for having a great set of parents.

To all co-authors for collaboration. Especially Jesper and Mihaela for sharing your expertise. To Mårten for collaboration in and outside of the university and tips and tricks concerning bikes. To Indrek for a great year working together. Jan-Otto Carlsson for sharing knowledge and good meetings.

Anna F, for supporting me, hope to see you in Sandviken. Erik L₁ and Erik L₂ for taking me under your wings, at work and on the side, hopefully it does not end here. Martin for always being helpful and sharing knowledge. Fredrik, Nils and Jonas M for the lunch time training sessions, skiing trips, several discussions and a lot more. Jill and Matilda for help and support throughout the years and fun trips around the world. A special thanks to Linus for help at the end. Viktor for great times at the office and Rickard for the memorable performance The Modern Man. Adam for nice discussions about music outside work. Yiming, Song and Tian for always being honest and for fun discussions and good Chinese food.

The technical and administrative staff at the Department of Chemistry Ångström. Eva and Tatti for guidance and for always being so helpful, do not know how I would have managed without you. Anders L and Jan B for help with everything involving building new experimental setups.

My gratitude goes of course also to the rest of my colleagues at materials chemistry for discussions, nice parties and coffee breaks.

Magnus, Tobias, Per, Markve, Svante, Jakob, Mauro, Christian R, C-Micke, Carl Johan M and Karl for your support and for gaming nights, barbeques, great parties and a lot more. Fredrik J for making it a lot more fun to be at work in July.

Teresa Z, Jesper G and Timo for the best gatherings together with card games. You know who's in the top two!

David M for always being helpful and a great friend, for images in the thesis, gaming nights, wine drinking and a lot more.

To Orphei Drängar, Allmänna Sången, Svenska Showorkesteren, Phontrattarna, Värmlands Nationskör, Tupplurarna, Östgöta Nationskapell for letting me practice my passion for music, either with my voice or trombone, and for a great set of trips around the world. My gratitude goes of course also to the rest of my friends, for making the last five years infinitely more fun than I ever could expect.

Min triss i systrar, Sofia, Amelie och Elin med familjer för support och att ni alltid finns där. För spelkvällar, avkoppling eller nya träningspass. Teo för att du har givit mig kraft och ett uppvaknande att det ibland funkar att gå till en lekplats och allt blir genast mycket roligare.

Mormor och Morfar för att ni alltid ger inspiration. Farmor för att du alltid gav mig inspiration och trodde på mig.

Mamma och Pappa för ni alltid ger stöd i motgång/medgång och för att ni alltid ställer upp oavsett om det skulle skjutsas till repetitioner eller när jag behöver råd om hur jag skall göra saft. Ni är bäst.

References

- [1] J. K. Casper. *Fossil fuels and pollution: the future of air quality*. Infobase Publishing (2010).
- [2] D. Fantazzini, M. Höök, and A. Angelantoni. *Energy Policy*, **39**, 7865 – 7873 (2011).
- [3] L. Maugeri. *Review of Environmental Economics and Policy*, pages 1–20 (2009).
- [4] T. Barker, P. Ekins, and N. Johnstone. *Global warming and energy demand*. Routledge (2005).
- [5] F. Drake. *Global Warming*. Routledge (2014).
- [6] M. Birkholz. *Thin film analysis by X-ray scattering*. John Wiley & Sons (2006).
- [7] Commercially available 3D transistor from intel, 22 nm (2014). URL <http://goo.gl/XH937A>.
- [8] G. Moore et al. Cramming more components onto integrated circuits (1965).
- [9] J-S. Park, H. Chae, H. K. Chung, and S. I. Lee. *Semiconductor Science and Technology*, **26**, 034001 (2011).
- [10] J. A. Thornton and J. E. Greene. Sputter deposition processes. *Handbook of Deposition Technologies for Films and Coatings, 2nd ed.*(Noyes Publications), pages 249–319 (1994).
- [11] H. O. Pierson. *Handbook of chemical vapor deposition: principles, technology and applications*. William Andrew (1999).
- [12] J-O. Carlsson. *Thin Solid Films*, **130**, 261–282 (1985).
- [13] K. L. Choy. *Progress in Material Science*, **48**, 57–170 (2003).
- [14] S. M. George. *Chemical Reviews*, **110**, 111 (2010).
- [15] R. L. Puurunen. *Journal of Applied Physics*, 97(12)121301 (2005).
- [16] V. Miikkulainen, M. Leskelä, M. Ritala, and R. L. Puurunen. *Journal of Applied Physics*, 113(2)021301 (2013).
- [17] N. Pinna and M. Knez. *Atomic Layer Deposition of Nanostructured Materials*. John Wiley & Sons (2012).
- [18] M. Knez, K. Nielsch, and L. Niinistö. *Advanced Materials*, **19**, 3425–3438 (2007).

- [19] M. D. Groner, F. H. Fabreguette, J. W. Elam, and S. M. George. *Chemistry of Materials*, **16**, 639–645 (2004).
- [20] X. Liang, S. M. George, A. W. Weimer, N-H. Li, J. H. Blackson, J. D. Harris, and P. Li. *Chemistry of Materials*, **19**, 5388–5394 (2007).
- [21] M. J. Biercuk, D. J. Monsma, C. M. Marcus, J. S. Becker, and R. G. Gordon. *Applied Physics Letters*, **83**, 2405–2407 (2003).
- [22] R. L. Puurunen, W. Vandervorst, W. F. A. Besling, O. Richard, H. Bender, T. Conard, C. Zhao, A. Delabie, M. Caymax, S. De Gendt, et al. *Journal of Applied Physics*, **96**, 4878–4889 (2004).
- [23] D. S. Taylor, M. K. Jain, and T. S. Cale. *Journal of Vacuum Science & Technology A*, **16**, 3123–3126 (1998).
- [24] W. FA. Besling, M-L. Ignacimouttou, A. Humbert, M. Mellier, and J. Torres. *Microelectronic Engineering*, **76**, 60–69 (2004).
- [25] G. Radhakrishnan, R. E. Robertson, R. C. Cole, and P. M. Adams. *Applied Physics A*, **77**, 175–184 (2003).
- [26] G. Depinto, S. Dunnigan, K. Schwechel, and B. Mishra. *Journal of Electronic Materials*, **26**, 376–382 (1997).
- [27] J. K. Lan, Y-L. Wang, C. G. Chao, K-Y. Lo, and Y. L. Cheng. *Journal of Vacuum Science & Technology B*, **21**, 1224–1229 (2003).
- [28] G. B. Raupp and T. S. Cale. *Chemistry of Materials*, **1**, 207–214 (1989).
- [29] T. S. Cale, D. F. Richards, and D. Yang. *Journal of Computer-Aided Materials Design*, **6**, 283–309 (1999).
- [30] G. Ozaydin-Ince and K. K. Gleason. *Chemical Vapor Deposition*, **16**, 100–105 (2010).
- [31] J. Kim, H. Hong, K. Oh, and C. Lee. *Applied Surface Science*, **210**, 231–239 (2003).
- [32] T. M. Mayer, J. W. Elam, S. M. George, P. G. Kotula, and R. S. Goeke. *Applied Physics Letters*, **82**, 2883–2885 (2003).
- [33] J. W. Elam, D. Routkevitch, P. P. Mardilovich, and S. M. George. *Chemistry of Materials*, **15**, 3507–3517 (2003).
- [34] H. Kim, H-B-R. Lee, and W-J. Maeng. *Thin Solid Films*, **517**, 2563–2580 (2009).
- [35] B. H. Kong, M. K. Choi, H. K. Cho, J. H. Kim, S. Baek, and J-H Lee. *Electrochemical and Solid-State Letters*, **13**, K12–K14 (2010).
- [36] I. L. Soroka, M. Rooth, J. Lu, M. Boman, P. Svedlindh, J-O. Carlsson, and A. Hårsta. *Journal of Applied Physics*, 106(8)084313 (2009).
- [37] S. K. Cheah, E. Perre, M. Rooth, M. Fondell, A. Hårsta, L. Nyholm, M. Boman, T. Gustafsson, J. Lu, P. Simon, and K. Edström. *Nano Letters*, **9**,

3230–3233 (2009).

- [38] Picosun (2014). URL <http://www.picosun.com/en/products/roll-to-roll+ald+chamber/>.
- [39] Beneq (2014). URL <http://www.beneq.com/tfs-200r.html>.
- [40] M. D. Archer and R. Hill. *Clean electricity from photovoltaics*. World Scientific (2001).
- [41] C. A. Grimes, O. K. Varghese, and S. Ranjan. *Light, water, hydrogen: the solar generation of hydrogen by water photoelectrolysis*. Springer (2007).
- [42] M. Grätzel. *Nature*, **414**, 338–344 (2001).
- [43] A. Fujishima and K. Honda. *Nature*, **238**, 37–38 (1972).
- [44] J. H. Kennedy and K. W. Frese. *Journal of The Electrochemical Society*, **125**, 709 (1978).
- [45] K. Sivula, F. Le Formal, and M. Grätzel. *ChemSusChem*, **4**, 432 (2011).
- [46] D. K. Bora, A. Braun, and E. C. Constable. *Energy & Environmental Science*, **6**, 407 (2013).
- [47] M. J. Katz, S. C. Riha, N. C. Jeong, A. B. F. Martinson, O. K. Farha, and J. T. Hupp. *Coordination Chemistry Reviews*, **256**, 2521 (2012).
- [48] D. A. Wheeler, G. Wang, Y. Ling, Y. Li, and J. Z. Zhang. *Energy & Environmental Science*, **5**, 6682 (2012).
- [49] R. M. Cornell and U. Schwertmann. *The Iron Oxides*. Wiley-VCH, 2nd edition (2003).
- [50] M. Ni, M. K. H. Leung, D. Y. C. Leung, and K. Sumathy. *Renewable & Sustainable Energy Reviews*, **11**, 401 (2007).
- [51] J. H. Park, S. Kim, and A. J. Bard. *Nano Letters*, **6**, 24 (2006).
- [52] V. Cristino, S. Caramori, R. Argazzi, L. Meda, G. L. Marra, and C. A. Bignozzi. *Langmuir*, **27**, 7276 (2011).
- [53] R. Liu, Y. Lin, L.-Y. Chou, S. W. Sheehan, W. He, F. Zhang, H. J. M. Hou, and D. Wang. *Angewandte Chemie International Edition*, **50**, 499 (2011).
- [54] A. Iwase and A. Kudo. *Journal of Materials Chemistry*, **20**, 7536 (2010).
- [55] Y. Liang, T. Tsubota, L. P. A. Mooij, and R. Van De Krol. *The Journal of Physical Chemistry*, **115**, 17594 (2011).
- [56] A. Wolcott, W. A. Smith, T. R. Kuykendall, Y. Zhao, and J. Z. Zhang. *Advanced Functional Materials*, **19**, 1849 (2009).
- [57] T. J. Jacobsson and T. Edvinsson. *RSC Advances*, **2**, 10298 (2012).
- [58] T. J. Jacobsson, V. Fjällström, M. Sahlberg, M. Edoff, and T. Edvinsson. *Energy & Environmental Science*, **6**, 3676 (2013).

- [59] A. Paracchino, V. Laporte, K. Sivula, M. Grätzel, and E. Thimsen. *Nature Materials*, **10**, 456 (2011).
- [60] Z. Zhang and P. Wang. *Journal of Materials Chemistry*, **22**, 2456 (2012).
- [61] J. Brilliet, J-H. Yum, M. Cornuz, T. Hisatomi, R. Solarska, J. Augustynski, M. Graetzel, and K. Sivula. *Nature Photonics*, **6**, 823 (2012).
- [62] T. J. Jacobsson, C. Platzer-Björkman, M. Edoff, and T. Edvinsson. *International Journal of Hydrogen Energy*, **38**, 15027 (2013).
- [63] J. J. Sakurai. *Modern Quantum Mechanics*. Addison Wesley Longman, New York (1994).
- [64] Image for maghemite mineral (2014). URL <http://goo.gl/2uK6g5>.
- [65] R. K. Quinn, R.D. Nasby, and R.J. Baughman. *Materials Research Bulletin*, **11**, 1011 – 1017 (1976).
- [66] K. L. Hardee and A. J. Bard. *Journal of The Electrochemical Society*, **123**, 1024–1026 (1976).
- [67] J. Kiwi and M. Gratzel. *Journal of the Chemical Society, Faraday Transactions 1*, **83**, 1101–1108 (1987).
- [68] N. J. Cherepy, D. B. Liston, J. A. Lovejoy, H. Deng, and J. Z. Zhang. *Journal of Physics B*, **102**, 770 (1998).
- [69] M. P. Dare-Edwards, J. B. Goodenough, A. Hamnett, and P. R. Trevellick. *Journal of the Chemical Society, Faraday Transactions 1*, **79**, 2027 (1983).
- [70] S. D. Tilley, M. Cornuz, K. Sivula, and M. Grätzel. *Angewandte Chemie International Edition*, **49**, 6405 (2010).
- [71] M. Fondell, M. Gorgoi, L. Von Fieandt, A. Lindblad, and M. Boman. Phase Control of Iron Oxides Grown in Nano-Scale Cauliflower Structures: Hematite, Maghemite and Magnetite. Submitted to Vacuum (2014).
- [72] J. A. Glasscock, P. R. F. Barnes, I. C. Plumb, and N. Savvides. *The Journal of Physical Chemistry C*, **111**, 16477 (2007).
- [73] I. Cesar, A. Kay, J. A. Gonzalez Martinez, and M. Grätzel. *Journal of the American Chemical Society*, **128**, 4582 (2006).
- [74] I. Cesar, K. Sivula, A. Kay, R. Zboril, and M. Grätzel. *Journal of Physics C: Solid State Physics*, **117**, 772 (2009).
- [75] W. D. Chemelewski, N. T. Hahn, and C. B. Mullins. *The Journal of Physical Chemistry C*, **116**, 5255 (2012).
- [76] O. Zandi, B. M. Klahr, and T. W. Hamann. *Energy & Environmental Science*, **6**, 634 (2013).
- [77] J. S. Jang, J. Lee, H. Ye, F. F. Fan, and A. J. Bard. *The Journal of Physical Chemistry C*, **113**, 6719 (2009).

- [78] S. Kumari, A. P. Singh, D. Deva, R. Shrivastav, S. Dass, and V. R. Satsangi. *International Journal of Hydrogen Energy*, **35**, 3985 (2010).
- [79] N. T. Hahn and C. B. Mullins. *Chemistry of Materials*, **22**, 6474–6482 (2010).
- [80] C. Jorand Sartoretti, B. D. Alexander, R. Solarska, I. Rutkowska, J. Augustynski, and R. Cerny. *Journal of Physics B: Atomic, Molecular and Optical Physics*, **109**, 13685 (2005).
- [81] L. Shipu, Z. Peng, S. Xuefeng, and G. Lian. *International Journal of Hydrogen Energy*, **39**, 14596 – 14603 (2014).
- [82] W. B. Ingler Jr and S. U. M. Khan. *Thin Solid Films*, **461**, 301 (2004).
- [83] M. Gaudon, N. Pailhé, J. Majimel, A. Wattiaux, J. Abel, and A. Demourgues. *Journal of Solid State Chemistry*, **183**, 2101 (2010).
- [84] V. Satsangi, S. Kumari, A. Singh, R. Shrivastav, and S. Dass. *International Journal of Hydrogen Energy*, **33**, 312 (2008).
- [85] A. Kleiman-Shwarscstein, Y-S. Hu, A. J. Forman, G. D. Stucky, and E. W. Mcfarland. *The Journal of Physical Chemistry C*, **112**, 15900 (2008).
- [86] Y-S. Hu, A. Kleiman-Shwarscstein, A. J. Forman, D. Hazen, J-N Park, E. W. Mcfarland, and S. Barbara. *Chemistry of Materials*, **20**, 3803 (2008).
- [87] J. Liu, Y.Y. Cai, Z.F. Tian, G.S. Ruan, Y.X. Ye, C.H. Liang, and G.S. Shao. *Nano Energy*, **9**, 282 – 290 (2014).
- [88] Y. Ling, G. Wang, D. A. Wheeler, J.Z. Zhang, and Y. Li. *Nano Letters*, **11**, 2119 (2011).
- [89] L. Wang, C-Y. Lee, A. Mazare, K. Lee, J. Müller, E. Spiecker, and P. Schmuki. *Chemistry - A European Journal*, **20**, 77 (2014).
- [90] K. Sivula, R. Zboril, F. Le Formal, R. Robert, A. Weidenkaff, J. Tucek, J. Frydrych, and M. Grätzel. *Journal of the American Chemical Society*, **132**, 7436 (2010).
- [91] H. Uchiyama, M. Yukizawa, and H. Kozuka. *The Journal of Physical Chemistry C*, **115**, 7050–7055 (2011).
- [92] V. M. Aroutiounian, V. M. Arakelyan, G. E. Shahnazaryan, H. R. Hovhannisyan, H. Wang, and J. A. Turner. *Solar Energy*, **81**, 1369–1376 (2007).
- [93] D. L. A. De Faria, S. Venâncio Silva, and M. T. De Oliveira. *Journal of Raman Spectroscopy*, **28**, 873–878 (1997).
- [94] G. Yasumasa. *Japanese Journal of Applied Physics*, **3**, 739 (1964).
- [95] R. Dronskowski. *Advanced Functional Materials*, **11**, 27–29 (2001).
- [96] A. S. Teja and P-Y. Koh. *Progress in Crystal Growth and Characterization of Materials*, **55**, 22 – 45 (2009).

- [97] P. Majewski and B. Thierry. *Critical Reviews in Solid State and Materials Sciences*, **32**, 203–215 (2007).
- [98] G. N. Parsons, J. W. Elam, S. M. George, S. Haukka, H. Jeon, E. Kessels, M. Leskelä, P. Poodt, M. Ritala, and S. M. Rossnagel. *Journal of Vacuum Science & Technology A*, **31**(5)050818 (2013).
- [99] S I Kol'tsov, G N Kuznetsova, and V B Aleskovskii. *Zh. Prikl. Khim.*, **40**, 2774–2777 (1967).
- [100] S. I. Kol'tsov. *Zh. Prikl. Khim. (English translation)*, **42**, 975–979 (1969).
- [101] S. I. Kol'tsov. In *Abstract of Scientific and Technical Conference*, page 27, Leningrad (1963).
- [102] S. I. Kol'tsov, G. N. Kuznetsova, and V. B. Aleskovskii. *Zh. Prikl. Khim. (English translation)*, **40**, 2644–2646 (1967).
- [103] M. Ritala, K. Kukli, A. Rahtu, P. I. Räisänen, M. Leskelä, T. Sajavaara, and J. Keinonen. *Science*, **288**, 319–321 (2000).
- [104] V.E. Drozd, A.A. Tulub, V.B. Aleskovski, and D.V. Korol'kov. *Applied Surface Science*, **82-83**, 587 – 590 (1994).
- [105] C. Detavernier, J. Dendooven, S. P. Sree, K. F. Ludwig, and J. A. Martens. *Chemical Society Reviews*, **40**, 5242–5253 (2011).
- [106] J. Aarik, A. Aidla, T. Uustare, and V. Sammelselg. *Journal of Crystal Growth*, **148**, 268 – 275 (1995).
- [107] J. A. Venables, G. D. T. Spiller, and M. Hanbucken. Nucleation and growth of thin films. *Reports on Progress in Physics*, **47**, 399 (1984).
- [108] D. M. Hausmann and R. G. Gordon. *Journal of Crystal Growth*, **249**, 251 – 261 (2003).
- [109] D. R. G. Mitchell, G. Triani, D. J. Attard, K. S. Finnie, P. J. Evans, C. J. Barbé, and J. R. Bartlett. *Smart Materials and Structures*, **15**, S57 (2006).
- [110] R. L. Puurunen, J. Saarilahti, and H. Kattelus. *ECS Transactions*, **11**, 3–14 (2007).
- [111] R. L. Puurunen, T. Sajavaara, E. Santala, V. Miikkulainen, T. Saukkonen, M. Laitinen, and M. Leskelä. *Journal of Nanoscience and Nanotechnology*, **11**, 8101–8107 (2011).
- [112] O. Nilsen, O. B. Karlsen, A. Kjekshus, and H. Fjellvåg. *Thin Solid Films*, **515**, 4527 – 4537 (2007).
- [113] O. Nilsen, O. B. Karlsen, A. Kjekshus, and H. Fjellvåg. *Thin Solid Films*, **515**, 4538 – 4549 (2007).
- [114] O. Nilsen, O. B. Karlsen, A. Kjekshus, and H. Fjellvåg. *Thin Solid Films*, **515**, 4550 – 4558 (2007).

- [115] O. Nilsen, O. B. Karlsen, A. Kjekshus, and H. Fjellvåg. *Journal of Crystal Growth*, **308**, 366 – 375 (2007).
- [116] E. Lindahl, J. Lu, M. Ottosson, and J-O. Carlsson. *Journal of Crystal Growth*, **311**, 4082–4088 (2009).
- [117] Picosun (2014). URL <http://www.picosun.com/en/products/picosun8482+r-series/>.
- [118] J. Aarik, A. Aidla, T. Uustare, K. Kukli, V. Sammelselg, M. Ritala, and M. Leskelä. *Applied Surface Science*, **193**, 277 – 286 (2002).
- [119] M. Rooth, R. A. Quinlan, E. Widenkvist, J. Lu, H. Grennberg, B. C. Holloway, A. Hårsta, and U. Jansson. *Journal of Crystal Growth*, **311**, 373 – 377 (2009).
- [120] E. Perre, L. Nyholm, T. Gustafsson, P-L. Taberna, P. Simon, and K. Edström. *Electrochemistry Communications*, **10**, 1467 – 1470 (2008).
- [121] M. Aronniemi, J. Saino, and J. Lahtinen. *Thin Solid Films*, **516**, 6110 – 6115 (2008).
- [122] M. de Ridder, P. C. van de Ven, R. G. van Welzenis, H. H. Brongersma, S. Helfensteyn, C. Creemers, P. Van Der Voort, M. Baltes, M. Mathieu, and E. F. Vansant. *Journal of Physical Chemistry B*, **106**, 13146–13153 (2002).
- [123] K. Zhou, J-Q. Huang, Q. Zhang, and F. Wei. *Nanoscale Research Letters*, **5**, 1555–1560 (2010).
- [124] O. Nilsen, M. Lie, S. Foss, H. Fjellvåg, and A. Kjekshus. *Applied Surface Science*, **227**, 40 – 47 (2004).
- [125] L. Hannevold, O. Nilsen, A. Kjekshus, and H. Fjellvåg. *Applied Catalyst A*, **284**, 177 – 184 (2005).
- [126] J. A. Libera, J. W. Elam, N. F. Sather, T. Rajh, and N. M. Dimitrijevic. *Chemistry of Materials*, **22**, 409–413 (2010).
- [127] M. Lie, H. Fjellvåg, and A. Kjekshus. *Thin Solid Films*, **488**, 74 – 81 (2005).
- [128] M. Rooth, A. Johansson, K. Kukli, J. Aarik, M. Boman, and A. Hårsta. *Chemical Vapor Deposition*, **14**, 67–70 (2008).
- [129] J. R. Scheffe, A. Francés, D. M. King, X. Liang, B. A. Branch, A. S. Cavanagh, S. M. George, and A. W. Weimer. *Thin Solid Films*, **517**, 1874 – 1879 (2009).
- [130] J. Escrig, J. Bachmann, J. Jing, M. Daub, D. Altbir, and K. Nielsch. *Physical Review B*, **77**, 214421 (2008).
- [131] X. Li, N. C. Fan, and H. J. Fan. *Chemical Vapor Deposition*, **19**, 104–110 (2013).
- [132] K. Pitzschel, J. M. M. Moreno, J. Escrig, O. Albrecht, K. Nielsch, and J. Bachmann. *ACS Nano*, **3**, 3463–3468 (2009).
- [133] S. B. Lim, A. Rahtu, and R. G. Gordon. *Nature Materials*, **2**, 749–754 (2003).

- [134] J. Bachmann, J. Escrig, K. Pitzschel, J. M. M. Moreno, J. Jing, D. Görlitz, D. Altbir, and K. Nielsch. *Journal of Applied Physics*, **105**, 07 (2009).
- [135] J. Bachmann, Jing, M. Knez, S. Barth, H. Shen, S. Mathur, U. Gösele, and K. Nielsch. *Journal of the American Chemical Society*, **129**, 9554–9555 (2007).
- [136] K. Kukli, M. C. Dimri, A. Tamm, M. Kemell, T. Käämbre, M. Vehkamäki, M. Puttaswamy, R. Stern, I. Kuusik, A. Kikas, et al. *ECS Journal of Solid State Science and Technology*, **2**, N45–N54 (2013).
- [137] S. C. Riha, J. M. Racowski, M. P. Lanci, J. A. Klug, A. S. Hock, and A. B. F. Martinson. *Langmuir*, **29**, 3439–3445 (2013).
- [138] A. B. F. Martinson, M. J. DeVries, J. A. Libera, S. T. Christensen, J. T. Hupp, M. J. Pellin, and J. W. Elam. *Journal of Physical Chemistry*, **115**, 4333–4339 (2011).
- [139] M. Rooth, A. Johansson, K. Kukli, J. Aarik, M. Boman, and A. Hårsta. *Chemical Vapor Deposition*, **14**, 67–70 (2008).
- [140] A. G. Gilbert and K. G. P. Sulzmann. *Journal of the Electrochemical Society*, **121**, 832–834 (1974).
- [141] NIST entry for $TiCl_4$ (2014). URL <http://googl/UCj0iD>.
- [142] N. M. Dawson. Atomic Layer Deposition of Aluminum Oxide. Master's thesis, University of California, Santa Cruz (2010).
- [143] D. JH. Emslie, P. Chadha, and J. S. Price. *Coordination Chemistry Reviews*, **257**, 3282–3296 (2013).
- [144] B. E. Warren. *X-ray Diffraction*. Courier Dover Publications (1969).
- [145] J. B. Cohen and L. B. Schwartz. *Diffraction from Materials*. Springer-Verlag, New York & Berlin (1987).
- [146] A. Segmüller, I. C. Noyan, and V. S. Speriosu. *Progress in Crystal Growth and Characterization*, **18**, 21–66 (1989).
- [147] L. S. Birks. *X-ray spectrochemical analysis*. Interscience New York (1969).
- [148] R. Jenkins. *An introduction to X-ray spectrometry*. Heyden, London (1974).
- [149] M. O. Krause. *Journal of physical and chemical reference data*, **8**, 307–327 (1979).
- [150] P. M. Fauchet and I. H. Campbell. *Critical Reviews in Solid State and Materials Sciences*, **14**, s79–s101 (1988).
- [151] D. A. Long. *Raman Spectroscopy*, volume 206. McGraw-Hill New York (1977).
- [152] N. B. Colthup, L. H. Daly, and S. E. Wiberley. *Introduction to infrared and Raman spectroscopy*. Elsevier (1990).

- [153] E. Hecht. *Optics 4th edition*, volume 1. Addison-Wesley Publishing Company (2001).
- [154] A. Messiah. *Quantum Mechanics*. Dover books on physics. Dover Publications (1999).
- [155] J. I. Goldstein, D. E. Newbury, P. Echlin, D. C. Joy, C. Fiori, E. Lifshin, et al. *Scanning electron microscopy and X-ray microanalysis. A text for biologists, materials scientists, and geologists*. Plenum Publishing Corporation (1981).
- [156] H. Hertz. *Annalen der Physik*, **267**, 983–1000 (1887).
- [157] A. Einstein. *Annalen der Physik*, **322**, 132–148 (1905).
- [158] K. Siegbahn, C. Nordling, A. Fahlman, R. Nordberg, K. Hamrin, J. Hedman, G. Johansson, T. Bergmark, S.-E. Karlsson, I. Lindgren, and B. Lindberg. *ESCA Atomic, Molecular and Solid State Structure Studied by means of Electron Spectroscopy*. Almquist and Wiksells, Uppsala (1967).
- [159] K. Siegbahn, C. Nordling, R. Fahlman, R. Nordberg, K. Hamrin, J. Hedman, G. Johansson, T. Bergmark, S.-E. Karlsson, I. Lindgren, and B. Lindberg. *ESCA, Atomic, Molecular and Solid State Structure Studies by Means of Electron Spectroscopy*, volume 20 of IV. Nova Acta Regiae Soc. Sci. Upsaliensis (1967).
- [160] A. Lindblad. *A Treatise on the Geometric and Electronic Structure of Clusters: Investigated by Synchrotron Radiation Based Electron Spectroscopies*. PhD thesis, Uppsala University (2008).
- [161] D. A. Shirley. *Physical Review B*, **5**, 4709–4714 (1972).
- [162] S. Suga and A. Sekiyama. *Photoelectron Spectroscopy – Bulk and Surface Electronic Structures*, volume 176 of *Springer Series in Optical Sciences*. Springer, Berlin, 1st edition (2014).
- [163] S. Doniach and M. Sunjic. *Journal of Physical Chemistry C*, **3**, 285 (1970).
- [164] A. Lindblad, R. F. Fink, H. Bergersen, M. Lundwall, T. Rander, R. Feifel, G. Öhrwall, M. Tchapyguine, U. Hergenhahn, S. Svensson, and O. Björneholm. *The Journal of Chemical Physics*, **123**, 211101 (2005).
- [165] J.H. Scofield. *Journal of Electron Spectroscopy and Related Phenomena*, **8**, 129 – 137 (1976).
- [166] J. J. Yeh and I. Lindau. Atomic subshell photoionization cross sections and asymmetry parameters: $1 < Z < 103$. *Atomic data and Nuclear data tables*, **32**, 1–155 (1985).
- [167] M. P. Seah and W. A. Dench. *Surface and Interface Analysis*, **1**, 2 (1979).
- [168] S. Tanuma, C. J. Powell, and D. R. Penn. *Surface and Interface Analysis*, **17**, 911–926 (1991).
- [169] S. Tanuma, C. J. Powell, and D. R. Penn. *Surface and Interface Analysis*, **21**, 165–176 (1994).

- [170] Software for calculation the inelastic mean free path (2014). URL <http://www.quases.com/products/quases-imfp-tp2m/>.
- [171] F. R. Elder, A. M. Gurewitsch, R. V. Langmuir, and H. C. Pollock. *Physical Review*, **71**, 829–830 (1947).
- [172] A. Lindblad, S. Svensson, and K. Tiedtke. *A compendium on beam transport and beam diagnostic methods for Free Electron Lasers*. Deutsches Elektronen-Synchrotron DESY (2011).
- [173] J. D. Jackson. *Classical Electrodynamics*. Wiley, 3rd edition (1998).
- [174] H. Motz. *Journal of Applied Physics*, **22**, 527–535 (1951).
- [175] H. Winick, G. Brown, K. Halbach, and J. Harris. *Physics Today*, **34**, 50–63 (1981).
- [176] R. Lindblad. *Electronic Structures and Energy Level Alignment in Mesoscopic Solar Cells - A Hard and Soft X-ray Photoelectron Spectroscopy Study*. PhD thesis, Uppsala University (2014).
- [177] W. Drube. *Nuclear Instruments and Methods A*, **547**, 87–97 (2005).
- [178] M. Gorgoi, S. Svensson, F. Schäfers, G. Öhrwall, M. Mertin, P. Bressler, O. Karis, H. Siegbahn, A. Sandell, H. Rensmo, W. Doherty, C. Jung, W. Braun, and W. Eberhardt. *Nuclear Instruments and Methods A*, **601**, 48 (2009).
- [179] M. Gorgoi, S. Svensson, F. Schäfers, W. Braun, and W. Eberhardt. *The European Physical Journal Special Topics*, **169**, 221–225 (2009).
- [180] F. Schaefer, M. Mertin, and M. Gorgoi. *Review of Scientific Instruments*, **78**, 123102 (2007).
- [181] N. Mårtensson, P. Baltzer, P.A. Brühwiler, J.-O. Forsell, A. Nilsson, A. Stenborg, and B. Wannberg. *Journal of Electron Spectroscopy and Related Phenomena*, **70**, 117 – 128 (1994).
- [182] M. Gorgoi, S. Svensson, F. Schäfers, G. Öhrwall, M. Mertin, P. Bressler, O. Karis, H. Siegbahn, A. Sandell, H. Rensmo, W. Doherty, C. Jung, W. Braun, and W. Eberhardt. *Nuclear Instruments and Methods A*, **601**, 48–53 (2009).
- [183] F. Schaefer, M. Mertin, and M. Gorgoi. *Review of Scientific Instruments*, **78**, 123102 (2007).
- [184] S. Aksela, T. Kantia, M. Patanen, A. Mäkinen, S. Urpelainen, and H. Aksela. *Journal of Electron Spectroscopy and Related Phenomena*, **185**, 273 – 277 (2012).
- [185] Y. Takata, Y. Kayanuma, M. Yabashi, K. Tamasaku, Y. Nishino, D. Miwa, Y. Harada, K. Horiba, S. Shin, S. Tanaka, E. Ikenaga, K. Kobayashi, Y. Senba, H. Ohashi, and T. Ishikawa. Recoil effects of photoelectrons in a solid. *Physical Review B*, **75**, 233404 (2007).
- [186] S. M. Sze and K. K. Ng. *Physics of semiconductor devices*. John Wiley & Sons (2006).

- [187] R. J. Elliott. *Physical Review*, **108**, 1384 (1957).
- [188] J. Tauc, R. Grigorovici, and A. Vancu. *physica status solidi (b)*, **15**, 627–637 (1966).
- [189] J. Tauc, A. Menth, and D. L. Wood. *Physical Review Letters*, **25**, 749 (1970).
- [190] T. L. Barr. *J. Phys. Chem.*, **82**, 1801–1810 (1978).
- [191] B. I. Lundqvist. *Journal of Physics: Condensed Matter*, **9**, 236–248 (1969).
- [192] C. Kittel. *Introduction to Solid State Physics*. John Wiley & Sons, Inc., New York, 8th edition (1986).
- [193] G. B. Hoflund and G. R. Corallo. *Physical Review B*, **46**, 7110–7120 (1992).
- [194] J. Sundberg, R. Lindblad, M. Gorgoi, H. Rensmo, U. Jansson, and A. Lindblad. *Applied Surface Science*, **305**, 203 (2014).
- [195] M. Cruz, J. Morales, J. P. Espinos, and J. Sanz. *Journal of Solid State Chemistry*, **175**, 359–365 (2003).
- [196] A. R. H. F. Ettema, R. A. de Groot, C. Haas, and T. S. Turner. *Physical Review B*, **46**, 7363–7373 (1992).
- [197] C-C. Huang, Y-J. Lin, C-Y. Chuang, C-J. Liu, and Y-W. Yang. *Journal of Alloys and Compounds*, **553**, 208 – 211 (2013).
- [198] L. S. Price, I. P. Parkin, A. M. E. Hardy, R. J. H. Clark, T. G. Hibbert, and K. C. Molloy. *Chemistry of Materials*, **11**, 1792–1799 (1999).
- [199] P. A. Grutsch, M. V. Zeller, and T. P. Fehlner. *Inorganic Chemistry*, **12**, 1431–1433 (1973).
- [200] A. W. C. Lin, N. R. Armstrong, and T. Kuwana. *Analytical Chemistry*, **49**, 1228–1235 (1977).
- [201] R. Holm and S. Storp. *Journal of Applied Physics*, **9**, 217–222 (1976).
- [202] S. Tanuma, H. Yoshikawa, H. Shinotsuka, and R. Ueda. *Journal of Electron Spectroscopy and Related Phenomena*, **190**, 127–136 (2013).
- [203] L. Kövér, S. Kovács, R. Sanjinés, G. Moretti, I. Cserny, G. Margaritondo, J. Pálincás, and H. Adachi. *Surface and Interface Analysis*, **23**, 461–466 (1995).
- [204] A. Ettema and C. Haas. *Journal of Physics: Condensed Matter*, **5** (1993).
- [205] A. P. Grosvenor, B. A. Kobe, M. C. Biesinger, and N. S. McIntyre. *Surface and Interface Analysis*, **36**, 1564 (2004).
- [206] P. C. J. Graat and M. A. J. Somers. *Applied surface science*, **100**, 36–40 (1996).
- [207] T. Yamashita and P. Hayes. *Applied Surface Science*, **254**, 2441 (2008).
- [208] N. S. McIntyre and D. G. Zetaruk. *Analytical Chemistry*, **49**, 1521–1529 (1977).

- [209] J. Aarik, A. Aidla, T. Uustare, K. Kukli, V. Sammelselg, M. Ritala, and M. Leskelä. *Applied Surface Science*, **193**, 277 – 286 (2002).
- [210] M. Fondell, T. J. Jacobsson, M. Boman, and T. Edvinsson. *Journal of Materials Chemistry A*, **2**, 3352–3363 (2014).
- [211] I. Jogi, T. J. Jacobsson, M. Fondell, T. Väjten, J-O. Carlsson, M. Boman, and T. Edvinsson. In the Structural and Optical Properties of Ultrathin Iron Oxide Polymorphs Synthesized by ALD. Submitted to *Journal of Solid State Chemistry* (2014).
- [212] M. Schuisky, A. Hårsta, A. Aidla, K. Kukli, A. Kiisler, and J. Aarik. *Journal of The Electrochemical Society*, **147**, 3319–3325 (2000).
- [213] M. Volmer and A. Weber. *Zeitschrift für Physikalische Chemie*, **119**, 277–301 (1925).
- [214] I. N. Stranski and L. Krastanow. *Akademie der Wissenschaften Wien*, pages 797–810 (1938).
- [215] D. Neff, L. Bellot-Gurlet, P. Dillmann, S. Reguer, and L. Legrand. *Journal of Raman Spectroscopy*, **37**, 1228–1237 (2006).
- [216] H. Berger, H. Tang, and F. Lévy. *Journal of Crystal Growth*, **130**, 108 – 112 (1993).
- [217] J.A. Glasscock, P.R.F. Barnes, I.C. Plumb, A. Bendavid, and P.J. Martin. *Thin Solid Films*, **516**, 1716 (2008).
- [218] R. J. Thibau, C. W. Brown, and R. H. Heidersbach. *Applied Spectroscopy*, **32**, 532 (1978).
- [219] D. Bersani, P. P. Lottici, and A. Montenero. *Journal of Raman Spectroscopy*, **30**, 355–360 (1999).
- [220] N. Beermann, L. Vayssieres, S-E. Lindquist, and A. Hagfeldt. *Journal of The Electrochemical Society*, **147**, 2456 (2000). ISSN 00134651.
- [221] C. Pérez León, L. Kador, M. Zhang, and A. H. E. Müller. *Journal of Raman Spectroscopy*, **35**, 165–169 (2004).
- [222] T. Yamashita and P. Hayes. *Applied Surface Science*, **254**, 2441 (2008).
- [223] M. Muhler, R. Schlögl, and G. Ertl. *Journal of Catalysis*, **138**, 413 (1992).
- [224] E. Lewin, M. Gorgoi, F. Schäfers, S. Svensson, and U. Jansson. *Surface and Coatings Technology*, **204**, 455 – 462 (2009).
- [225] R. Kelly. *Materials Science and Engineering: A*, **115**, 11 – 24 (1989).
- [226] T.J. Chuang, C.R. Brundle, and K. Wandelt. *Thin Solid Films*, **53**, 19 – 27 (1978).
- [227] M. Fondell, M. Gorgoi, M. Boman, and A. Lindblad. *Journal of Electron Spectroscopy and Related Phenomena*, **195**, 195 – 199 (2014).

- [228] L. Wang, C-Y. Lee, and P. Schmuki. *Journal of Materials Chemistry A*, **1**, 212 (2013).
- [229] A. Müller. *Towards functional oxide heterostructures*. PhD thesis, Julius Maximilians Universität, Würzburg (2012).
- [230] R. Morrish, M. Rahman, J. M. D. MacElroy, and C. A. Wolden. *ChemSusChem*, **4**, 474 (2011).
- [231] Keisuke Kobayashi. *Nuclear Instruments and Methods*, **547**, 98 (2005).
- [232] Th. Eickhoff, V. Medicherla, and W. Drube. *Journal of Electron Spectroscopy and Related Phenomena*, **137-140**, 85 (2004).
- [233] T. J. Jacobsson and T. Edvinsson. *The Journal of Physical Chemistry C*, **118**, 12061–12072 (2014).
- [234] L. Vayssieres. *Optics and Photonics 2006 SPIE proceedings*, **6340** (2006).
- [235] B. M. Klahr, A. B. F. Martinson, and T. W. Hamann. *Langmuir*, **27**, 461–468 (2010).

Acta Universitatis Upsaliensis

*Digital Comprehensive Summaries of Uppsala Dissertations
from the Faculty of Science and Technology 1186*

Editor: The Dean of the Faculty of Science and Technology

A doctoral dissertation from the Faculty of Science and Technology, Uppsala University, is usually a summary of a number of papers. A few copies of the complete dissertation are kept at major Swedish research libraries, while the summary alone is distributed internationally through the series Digital Comprehensive Summaries of Uppsala Dissertations from the Faculty of Science and Technology. (Prior to January, 2005, the series was published under the title "Comprehensive Summaries of Uppsala Dissertations from the Faculty of Science and Technology".)

Distribution: publications.uu.se
urn:nbn:se:uu:diva-232948



ACTA
UNIVERSITATIS
UPSALIENSIS
UPPSALA
2014